DATA USE INVESTIGATIONS FOR APPLICATIONS EXPLORER MISSION A (HEAT CAPACITY MAPPING MISSION)

HCMM's Role in Studies of the Urban Heat Island, Great Lakes Thermal Phenomena and Radiometric Calibration of Satellite Data

John R. Schott*
and
Edward W. Schimminger

January 1981

Final Report

Calspan Report No. 6175-M-1

Prepared for:

NATIONAL AERONAUTICS AND SPACE ADMINISTRATION
GODDARD SPACE FLIGHT CENTER
GREENBELT, MARYLAND 20771

*Dr. Schott (currently with the Department of Photographic Science, Rochester Institute of Technology, One Lomb Memorial Drive, Rochester, N.Y. 14623) served as the Principal Investigator on this program.

CALSPAN ADVANCED TECHNOLOGY CENTER
A DIVISION OF CALSPAN CORPORATION
AN ARVIN COMPANY P.O. BOX 400 BUFFALO, NEW YORK 14225

TECHNICAL REPORT DATA
(Please read Instructions on the reverse before completing)

1. REPORT NO.	2.	3. RECIPIENT'S ACCESSION NO.

4. TITLE AND SUBTITLE DATA USE INVESTIGATIONS FOR APPLICATIONS EXPLORER MISSION A (HEAT CAPACITY MAPPING MISSION) HCMM's Role in Studies of the Urban Heat Island, Great Lakes Thermal Phenomena and Radiometric Calibration of Satellite Data

5. REPORT DATE January 1981

6. PERFORMING ORGANIZATION CODE

7. AUTHOR(S)
John R. Schott and Edward W. Schimminger

8. PERFORMING ORGANIZATION REPORT NO.
6175-M-1

9. PERFORMING ORGANIZATION NAME AND ADDRESS
Calspan Corporation

10. PROGRAM ELEMENT NO.

11. CONTRACT/GRANT NO.
NAS5-24263

12. SPONSORING AGENCY NAME AND ADDRESS
National Aeronautics and Space Administration
Goddard Space Flight Center
Greenbelt, Maryland 20771

13. TYPE OF REPORT AND PERIOD COVERED

14. SPONSORING AGENCY CODE

15. SUPPLEMENTARY NOTES

16. ABSTRACT

This report discusses the results of a study aimed at assessing the utility of data from NASA's Heat Capacity Mapping Mission satellite for studies of the Urban Heat Island, thermal phenomena in large lakes and radiometric calibration of satellite sensors. The data were found to be of significant value in all cases. Using HCMM data the existence and microstructure of the heat island can be observed and associated with land cover within the urban complex. The formation and development of the thermal bar in the Great Lakes can be observed and quantitatively mapped using HCMM data. In addition, the thermal patterns observed using the HCMM satellite data can be associated with water quality variations observed both from other remote sensing platforms and in situ. Finally, the Imaging Radiometer on-board the HCMM satellite is shown to be calibratible to within about 1.1°C of actual surface temperatures. These findings, as well as the analytical procedures used in studying the HCMM data, are included in the report.

17. KEY WORDS AND DOCUMENT ANALYSIS

a. DESCRIPTORS	b. IDENTIFIERS/OPEN ENDED TERMS	c. COSATI Field/Group
Key Words: Heat Capacity Mapping Mission, Atmospheric Effects, Infrared, Heat Island, Thermal Bar, Water Resources, Satellite, Remote Sensing, Lake Ontario, Thermal Infrared		

18. DISTRIBUTION STATEMENT	19. SECURITY CLASS *(This Report)* Unclassified	21. NO. OF PAGES
	20. SECURITY CLASS *(This page)* Unclassified	22. PRICE

EPA Form 2220-1 (9-73)

PREFACE

The objective of the research described in this report was to evaluate the utility of Heat Capacity Mapping Mission (HCMM) data for earth resources applications. The HCMM data were the output product of NASA's Applications Explorer Mission 1 program. This program had three specific objectives. The first objective was to determine if the data from the Heat Capacity Mapping Radiometer (HCMR) could be utilized to accurately measure surface temperatures (specifically water temperatures). The second objective was to determine if large scale diurnal and seasonal thermal phenomena in the Laurentian Great Lakes could be observed using HCMM data and, if observations were possible, could HCMM data provide significant input to water quality studies associated with thermal phenomena. The third major objective was to investigate the feasibility of using HCMM data to study macroscale/microscale thermal patterns associated with the well known urban heat island effect.

The program involved analyses of aerial underflight imagery, satellite image transparencies and computer compatible tapes as well as in situ and ancillary support data. The results of these analyses indicate that the thermal channel aboard HCMM can be radiometrically calibrated to provide surface temperatures within 1.1°C of actual surface values. The radiometric calibration of the HCMM thermal data enabled detailed mapping of the thermal bar phenomenon in Lake Ontario. The seasonal development of the thermal bar was observed using HCMM images and the day/night temperature difference data demonstrated that the diurnal development of the thermal bar could also be observed using HCMM data. HCMM data was also used to study the macro and micro structure of urban heating patterns. In particular, the role of vegetation in moderating the urban heat island was observed.

One primary recommendation for future thermal satellites would be more repetitive coverage to observe short term thermal phenomena and to improve the probability of cloud-free coverage. A second major recommendation would be development of an improved procedure for radiometric calibration of the sensor including correction for atmospheric effects. This study demonstrated that current radiometric correction procedures are inadequate if temperature measurements on the order of 1°C are required.

ACKNOWLEDGEMENTS

We would like to express our thanks to Harold Oseroff, our NASA technical monitor, for prodding us on throughout this program. We are also in great debt to John Price, Locke Stuart, and the entire HCMM experiment staff for making the experiment the success it has been. Closer to home, our gratitude goes to Mike Wilkinson and Martha Bronstein for input to the thermal bar experiment, Mike in particular for the thermal bar literature review. Tim Gallagher deserves special thanks for collecting the day/night HCMM underflight data. We would also like to acknowledge the support of Lee Herrington of S.U.N.Y., Syracuse, who provided Heat Island ground truth support and Thomas Lillesand and Doug Meisner of the University of Minnesota who provided the reprocessed digital images used in several places within this report.

TABLE OF CONTENTS

LIST OF ILLUSTRATIONS

LIST OF ILLUSTRATIONS (cont.)

LIST OF ILLUSTRATIONS (cont.)

LIST OF TABLES

Section 1

INTRODUCTION AND SUMMARY

The objective of the research described in this report was to evaluate the utility of Heat Capacity Mapping Mission (HCMM) data for earth resources applications. The HCMM data were the output product of NASA's Applications Explorer Mission 1 program. This program involved satellite collection of day/night thermal infrared data (10.5-12.5 μm) and registered day visible data (0.55-1.1 μm) in image and computer compatible tape (CCT) formats (HCMM Data Users Handbook 1980).

This program had three specific objectives. The first objective was to determine if the data from the Heat Capacity Mapping Radiometer (HCMR) could be utilized to accurately measure surface temperatures (specifically water temperatures). The second objective was to determine if large scale diurnal and seasonal thermal phenomena in the Laurentian Great Lakes could be observed using HCMM data and, if observations were possible, could HCMM data provide significant input to water quality studies associated with thermal phenomena. The third major objective was to investigate the feasibility of using HCMM data to study macroscale/microscale thermal patterns associated with the well known urban heat island effect.

This report discusses the background, approach, analytical methods and results of each aspect of the three-pronged experiment. The study area for the experiments centered on Lake Ontario and the nearby cities of Buffalo, Rochester and Syracuse in New York State. Satellite and underflight aircraft data were collected during 1978. The intent of the program was to apply the results of the HCMR calibration experiments to quantitative studies of the thermal bar in Lake Ontario (Rodgers 1965) and the urban heat island (Braham 1977).

It was demonstrated that by employing underflight calibration techniques the HCMR could be calibrated to within about 1.4°C of the actual water surface temperature. However standard atmospheric models (LOWTRAN and RADTRA)

were not capable of reproducing these results. Variation in path radiance appears to be one of the dominant factors affecting the variation in observed longwave radiance for spaceborne sensors.

Large scale thermal phenomena such as the spring thermal bars in the Great Lakes were readily observed by HCMM. The precise location of the thermal bar marks the boundary between the warm nutrient-rich water and the cold core of the lake. This location could be identified on maps drawn from CCT data which had been radiometrically corrected using the underflight procedures described above. It was also possible to observe turbidity gradients across the thermal bar using Landsat data.

The thermal anomaly caused by the extensive development in urban areas (known as the heat island) is readily evident on HCMM imagery. In addition, the thermal microstructure existent within the urban heat island associated with such features as large city parks can be observed.

In summary, this report describes some of the doorways opened to us by the high resolution large scale perspective offered by the HCMM experiment. It also discusses the techniques we have developed for extracting meaningful information from HCMM data and the potential roles thermal infrared satellites offer in monitoring and helping to solve some of the problems affecting our earth's resources.

Section 2

BACKGROUND

This section describes each of the phenomena investigated as part of the experiment and discusses previous work that was drawn on in our studies.

2.1 Remote Measurement of Temperature (background)

Remote measurement of surface temperatures employing longwave infrared line scanning systems has been practiced for many years (Scarpace et al 1974). Measurement of temperatures to accuracies better than a degree celcius using airborne infrared systems typically required use of ground truth. Collecting ground truth temperatures for a satellite with a 0.36 km^2 footprint posed a serious problem, so alternate approaches had to be considered.

One standard approach to calibrating satellite systems involves the use of atmospheric models of radiation transfer (Rangaswamy and Subbarayudu, 1978; Selby et al, 1978). These models are designed to account for the effect the atmosphere has on signal attenuation and also for the additive energy associated with emissions from the atmospheric constituents between the spacecraft and the ground. These effects are illustrated in Figure 2-1. A significant problem with these models is that they have never been extensively tested for use from earth observation platforms because of the difficulties involved in obtaining viable ground truth.

Schott (1979) described a procedure for a wholly airborne technique for radiometric measurement of water surface temperatures. This technique is described in detail in Appendix A. Essentially it involves flying an infrared line scanner at a series of altitudes over a target area and recording the radiant energy reaching the sensor. The radiant energy reaching the sensor at altitude is expressed as

$$W = \tau \varepsilon W_T + \tau W_S r + W_A \qquad (2\text{-}1)$$

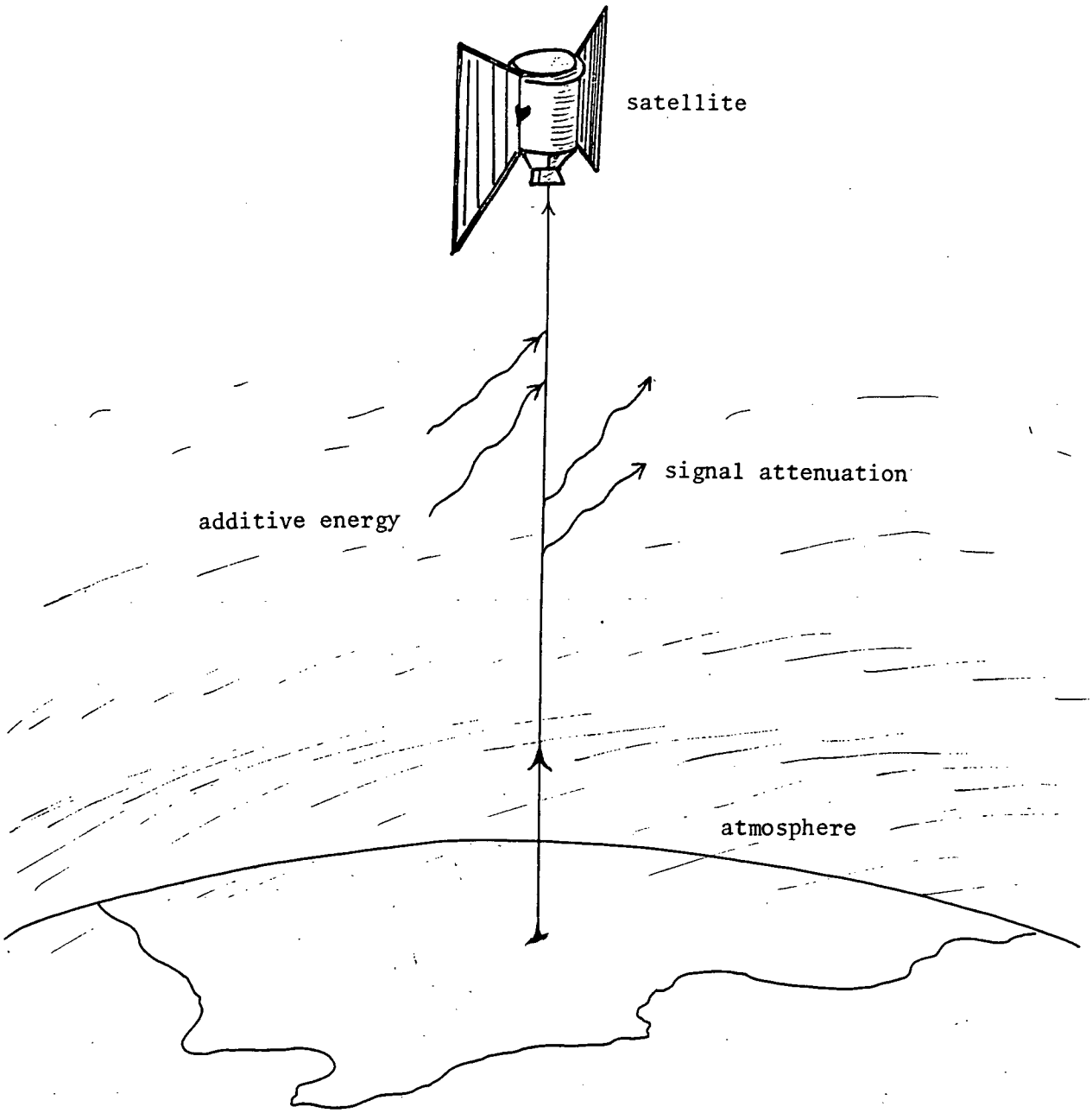

Figure 2-1. Atmospheric Effects on an Idealized Spaceborne Infrared Sensing System.

where:

- τ is the atmospheric transmission in the wavelength interval observed
- ε is the emissivity of the surface in this spectral region
- W_T is the energy that would be emitted (over the spectral region observed) by a blackbody at temperature T
- T is the surface temperature of the area observed
- W_S is the spectral radiant energy reaching the surface from the sky
- r is the reflectivity of the surface (ε+r = 1)
- W_A is the energy emitted by the atmosphere between the source and the sensor which reaches the sensor.

The energy paths described by equation 2-1 are illustrated in Figure 2-2. As detailed in Appendix A, Schott (1979) defined procedures for computation of the variables τ, W_A and W_S thus permitting direct aerial measurement of temperature for surfaces of known emissivity.

This technique, for calibration of aerial infrared scanning systems, was chosen as a tool in correcting the HCMR sensor data for atmospheric and background effects. By flying a fully calibrated airborne infrared system under HCMM we expected to be able to obtain ground truth. The temperatures measured using the aerial thermograms would be well within one degree celcius of the actual value and could cover areas much larger than the HCMM footprint.

The ground truth could then be used to calibrate the satellite so that actual surface emittance data (free of atmospheric effects) could be obtained. The data obtained in this manner could also be compared to the data obtained by using the LOWTRAN and RADTRA atmospheric models.

By evaluating the utility of the atmospheric models in this manner we can determine what accuracy can be obtained in satellite measurement of temperature.

The technical approach used in calibrating the satellite data is discussed in Section 3.1.

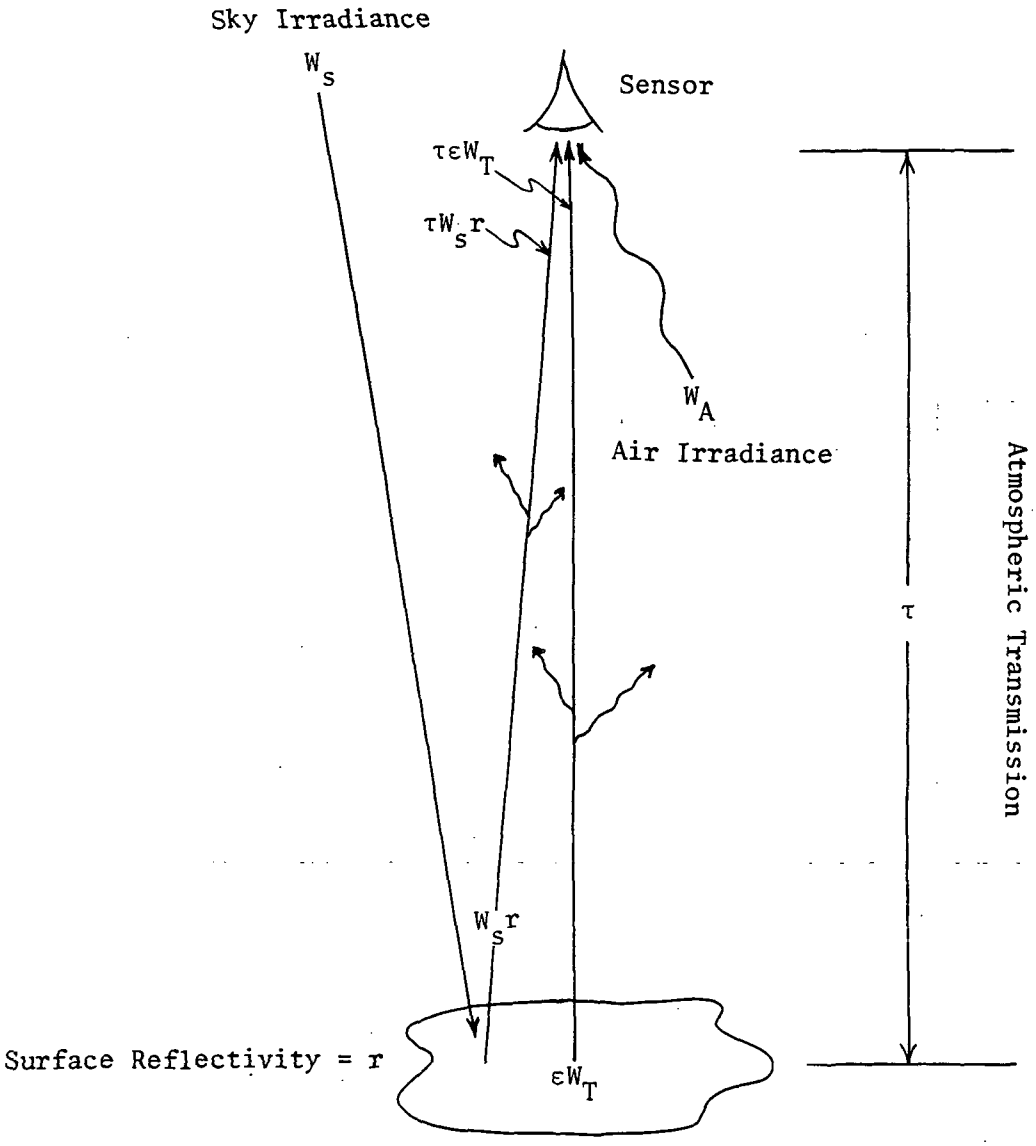

Figure 2-2. Energy Paths of Radiant Energy According to Equation 2-1.

$$W = \tau\varepsilon W_T + W_s r + W_A \qquad (2\text{-}1)$$

2.2 The Thermal Bar Phenomena (background)

In this section we briefly review the literature describing the thermal bar phenomena and proceed to discuss the potential for studying the phenomena using satellite sensing systems.

The thermal bar has been defined as the boundary layer between two oppositely stratified water regions, one with a surface temperature above 4°C in direct stratification, and the other with a surface temperature below 4°C in an inversely stratified configuration (Huang, 1972). The thermal bar has also been described for experimental purposes as a sinking zone consisting of water between 3.5 and 4.5°C travelling in front of a stable thermocline (Elliott and Elliott, 1970). Thermal bars occur during the spring and fall in dimictic, temperature zone lakes (Hubbard and Spain, 1973); however, the effect is much more pronounced and has been more extensively studied during the spring heating of large lakes fitting this description.

Development of the thermal bar occurs in two regimes (Rodgers and Sato, 1970). The first entails influx of natural or man-made sources of warm water to the shallow near-shore areas. Here, the first appearance and progression of a 4°C isotherm (representing the thermal bar) is dependent upon local conditions affecting the rate of heat input. The second mechanism involves both heating through the lake surface and lake heat content. Obviously, this regime occurs during early stages of the thermal bar period, but it does not exert dominance until the bar has travelled to a point past which significant influence by the first regime ends (Rodgers and Sato, 1970).

Figure 2-3, from Rodgers (1966), portrays the formation and progress of the thermal bar in Lake Ontario in 1965. The surface and mid-lake temperature profiles illustrate development of the thermal bar from winter to full summer lake stratification. The figure shows that as near-shore waters warm a 4°C isotherm forms around the lake. This creates a steadily constricting ring, which is driven by a density gradient penetrating the relatively cold and less dense waters of mid-lake. The progress of the spring thermal bar through the deeper parts of a lake is synonymous with the progress of stratification (Rodgers and Sato, 1970).

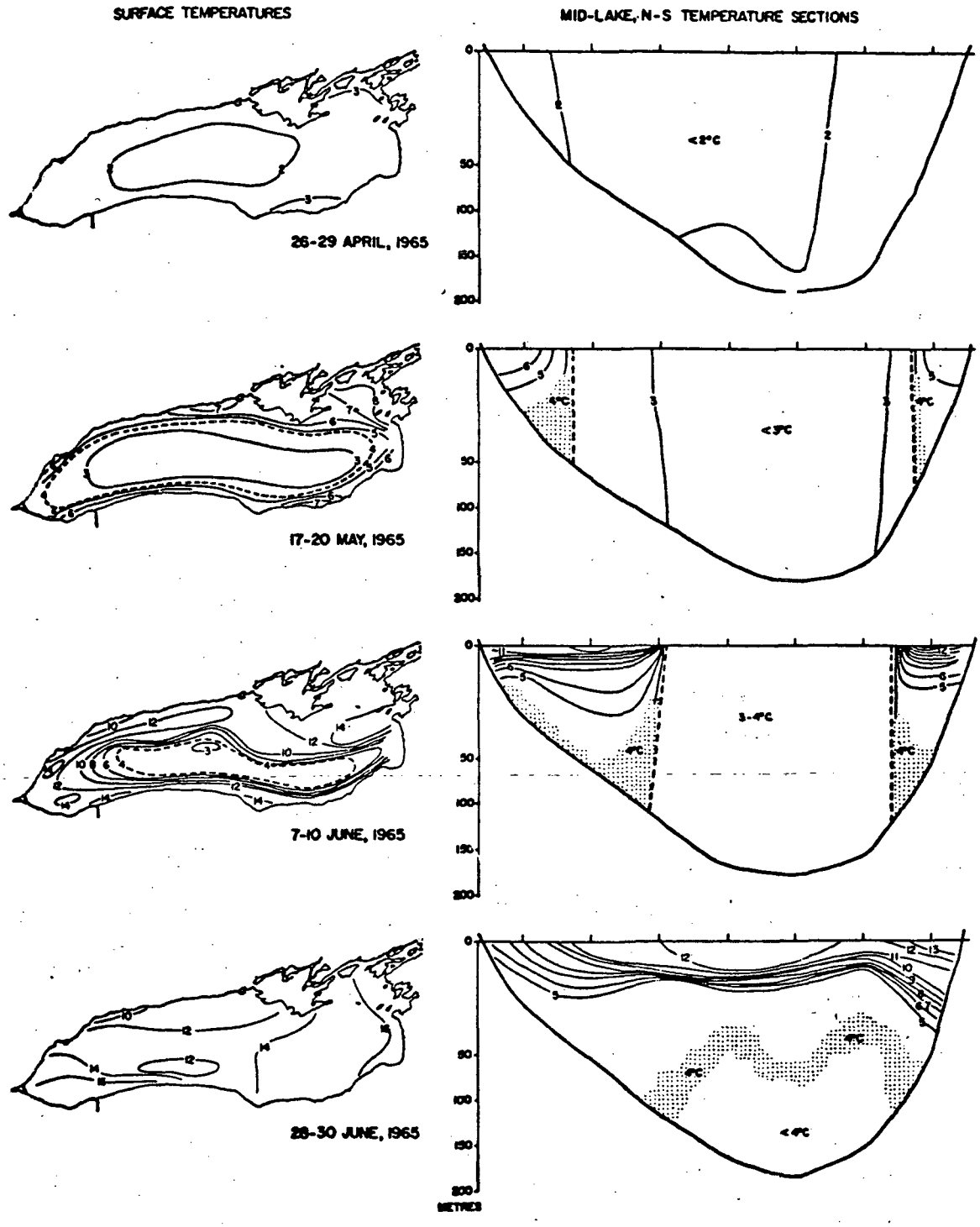

Figure 2-3. Formation and Progress of the Thermal Bar of Lake Ontario from Winter to Full Summer Stratification. (From Rodgers, G.K.: Publications Gt. Lakes Res. Div. Univ. Mich., 15: 372, 1966.) (From Wetzel, 1975)

Initial development of portions of the thermal bar is undoubtedly variable along the shoreline and precise dates for such formation are notably lacking in the literature. In Lake Michigan, the spring thermal bar period may start in late April or early May and may last from four to six weeks or more (Huang, 1972). Rodgers reported an instance of moderate thermal bar development in Lake Ontario by May 17-20 in 1965 (Wetzel, 1975).

Progression of the thermal bar continues until the last surface water trace of the 4°C isotherm has disappeared. At that point, according to one source, the lake has achieved full stratification (Rodgers and Sato, 1970), and the bar remnants sink and dissipate.

Thermal bar disappearance dates in Lake Ontario were estimated for the years 1965-1969, and the dates varied from June 8th to 22nd (Rodgers and Sato, 1970). The following year, in an extensive field investigation of the spring thermal bar in Lake Ontario, no disappearance date was mentioned (Rodgers, 1971). In 1970, Rodgers and Sato found a correlation between April 1st mid-lake heat content and date of disappearance. Their data suggested that the disappearance date might be predicted to within 4 days (Rodgers and Sato, 1970).

Thermal bars have been studied in at least two laboratory models (Elliott and Elliott, 1970) and several field investigations (Rodgers, 1971) (Hubbard and Spain, 1973), in addition to at least one set of mathematical models (Elliott and Elliott, 1971) and a physical model (Elliott and Elliott, 1970).

A quantitative laboratory model developed in 1970 suggests that a stable thermocline of water warmer than 4°C forms in the shallows. The advancing front end marks a boundary between the stable thermal structure in the shallows and the convecting deeper cold water across the bar. The model displayed a mean flow toward the deep end in the thermocline with a counter-flow underneath. Simultaneously, a flow near the surface travels toward the shallows. This current deflects downward and splits to form an upslope current in the shallows and a down slope current at depth. The thermal bar in this model was referred to as the sinking zone located in front

of the stable thermocline consisting of water between 3.5 and 4.5°C. This dense water was reported to be the result of heating cooler, lighter water from the deep end, and does not include water from the stable thermocline on the shallow side. This particular model assumed negligible horizontal advection and diffusion (Elliott and Elliott, 1970).

A major finding of extensive field investigations during the spring of 1970 in Lake Ontario was that no clear thermal evidence for bottom flows toward the deep portion of the lake ahead of the thermal bar was found. Small temperature increases observed at the bottom in this study were reported attributable to other factors including remnants of the winter hypolimnion and thermal fine structure (Rodgers, 1971).

Field studies showed an inverse correlation with thermal bar movement speed and lake bottom slope. During one set of surveys, the thermal bar moved with an average speed of 0.8 cm/sec. away from the north shoreline of Lake Ontario while travelling at 0.4 cm/sec. (average) away from the south shore (Rodgers, 1971). It is reasonable to assume that the velocity differential is responsible for the steep surface isothermal gradient shown along the southern shore of Lake Ontario (Wetzel, 1975). Although not addressed in the literature, some data suggest a narrowing of the bar as the phenomenon progresses.

Horizontal temperature gradients associated with the 4°C isotherm can vary from day to night and from one day to the next. Also, surface skim conditions can occur on the cold side of the thermal bar when strong heating is coupled with calm or very light winds. The skim can consist of water temperatures greater than 4°C (Rodgers and Sato, 1970), and this phenomenon could confound data interpretation.

Field studies of heat content change show no marked pattern when the thermal bar is close to shore. However, higher than average heat content changes take place between the positions of the thermal bar as it moves out into the lake on the north side of Lake Ontario. This trend was not noticed on the south side; however, very large positive heat changes occurred at mid-lake during the last one to two weeks of the presence of the thermal bar. Rodgers concluded that shore waters warm less than mid-lake waters, particularly during the last weeks of the thermal bar period (Rodgers, 1971).

The density related downward flowing currents along the vertical thermal bar result in a split flow penetrating the lower portions of the near-shore and off-shore water masses as mentioned previously. Earth's rotational forces combine with the density gradient to establish a counter clockwise coastal current (Wetzel, 1975).

The thermal bar phenomenon is associated with definite changes in water quality and biota. For example, visual field observations describing the high correlation of turbidity with temperature at the lake surface in the region of the 4°C isotherm had been common in the literature prior to 1967. Rodgers, in a 1967 study of Lake Ontario, confirmed the correlation quantitatively by using a towed transmissometer-thermometer and revealed increased detail as to the variety of horizontal temperature gradients. His data showed a marked inverse correlation between surface water temperature and surface water transparency as is evident in Figure 2-4 taken from his paper. The figure represents records of temperature and percent transmission on the crossings of the 4°C isotherm in Lake Ontario during the spring of 1967.

A major water quality consideration created by the thermal bar is the temporary isolation of inshore waters by the density barrier. Chemical and thermal enrichment via point and non-point discharges can occur in this region as a result of entrapment on the inshore side of the bar. As a result, increased productivity can occur earlier in the inshore areas than in the mid-lake region. Perhaps more importantly, the entire volume of lake water is unavailable for pollutant and nutrient reduction of dilution (Hubbard and Spain, 1973). The isolation of inshore waters suggests that seasonal limitations be established for pollutant loadings in effluent discharges to large lakes.

Preliminary bacteriological studies performed along the north shore of Lake Ontario during the spring of 1970, and designed to investigate the influence of the thermal bar on bacterial concentrations in the inshore area, indicated that a bacterial density gradient occurred with respect

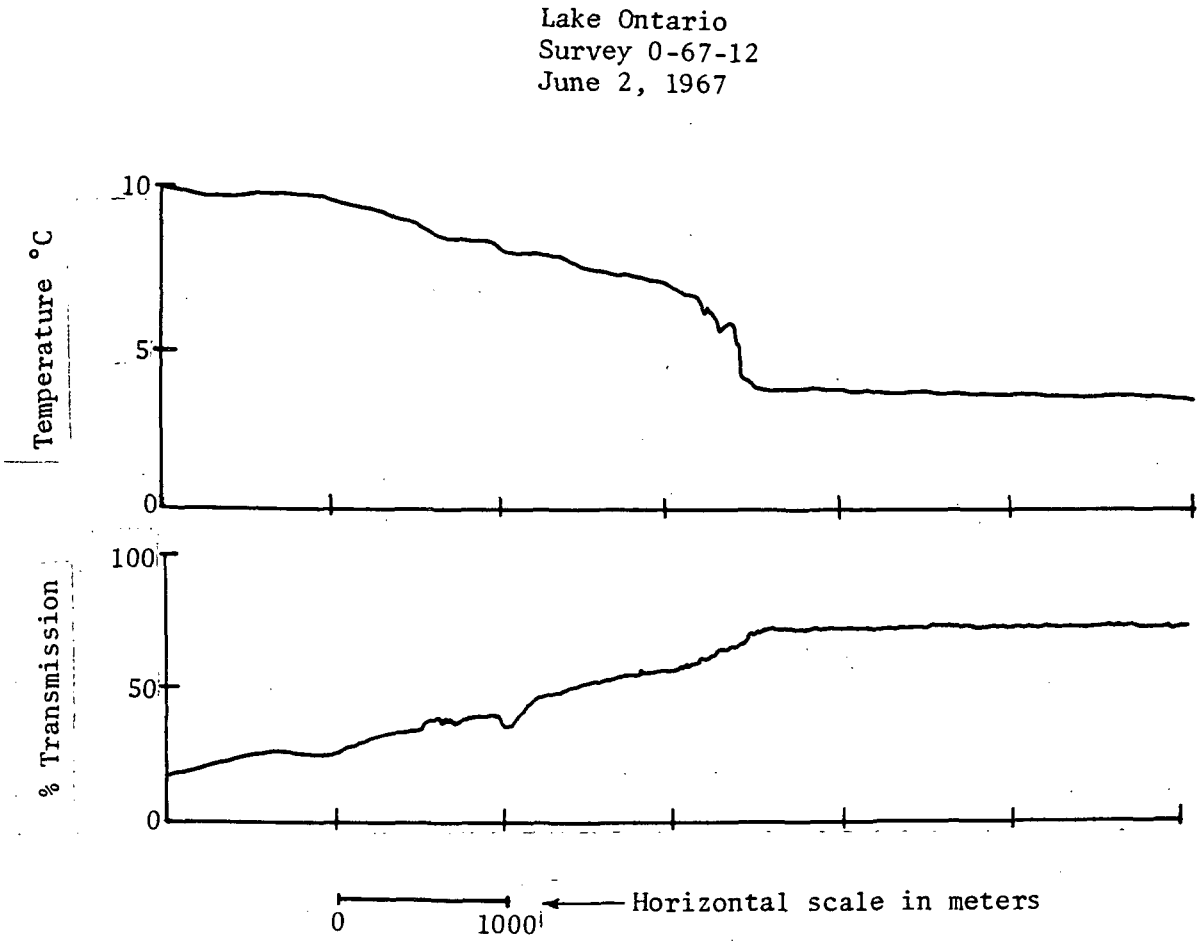

Figure 2-4. Characteristic Record of Temperature - Percent Transmission on Crossing the 4°C Surface Isotherm. (From Rodgers, 1968)

to the bar. Maximum bacterial densities were found to occur along the inshore boundary of the bar, suggesting that the thermal bar tends to concentrate bacteria within the inshore area (Menon et al, 1971).

Algal populations in Lake Michigan studied during the thermal bar period in 1967 were determined to be profoundly affected by the thermal bar. Both algal abundance and species composition were biological parameters heavily influenced. The highest algal populations observed during the study occurred at the interface between the waters inshore and offshore of the thermal bar, with algal populations considerably lower in local river water and waters offshore of the thermal bar (Stoermer, 1968). Figure 2-5.a portrays generalized isopleths of additive totals of algal cells for inshore waters during the Lake Michigan study. Sample station numbers are included for reference points. The total algal numbers shown in Figure 2-5.a appear to follow the same distribution as the physical parameters measured during the study. Figure 2-5.b shows surface temperature data as isotherms collected on the same date and at the same location as the algal data shown in Figure 2-5.a.

We expected HCMM to see the marked thermal gradients from mid-lake to near-shore associated with the spring thermal bar. We were particularly interested in determining the location of the thermal bar itself. We wanted to see if HCMM could be used to locate the 4°C isotherm that represents the zone of sinking water that physically separates the cold mid-lake water from the warmer inshore water. If this were possible studies of whole lake thermal phenomena would be possible using the nearly instantaneous data available from HCMM. It would also be possible to study short term (diurnal) development of the thermal bar by analysis of night/day temperature difference images available from HCMM. Our intent was to use the calibration methods discussed in the previous section to compute water surface temperatures for all of Lake Ontario. We could then use the data to isothermally map the lake.

In addition to the thermal properties of the lake we were acutely interested in water quality. The thermal bar prevents the heavily stratified inshore waters from mixing with the mid-lake water. The warm inshore water carrying nutrients, suspended solids and other potential pollutants

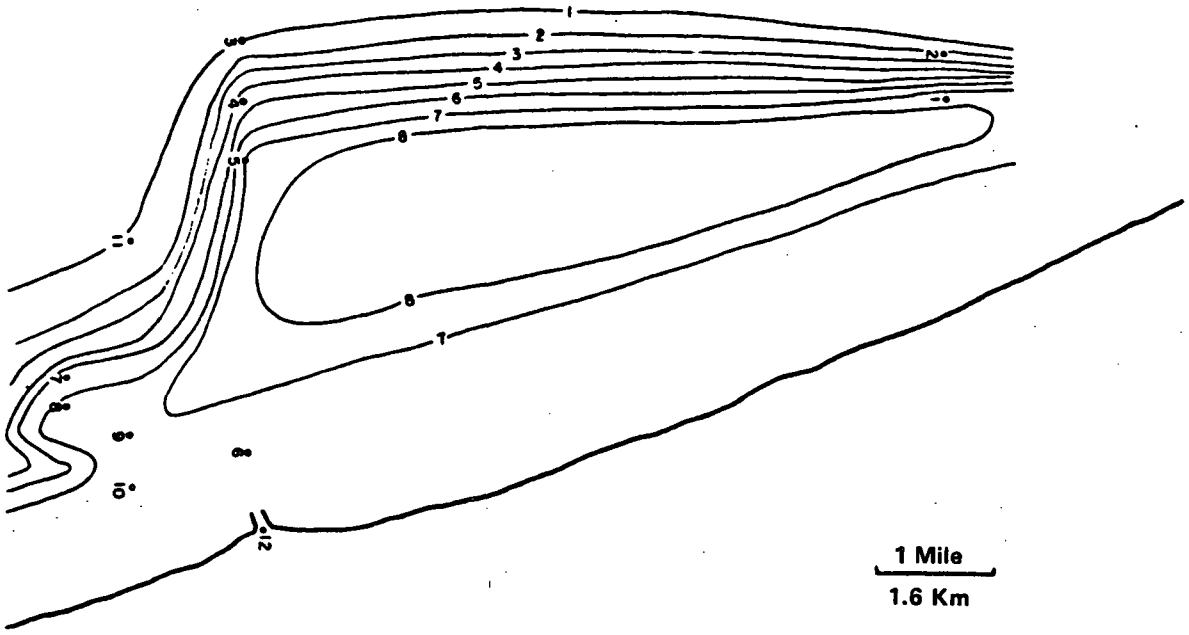

Figure 2-5a. Generalized Contours of Additive Totals of Algal Cells Per Four 1-ml Samples, Grand Haven, Michigan, Vicinity, 28 April 1967 (From Stoermer, 1968).

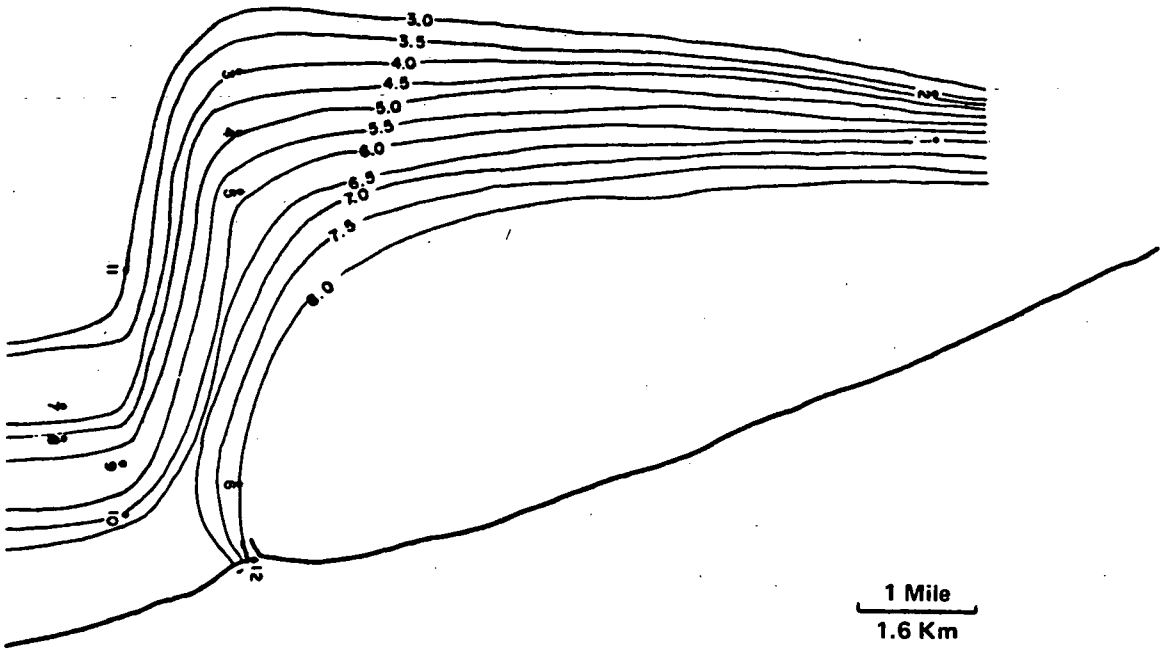

Figure 2-5b. Generalized 0.5°C Surface Temperature Contours, Grand Haven, Michigan, Vicinity, 28 April 1967 (From Stoermer, 1968).

from spring runoff is thus concentrated inshore of the thermal bar for the duration of the thermal bar. The warm nutrient-rich water provides an excellent environment for algal growth. The combination of a higher probability of suspended solids combined with increased algal standing crop should increase the turbidity of the inshore water.

Piech et al, 1978 and Schott 1980 have described a technique for remote assessment of water quality parameters using satellite or aerial photography. The technique involves a procedure for measurement of the spectral reflectance of the water by photometric analysis of color photographs. The reflectances measured from the images are processed through statistical models. These models were developed from laboratory measurement of the reflectance of water containing certain coloring agents (chlorophyll, suspended solids and yellowing organics) that modify the reflectance of water. Depending on the amount of ground truth available the output of these models can be expressed either, as the degree of change of the most significant water quality parameter varying between two points, or as actual concentration values of key water quality parameters. We felt that by applying this method of water quality analysis (described in greater detail in Appendix B), it would be possible to assess the feasibility of using HCMM data combined with other remotely sensed data to study the influence of the thermal bar on water quality. The technical approach used in evaluating this method is discussed in Section 3.2.

2.3 The Urban Heat Island (background)

The urban heat island is a phenomenon that occurs in developed urban centers. It is characterized primarily by elevated temperatures in an urban area as compared to surrounding rural areas. In addition to the discomfort brought on by excessive heat in urbanized areas, studies indicate that this excess heat, particularly at night in the summer, is actually related to an increase in human mortality (Clarke, 1972). If the influence of individual urban features (e.g., parks, open fields and industrial sites) on heat island development could be monitored, the knowledge gained could be beneficial to

future urban renewal and expansion in reducing the health hazards associated with the heat island. This project investigated the feasibility of studying the urban heat island problem using imagery provided by the HCMM satellite.

A large number of factors influence the development of an urban heat island. The physical properties of the materials found within an urban area are directly related to the absorption and reflection of incident energy (e.g., solar) and the emission of stored energy. Through industry and transportation, urban complexes generate additional heat independent of solar loading. Local meteorological conditions also affect the development of the heat island. Proper analysis of the heat island problem using satellite imagery requires appropriate consideration of each of these prime factors. A brief discussion of these parameters and the relationship of each to the development of the heat island follows.

The most outstanding factor influencing the development of an urban heat island is the high proportion of man-made materials used in an urban center. Unlike the abundant vegetation found outside the urban center, man-made materials do not exhibit the physiological process of evapo-transpiration. Thus, the radiant heat incident on an urban area cannot be removed through evaporative cooling, but rather is absorbed and used to raise the temperature of the material surfaces.

All the energy absorbed at the surface does not however go into raising the surface temperature. The energy is dissipated by convection, conduction and radiation. The extent of convection cooling is in part governed by air turbulence and is therefore related to the surface roughness of the material. Radiational cooling is governed by the temperature and emissivity of the surface. In addition to losing heat upward from the surface which we can think of as loss from the system; heat can also be conducted into the material. This heat will raise the temperature deeper in the material by removing heat from the surface. This term will also be a heat source when the surface begins to cool and heat is conducted back to the surface from within the material.

Lag times or phase shifts occur when a material stores heat below the surface. This heat tends to come up to the surface after the driving function begins to decline, maintaining high temperatures longer than if all the heat were at the surface. This is characteristic of most man-made materials used for pavements and building construction. In this way, after solar insolation begins to decline or is completed within the diurnal cycle, heat stored within pavements and building roofs and walls is slowly radiated from the material surfaces, maintaining warm temperatures within the urban area. A sample plot of some temperature variations in response to a sinusoidal driving function is shown in Figure 2-6. The effects of vegetative evapotranspiration processes are not included in this figure. The theoretical responses of the urban and rural areas are based solely on the densities of materials characteristically found within these areas, urban areas being composed generally of high density materials as mentioned above, and rural areas being composed of less dense vegetation and soils.

Atmospheric conditions also influence the ability of the urban area to cool after daytime insolation is completed. Cloud cover or haze will tend to reflect heat being emitted by the urban area back into the city (Mitchell, 1961). Smog, smoke, and particulates concentrated in the atmosphere over urban areas thus tend to enhance the contrast in temperature between the urban area where heat tends to be reflected back into the city and the surrounding rural areas which are more apt to "see" a clear sky which does not reflect the emitted heat. In this way, overcast sky conditions, either natural or man-induced, tend to increase the severity of the heat island formation by locking excess heat within the urban area.

The air movement across an area also affects its tendency to lose excess heat. Under stable, low-wind conditions, the heat stored by day in an urban region is not removed by convective cooling and remains to heat the city air. Strong heat islands are thus inclined to develop on still nights.

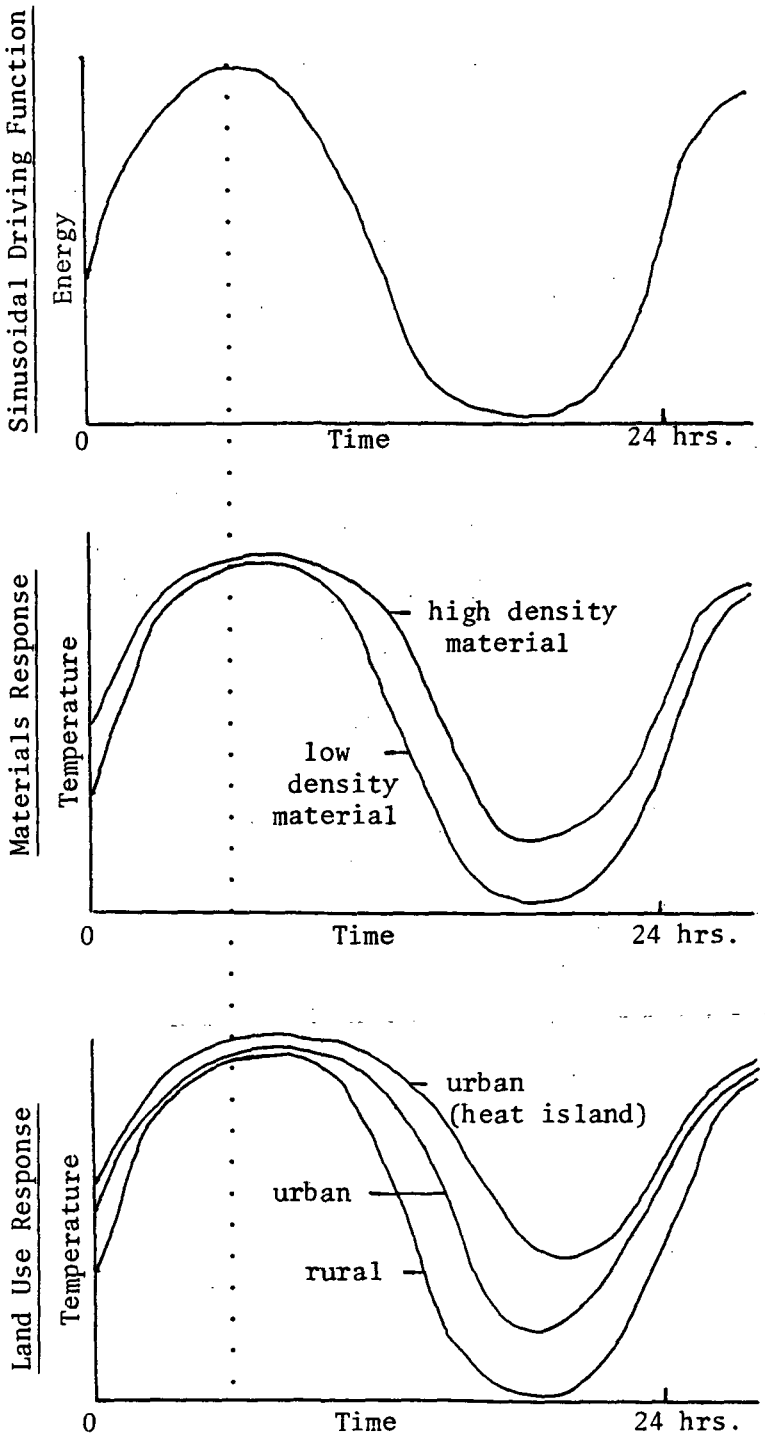

Figure 2-6. Theoretical Temperature Response to a Sinusoidal Driving Function. Higher Density Materials Tend to Absorb and Store More Heat Than Less Dense Materials, Releasing the Stored Energy During Periods of Low Loading. In Terms of Cities This Means That Urban Areas, Consisting Basically of Higher Density, Man-Made Materials, Tend to Absorb Solar Radiation During the Day and Re-emit it During the Night, Maintaining Higher Temperatures in the City Than in Surrounding Rural Areas Composed of Less Dense Materials.

As described in the above discussion, the urban heat islands develop as a result of numerous factors. The individual effects resulting from increased particulate matter in the atmosphere, higher density materials used for urban construction, and the lower vegetation levels often associated with large urban areas combine to create the phenomenon known as the urban heat island. The non-homogeniety of these factors across an urban complex must give rise to variations in the heat island within the limits of one urban complex. Increases in the percentage of tree cover in certain urban areas, for example, would be expected to increase the cooling capabilities of those immediate areas and possibly of proximate areas also. Analysis of temperature variations within an urban area may lead to the identification of those certain factors which have the greatest positive and negative effects on the heat island development. Identification of these factors could aid in future urban planning and renewal to benefit the health of people who work and live in urban areas.

HCMM satellite imagery provides an available and relatively inexpensive tool for analysis of these factors. Image scale and resolution permit observation of the major configuration of imaged heat island formation as well as some detail of the variability of temperature within the urban area. The technical approach used to investigate the potential of HCMM data for study of the urban heat island phenomenon is discussed in Section 3.3.

Section 3

TECHNICAL APPROACH

This section discusses separately the definition of each of the three experimental questions addressed by the program as well as data collection and analysis techniques.

The three aspects of the experiment: atmospheric effects, the thermal bar and the heat island, were integrated geographically into the central and western New York areas bordering Lake Ontario and the lake itself. The HCMM spacecraft was underflown 7 times as detailed in Table 3-1. Thermal infrared (8-14 μm) and color photography (day only) were collected for selected ground tracks. Figure 3-1 is a HCMM thermal image of Lake Ontario showing the typical coverage pattern for an underflight mission.

3.1 Atmospheric Effects Experiment

Calibration of the HCMR for atmospheric and background effects required collection of "underflight" truth data. These data were obtained by flying an infrared scanner through the profile calibration approach described in Appendix A. The aircraft data were typically obtained at altitudes ranging from 1 to 2 thousand meters. The atmospheric profiles to calibrate the system would be flown from flying height down to near ground level. Profiles were normally flown at Buffalo (Huntley Power Station), Rochester (Ginna Power Station), Nine Mile Point Power Station and Syracuse (Onondaga Lake). An example of the type of data obtained during a profile is shown in Figure 3-2. This figure shows apparent temperature plotted against altitude for several surfaces with different temperatures observed during a profile. Figure 3-3 shows the extrapolated (zero altitude) surface radiances plotted against the observed radiances at altitude. As discussed in detail in Appendix A the slope of the line plotted in Figure 3-3 is a measure of atmospheric transmission and the intercept is a function of the path radiance illustrated in Figure 2-2.

Table 3-1

HCMM Underflight Schedule Indicating the Major Sites Covered on Each of the Seven Missions.

Underflight Mission	Buffalo	Rochester	Syracuse	Lake Ontario Thermal Bar
22 May 1978 - Day	x	x	x	x
6 June 1978 - Day	x	x	x	x
6 June 1978 - Night	x	x	x	x
14 August 1978 - Day	x	x	x	
14 August 1978 - Night	x	x	x	
1 November 1978 - Night	x	x	x	
2 November 1978 - Day	x	x	x	

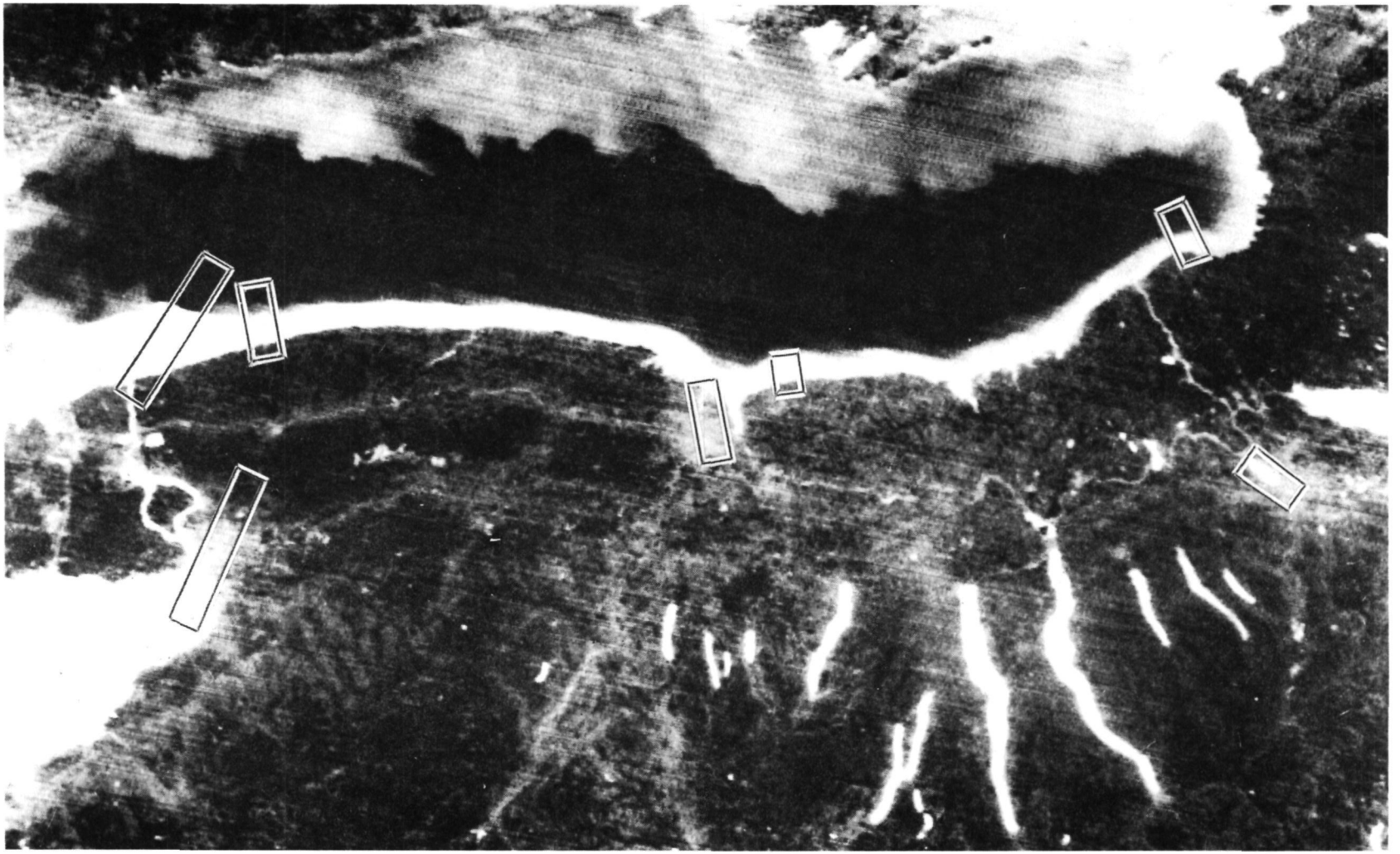

Figure 3-1. HCMM Thermal Image of Lake Ontario. Boxed in Areas Indicate Ground Tracks Typically Covered By an Underflight Mission. Surface Temperatures Obtained for These Areas Using Calibrated Underflight Data Are Used to Calibrate the HCMR and Thus Obtain Surface Temperatures for the Entire Lake.

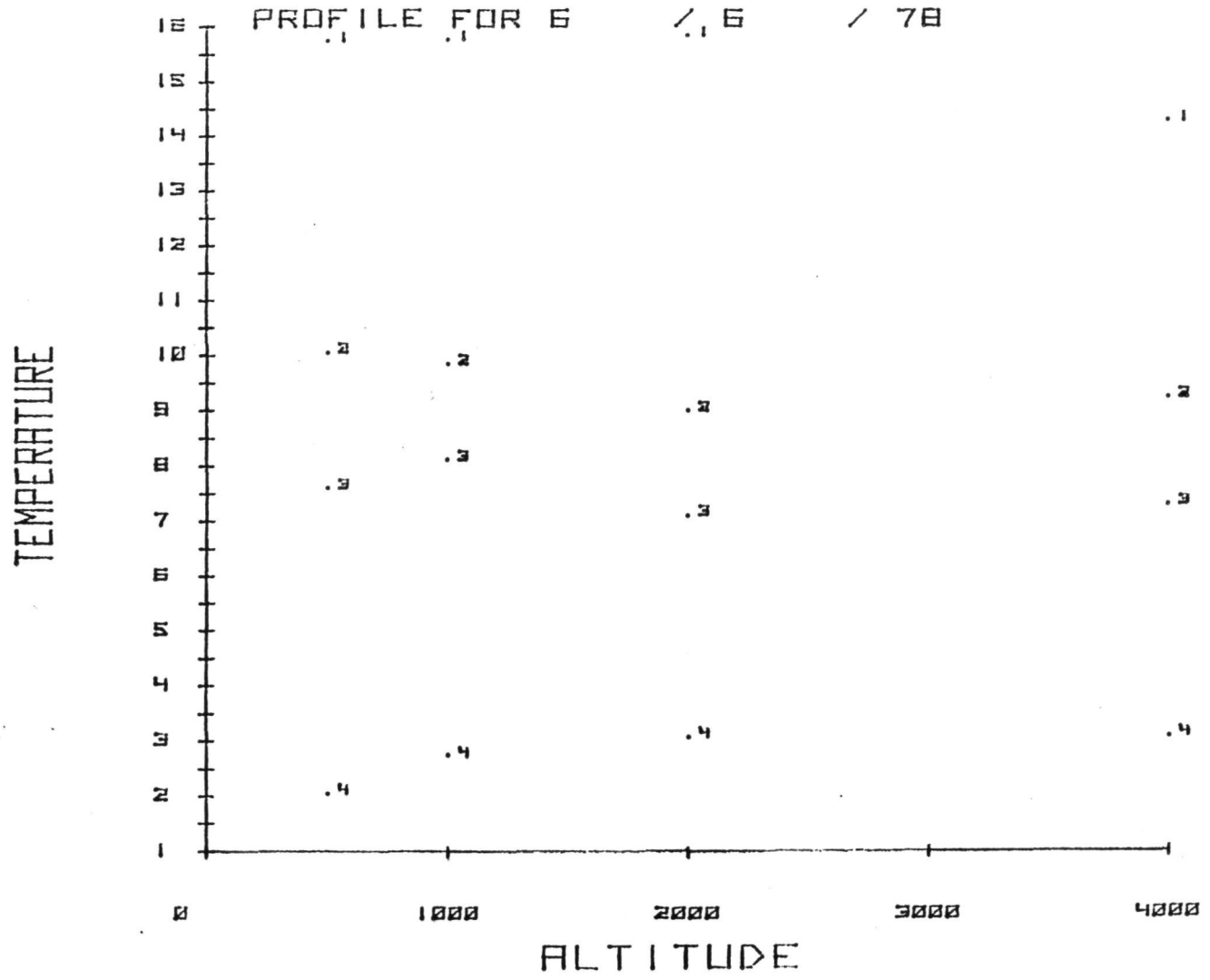

Figure 3-2. Example of Data Obtained During a Profile. Apparent Temperature (°C) is Plotted Against Altitude (Ft.) for Several Surfaces with Different Temperatures.

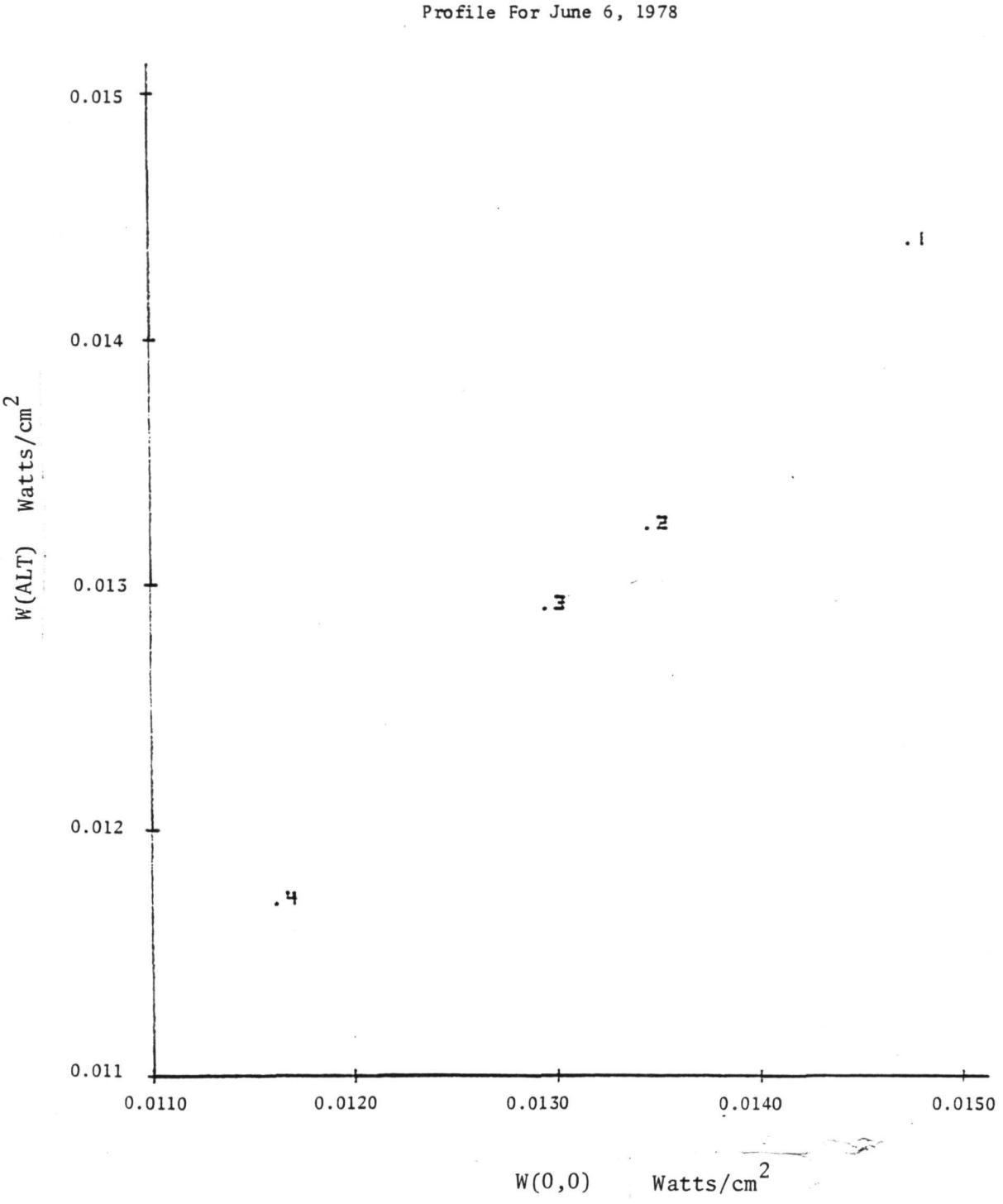

Figure 3-3. Surface Radiances Plotted Against Observed Radiances at Altitude.

By employing these calibration parameters it is possible to compute the radiant energy or equivalent blackbody temperature originating from any object observed by the infrared scanning system at flight altitude. Employing this approach "ground truth" was obtained by underflying the HCMM space craft. A fully calibrated line scanner was flown over a known ground track (usually over water because of its slowly varying thermal structure). Density readings were made of the aerial infrared imagery representing surface areas equivalent to the HCMM IFOV. These densities were converted to integrated surface temperature values using the procedures described above. Apparent satellite temperatures of these same areas were computed by analysis of digital HCMM data. Figure 3-4 shows a plot of actual surface temperature of Lake Ontario as measured by the aircraft along a flight line out from shore. Figure 3-5 is a plot of the apparent temperatures as viewed by the HCMR corresponding to this same flight line. By regressing the satellite observed apparent temperatures against the actual surface temperatures we can establish a linear relationship for correcting satellite temperatures to surface temperatures, where the slope of the relationship

$$T_{satellite} = m\, T_{surface} + b \qquad (3\text{-}1)$$

is a function of atmospheric transmission (over the 10.5-12.5 μm bandpass) and the intercept is a function of path radiance. Figure 3-6 is a plot showing how this type of analysis was applied to HCMM imagery.

The satellite was calibrated in this manner at several locations on each underflight. By comparing the correction equations the physical extent over which a correction was applicable could be estimated. The variation in atmospheric effects from day to day was also evaluated. Finally, by studying meteorological conditions and location of the calibration site relative to the sensor, the effects of factors such as visibility, air temperature and slant path length could be studied.

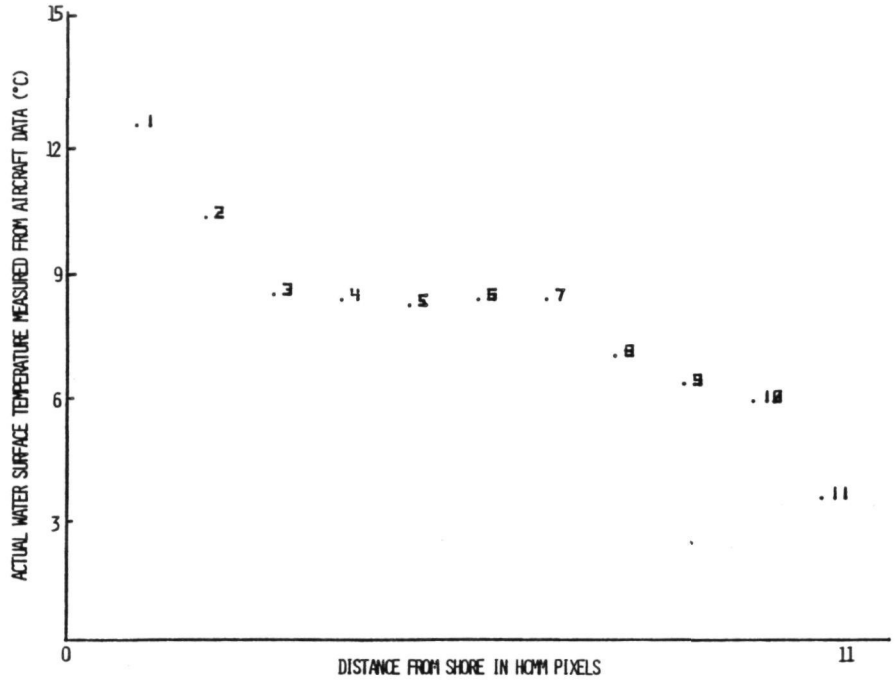

Figure 3-4. Corrected Aircraft Data for 9 Mile Point - June 6, 1978

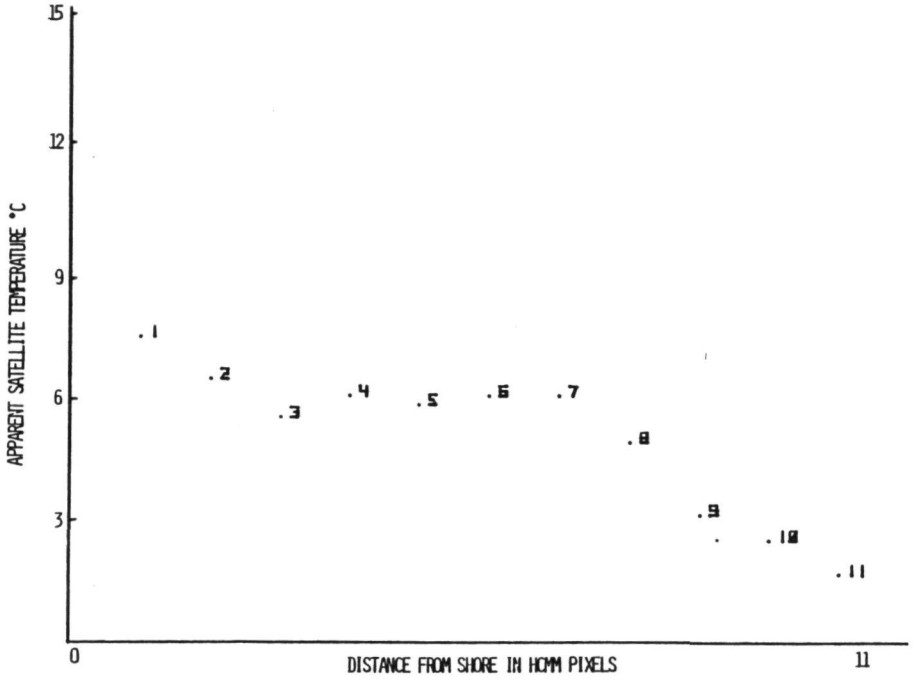

Figure 3-5. Uncorrected Satellite Data for 9 Mile Point - June 6, 1978

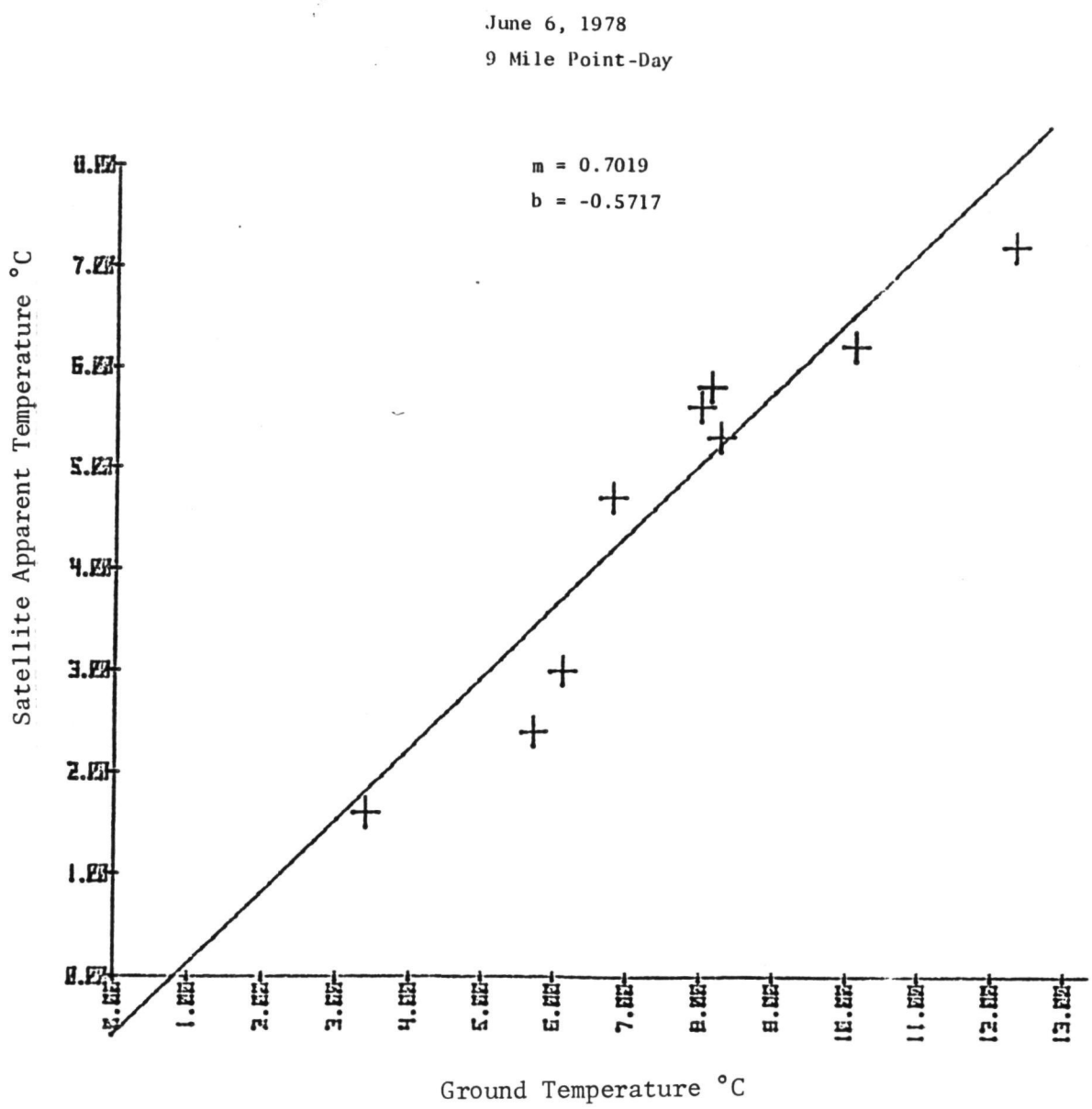

Figure 3-6. Regression of Satellite Observed Apparent Temperatures Against Measured Surface Temperatures.

The experiment was also designed so that radiosonde data collected by the National Weather Service at the Buffalo airport could be incorporated into atmospheric propagation models. These models provided corrections to the HCMR data for atmospheric effects. The predicted temperatures obtained by the models were then compared to the empirical values obtained via the underflight method.

The results of these absolute temperature atmospheric calibration analyses are presented in Section 4.1.

3.2 Thermal Bar Experiment

Data collection on the thermal bar experiment concentrated on underflights out from the southern shore of Lake Ontario across the bar. Three flight lines were flown on May 22, 1978 and again on June 6, 1978. The aerial infrared data was calibrated using the empirical method (Schott 1979) described in the previous section. This densitometric analysis of the thermal data permitted precise location of the 4°C zone characterizing the thermal bar. Color photographs were also collected along these flight lines using Hasselblad 500 EL (70 mm format) cameras. Figure 3-7 shows two examples of the water quality changes visible along the flight line. Figure 3-8 shows simultaneous color and thermal infrared images of the thermal bar illustrating how marked the change in temperature and water clarity can be.

The HCMM thermal infrared images clearly depict the effectiveness of the thermal bar in trapping warmer water on the inshore side. Figures 3-9 through 3-14 are HCMM infrared images illustrating the progression of the Lake Ontario thermal bar in 1978. In the early spring the lake surface is at nearly a constant temperature with only an isolated trace of warming near shore (Figure 3-9). By May 26 of 1978 the bar has clearly formed and the cold core of the lake is encircled by a narrow ring of warm water (Figure 3-10). In the following weeks the warm water forces its way out from shore exhibiting more rapid movement from the shallow northern shore and sharper thermal gradients on the southern shore (Figures 3-11 to 3-13).

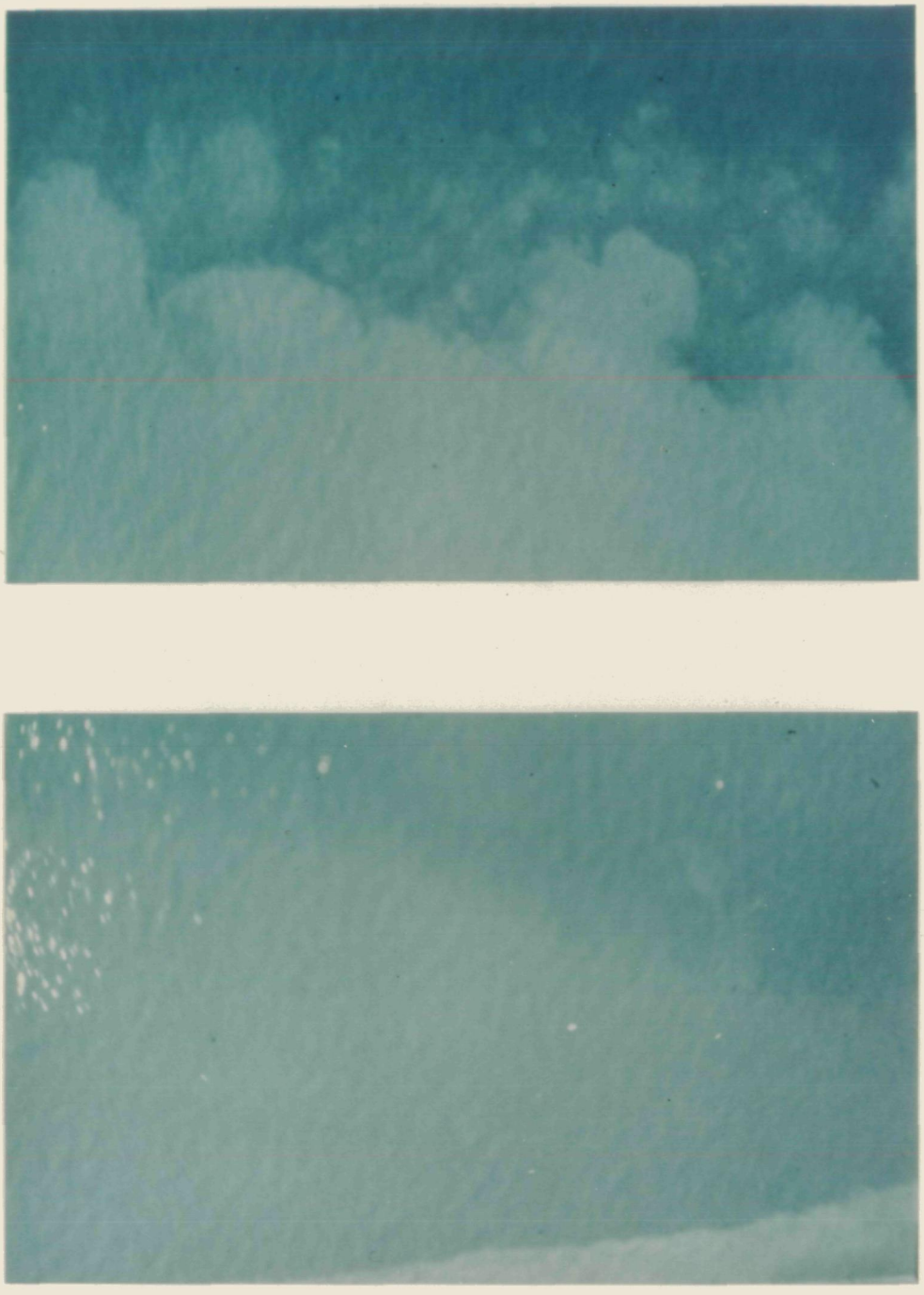

Figure 3-7. Two Examples of Water Quality Changes in Lake Ontario Visible on Standard Color Photography Taken 22 May 1978 (North is up). The Brightness of the Water is Related to the Turbidity of The Lake. The Lower Photograph, Taken 2 Miles From Shore, Shows Changes in Water Quality Resulting From the Cooling Water Discharge of a Power Plant on the South Shore of Lake Ontario. The Top Photograph, Taken 3 Miles From the Shore, Shows the Marked Change in Water Quality at the Thermal Bar.

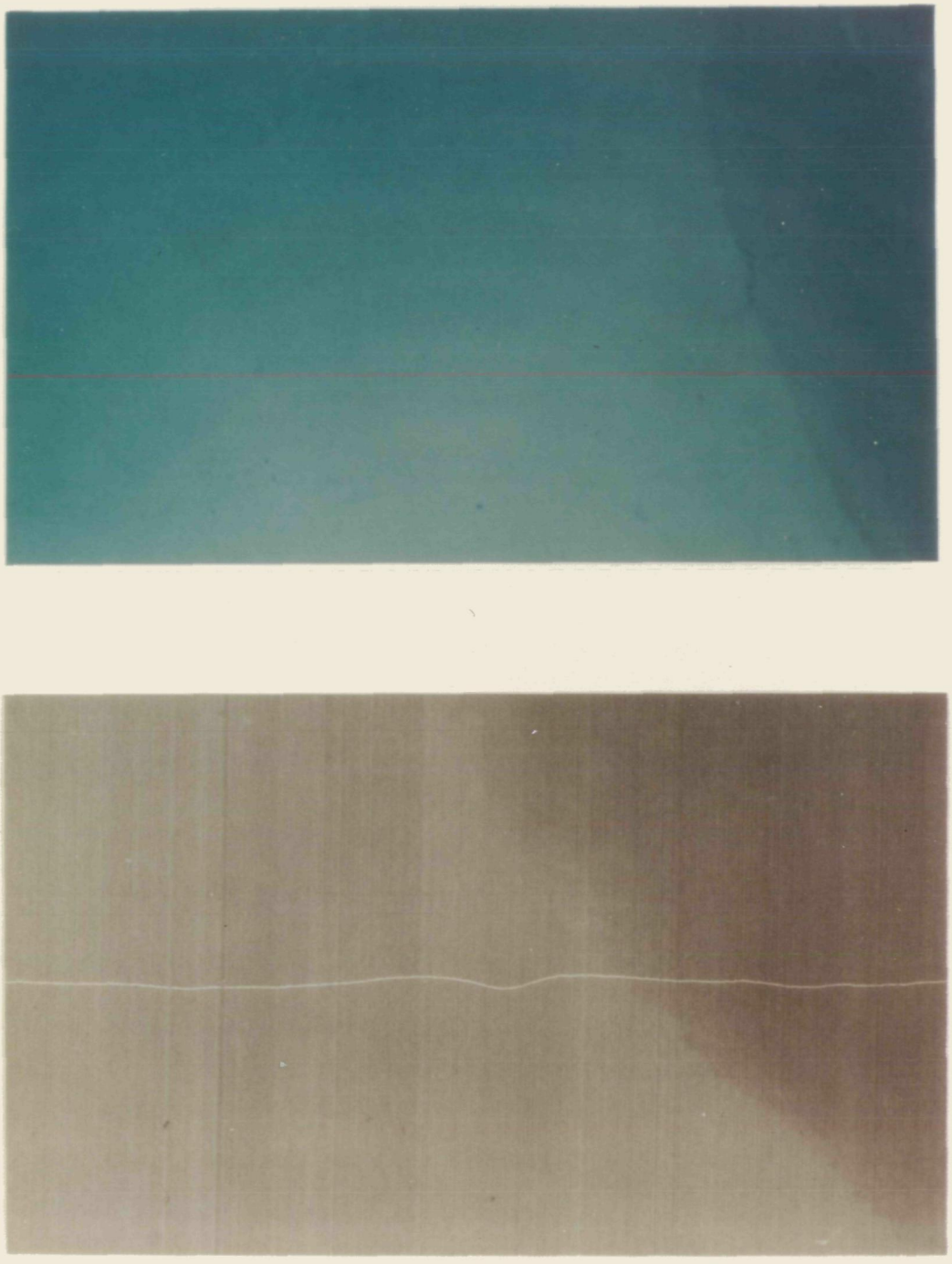

Figure 3-8. Simultaneous Color and Thermal Infrared Images of the Thermal Bar in Lake Ontario - 22 May 1978. The Marked Change in Temperature Across the Thermal Bar is Clearly Shown in the Lower Illustration; Light is Warm, Dark is Cold. The Corresponding Change in Water Quality Can be Seen in the Top Photograph Where the Dark, Clear Water Corresponding to the Colder Temperatures Beyond the Thermal Bar Can be Seen in the Upper Right Corner.

Figure 3-9. Lake Ontario Thermal Bar Development - 11 May 1978. The Lake Surface is at Nearly a Constant Temperature With Only a Small Trace of Warming Near Shore.

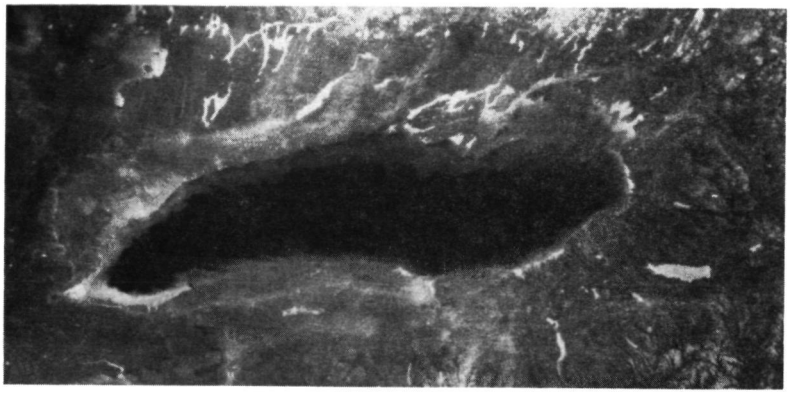

Figure 3-10. Lake Ontario Thermal Bar Development - 26 May 1978. A Narrow Ring of Warmer Water Encircles the Entire Lake.

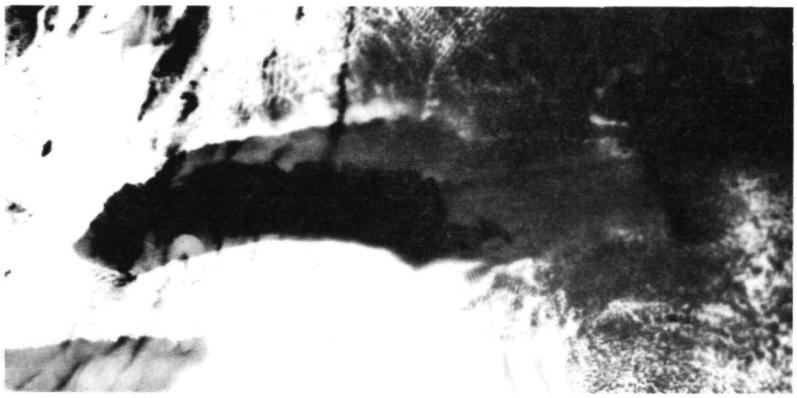

Figure 3-11. Lake Ontario Thermal Bar Development - 1 June 1978. The Thermal Bar Advances More Rapidly From the Shallow, Northern Shore of the Lake.

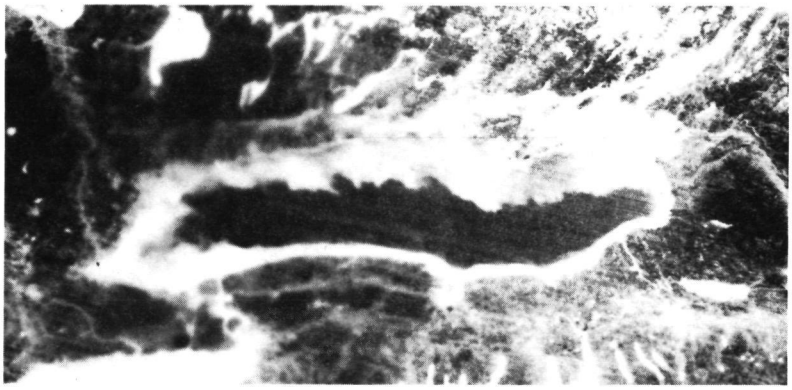

Figure 3-12. Lake Ontario Thermal Bar Development - 6 June 1978. The Thermal Bar is Well Developed With the Sharp Change in Temperature Between the Warm Inshore Waters and the Cold Core of the Lake Being Clearly Visible.

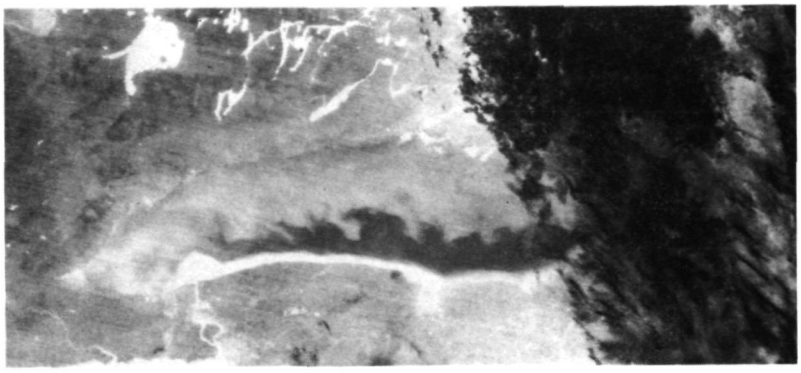

Figure 3-13. Lake Ontario Thermal Bar Development - 22 June 1978. The Thermal Bar Has Advanced Very Little From the Deep, Southern Shore; Only a Small Portion of the Cold Core of the Lake Remains.

Figure 3-14. Lake Ontario Thermal Bar Development - 4 July 1978. The Cold Core of the Lake Has Sunk to the Bottom and the Lake has Fully Stratified.

Finally, by July 4, 1978, the lake has fully stratified (Figure 3-14). The images shown in Figures 3-9 to 3-14 clearly illustrate that HCMM data can be used to subjectively observe the thermal development of the bar. Indeed Figure 3-15 shows that the thermal bar is a large lake phenomenon readily observed in all the Great Lakes.

Quantitatively mapping the thermal bar is a more difficult task. The location of the 4°C isotherm, which is the temperature at which water is most dense and therefore sinks, is important because this represents the physical limit of dilution of inshore water. Quantitative mapping of the thermal patterns in the lakes was accomplished by sorting the HCMR CCT data and printing isothermal displays. Figure 3-16 is an example of an isothermal display of the raw CCT data. The limitation of this approach is obvious when one recognizes that the negative mid-lake temperatures are impossible. It was necessary, therefore, to utilize the empirical calibration techniques described in Section 3.1. By applying the corrections generated using the underflight method, isothermal maps such as those shown in Figures 3-17 and 3-18 were generated. The accuracy of these maps will be discussed in Section 4.1.

The color photography was calibrated at the shoreline ends of the flight lines using the method of Piech and Schott (1978), (Appendix B). This approach permits conversion of density measurements on the photographic records to the volume spectral reflectance of the water. The spectral reflectance values of the water are then input to a model whose output indicates what the dominant water quality change (chlorophyll change, lignin change or yellowing organic change) is between a reference point and the point in question. This method was applied by collecting density values from the cold core of the lake and then along the ground track toward shore. The water farthest from shore (in the stable core of the lake) was used as the reference point and changes from that point were computed by processing the data as described above and detailed in Appendix B. In Figure 3-19 the changes indicated by the densitometric analysis of the color imagery as well as the magnitude

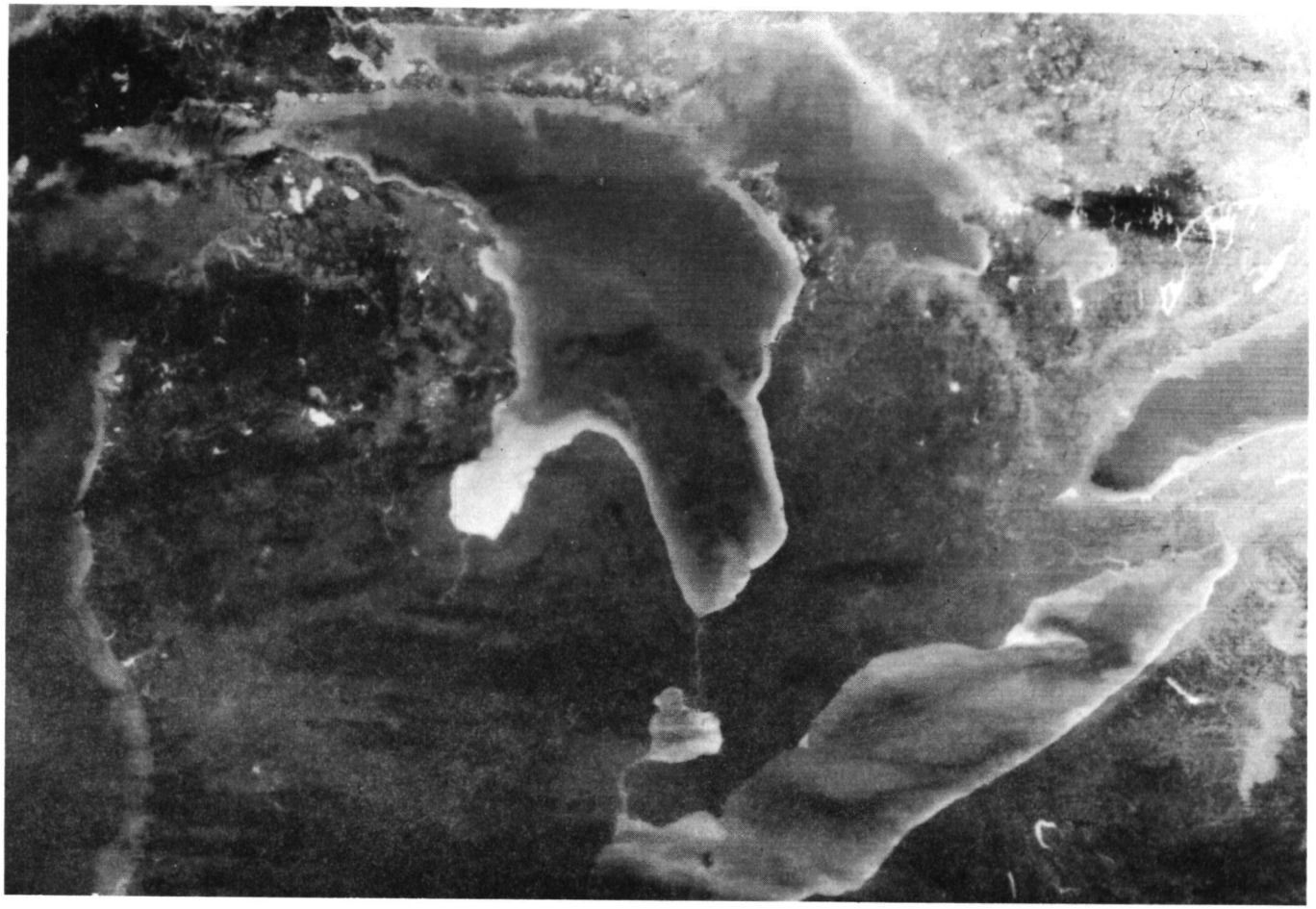

Figure 3-15. Thermal Image of the Great Lakes - 22 May 1978. The Thermal Bar is a Large Lake Phenomenon Observable in all the Great Lakes. The East Shore of Lake Michigan, Lake Huron and Lake Ontario Show Clear Indications of Spring Thermal Bar Development in the Above Illustration. Lake Erie, Located at the Lower Right, Exhibits a Less Marked Thermal Bar Because it is Much Shallower than the Other Great Lakes and Warms Much Faster.

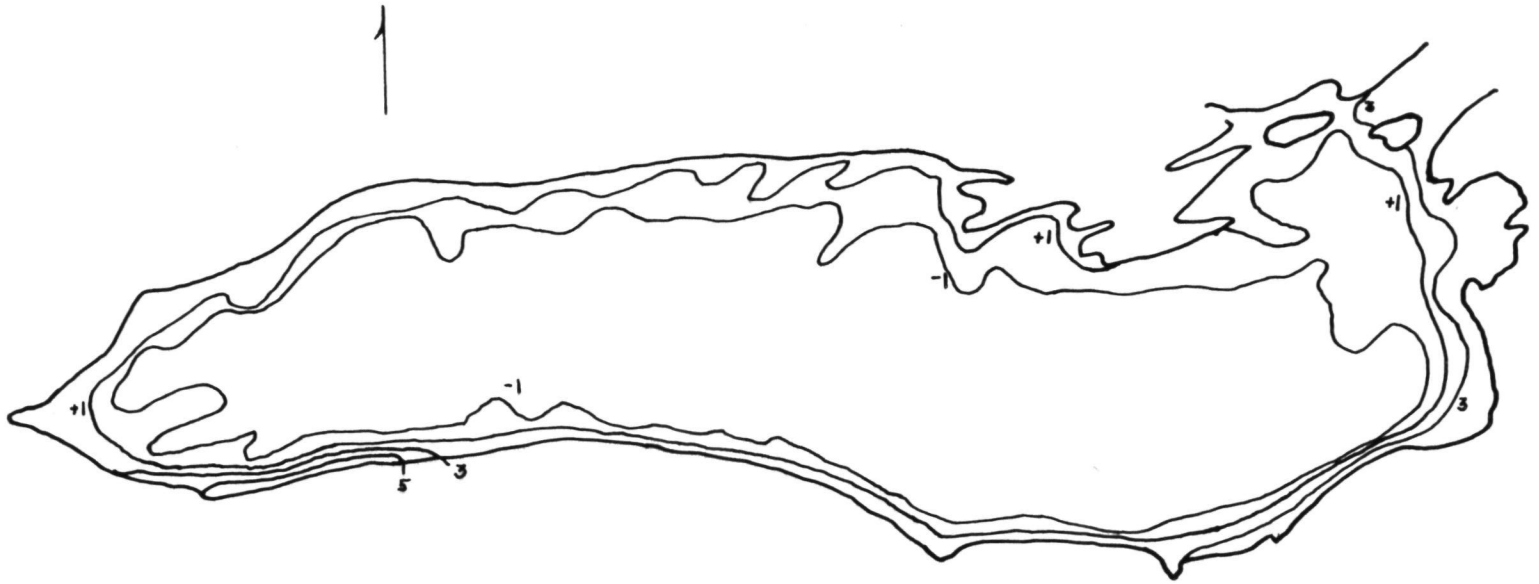

APPARENT SURFACE RADIOMETRIC TEMPERATURE (°C)
LAKE ONTARIO
22 MAY 1978 - 1400 EDT

Figure 3-16. Thermal Map of Lake Ontario from HCMR Data - 22 May 1978 - 2 p.m. EDT. No Atmospheric Calibration Was Applied to the HCMR Data; the Unrealistic, Below Freezing Temperatures in the Center of the Lake Indicate That Uncalibrated HCMR Data is Not Adequate For Accurate Mapping of the Lake Temperatures.

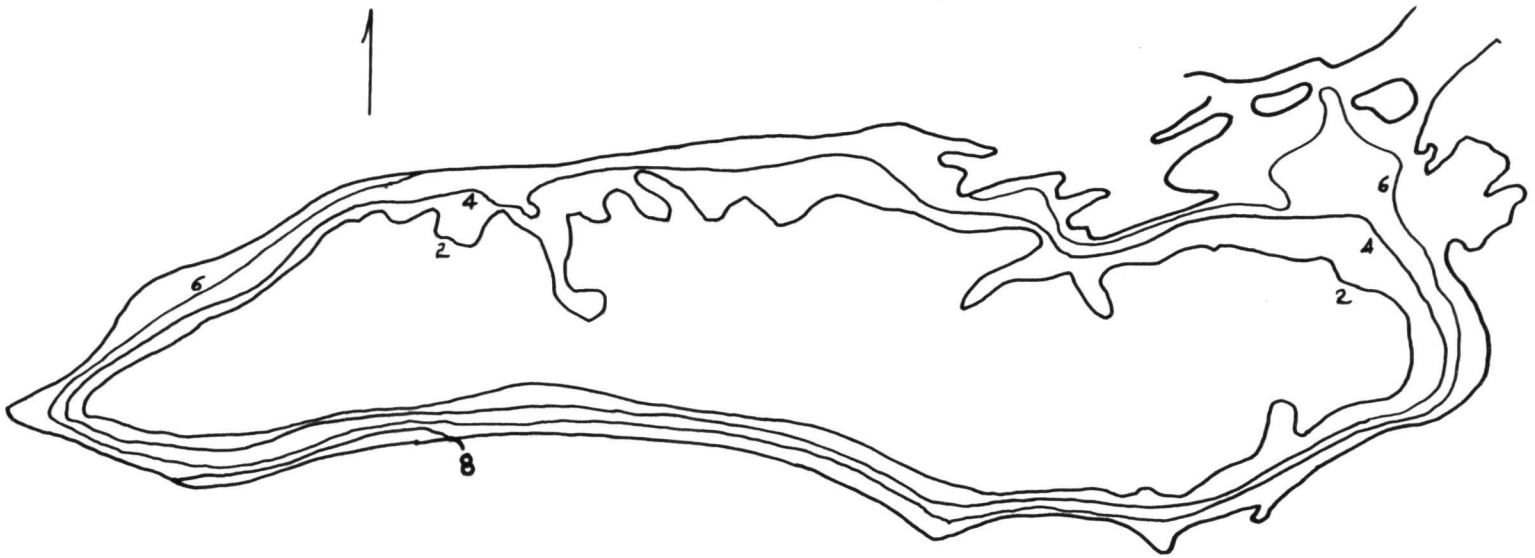

SURFACE RADIOMETRIC TEMPERATURE (°C)
LAKE ONTARIO
22 MAY 1978 - 1400 EDT

Figure 3-17. Thermal Map of Lake Ontario from Calibrated HCMR Data - 22 May 1978 - 2.p.m. EDT.

Figure 3-18. Thermal Map of Lake Ontario from Calibrated HCMR Data - 6 June 1978 - 2 a.m. EDT.

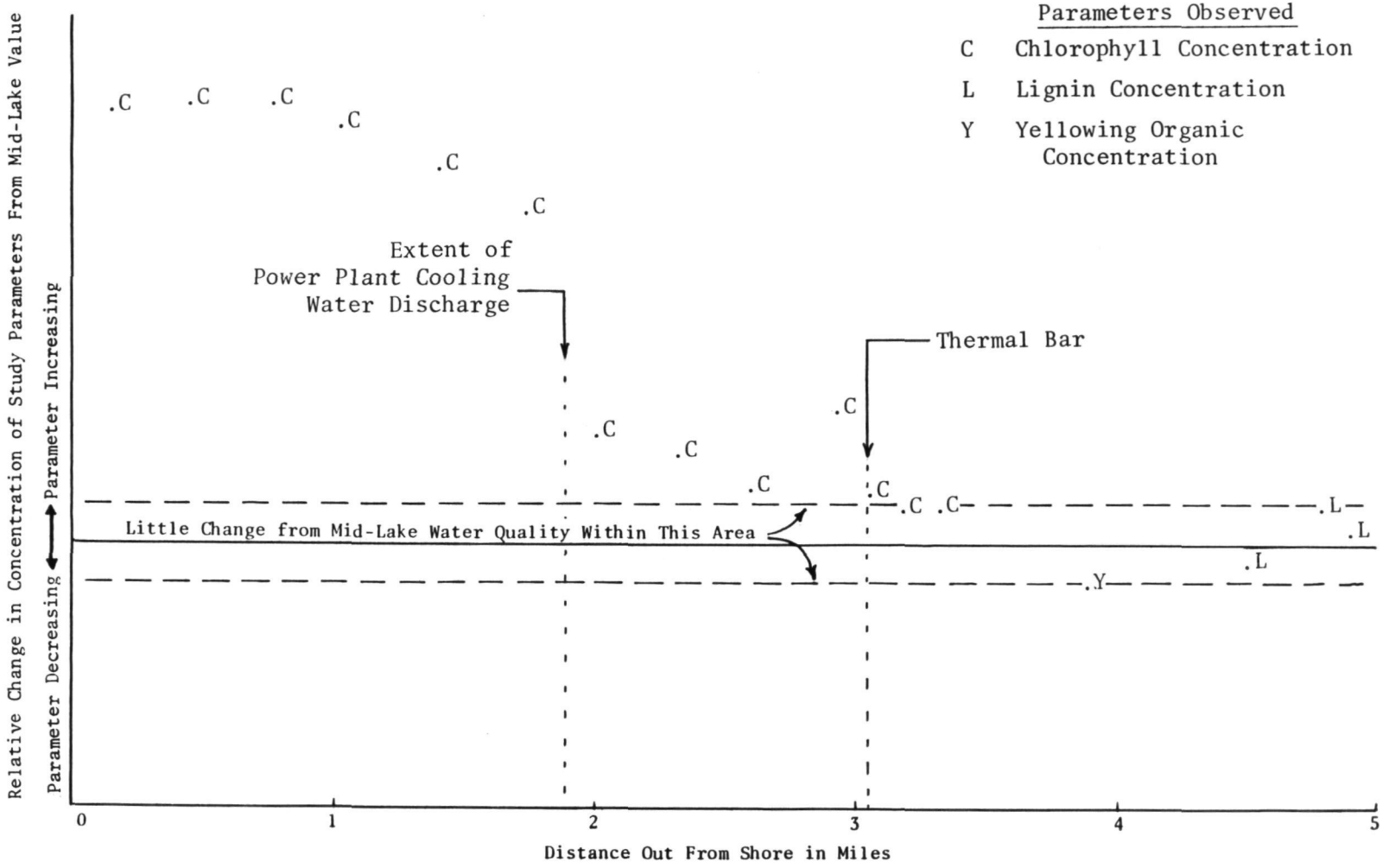

Figure 3-19. Dominant Water Quality Changes From the South Shore of Lake Ontario to Mid-Lake Across the Thermal Bar - May 22, 1978. Concentrations are Presented Relative to the Water in the Stable Core of the Lake.

of the changes are plotted against distance from shore. In this case, as in all those studied, the dominant change in moving across the thermal bar was an increase in algal populations as indicated by increased chlorophyll concentrations. A more detailed interpretation of these results is presented in Section 4.2.

3.3 Heat Island Analysis

An initial investigation of the potential of HCMM data for analysis of certain thermodynamic properties of urban centers was also performed. Of particular interest under this experiment was an examination of surface temperature patterns within an urban area as related to land use, land cover, and meteorological conditions. This examination of data gave rise to several interesting observations; a presentation and discussion of these observations is given later in this section.

Study of the urban heat island problem was concentrated over two cities - Buffalo, New York and Syracuse, New York. As presented earlier in Table 3-1, underflight thermal scanner data were obtained for several dates. In addition to the underflight data, ground data were collected on 2 November 1978. These data were collected at eight locations in and about Syracuse at the same time as the satellite overflights - approximately 2 a.m. and 2 p.m. local time. Ground data consisted of the apparent radiometric temperatures of large, uniform surfaces such as parking lots. These were obtained using a Barnes PRT-5 radiometer with a 2° field of view. The instrument was aimed vertically at the ground element from an elevation of five feet. Air temperature and relative humidity data were also obtained at each location.

Figure 3-20 illustrates the numerous radiometric readings taken at one of the ground sites. This process was typical of the eight stations for which ground data were collected. Figure 3-21 shows the location of each ground station in Syracuse along with a tabulation of the corresponding ground data.

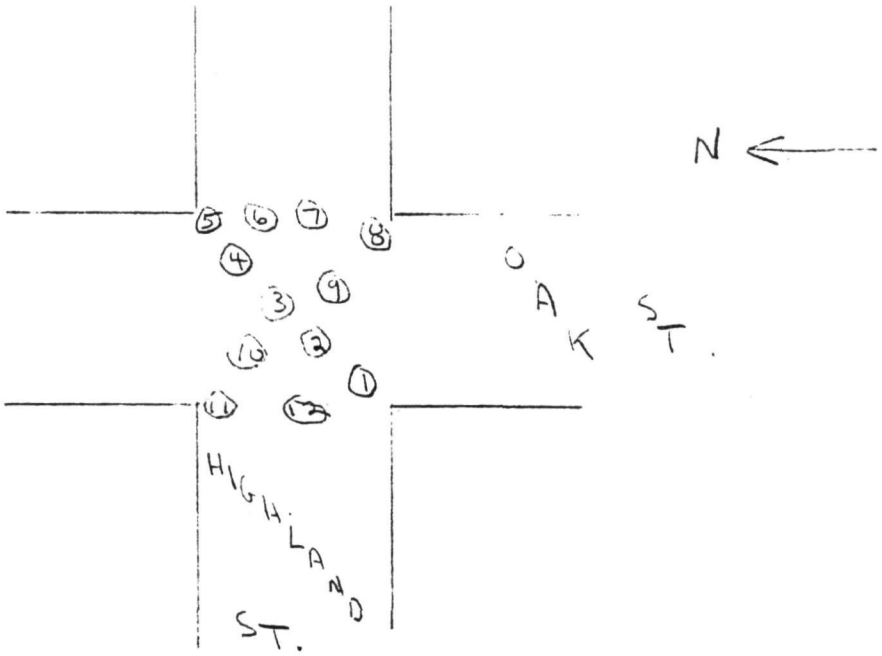

#	am	pm
1	3.0	14.0
2	4.5	18.0
3	5.0	21.6
4	5.0	17.5
5	4.5	20.5
6	4.5	18.0
7	4.5	22.0
8	5.0	22.0
9	5.0	21.5
10	5.5	17.5
11	5.0	22.0
12	5.0	21.0

Station 5
02:20,'14:30
Highland St./Oak St.

am/pm
relative humidity:70%/55%
wind speed: 0.5mph/ 5.0mph
wind direction:
air temperature:38.0/64.4 F

Figure 3-20. Ground Data Collected at Syracuse Station #5

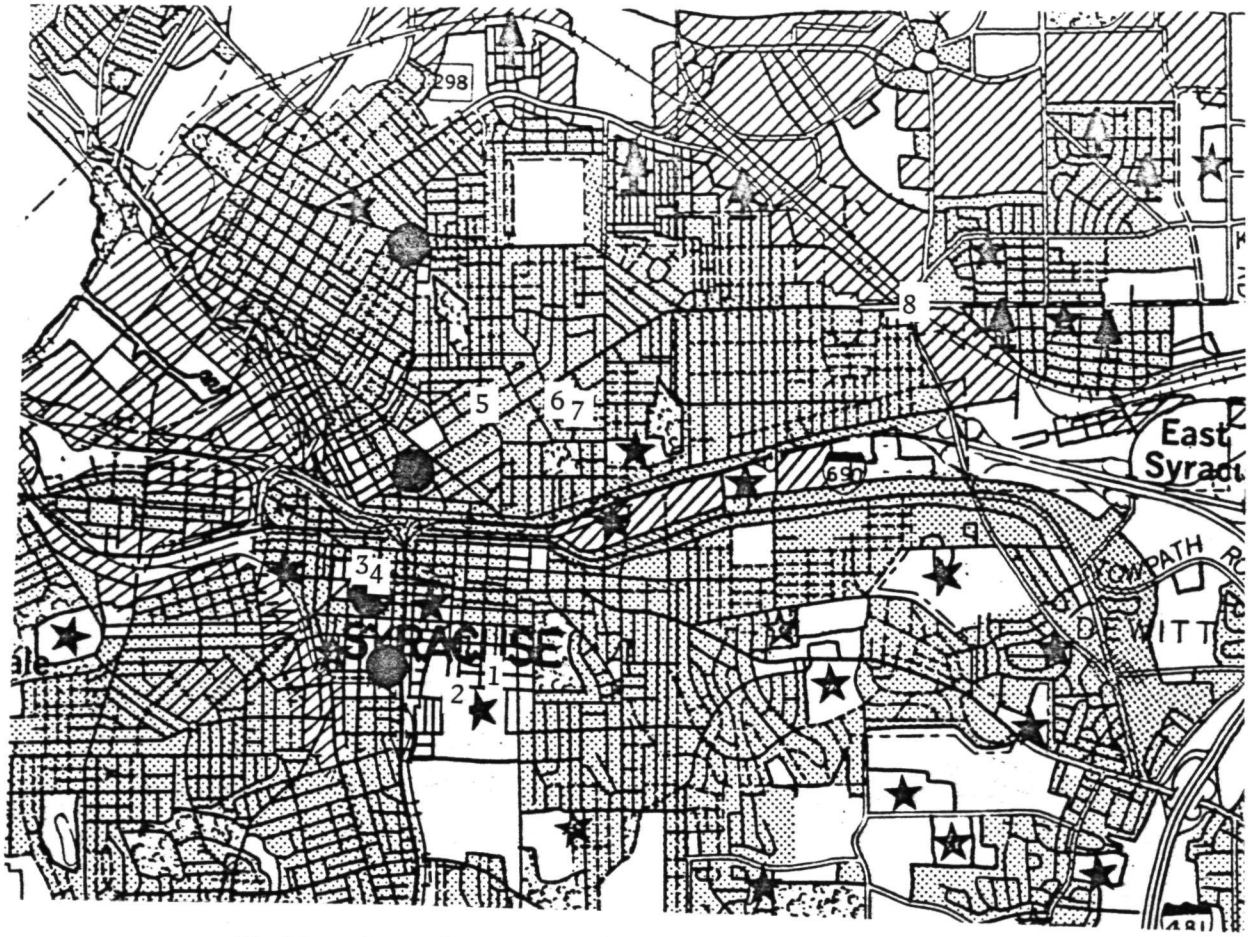

Station #	Day Temp. °C	Night Temp. °C	ΔT °C
1	14.3	2.8	11.5
2	21.0	4.2	16.8
3	19.0	6.9	12.1
4	17.9	3.8	14.2
5	19.6	4.7	14.9
6	19.9	1.1	18.8
7	17.4	3.7	13.7
8	17.5	4.0	13.4
Urban $\bar{x}$	18.0	4.4	13.6
Suburban $\bar{x}$	18.6	3.4	15.2

Figure 3-21. Ground Temperature Data Collected at Syracuse, New York - 2 November 1978

The ground data were collected to identify microscale variations in temperature within the urban center as well as to monitor general temperature gradients between the urban and suburban areas of Syracuse.

Most of the heat island analyses were performed using the ample data available from the HCMM satellite imagery. These data were supplied by NASA in both computer compatible tapes (CCTs) and hard copy film images. The CCTs were used for the heat island analyses because of the simplicity of scaling the digitized scene to any map or image base.

In order to examine the relationships between ground surface temperature and land cover/land use, the thermal images from the HCMM satellite were registered with high altitude U-2 color infrared photography over the particular urban areas being studied. Land use maps of the metropolitan areas proved to be insufficient for this purpose due to their generalization of classifications. The registration of the CCT thermal images to the U-2 photographs was straight-forward. Clearly identifiable points on both images, in particular distinctive land/water interfaces, were selected across the metropolitan area. The grid location of each point on each image was recorded and rectilinear transformation coefficients were determined.

The CCT digital data were converted to temperature space using the satellite's calibration. Computer software routines were developed and employed to generate isopleths at 1°C intervals within a scene. These isopleths were defined by their grid coordinates on the thermal image so that they could be easily regenerated via the rectilinear transformation coefficients to be registered with the U-2 photograph. Transparent overlays of these isopleths then provided a means for analyzing relationships between temperature patterns and ground cover within the heat island.

It was determined that temperatures corrected for atmospheric effects would not be required for our analysis of thermal patterns within any one urban area. The atmospheric calibration which is a linear correction would simply change the values of the thermal isopleths without affecting the thermal patterns of interest under this experiment. For this reason, temperatures used within the heat island experiment were determined solely by the satellite's calibration.

Overlays of temperature isopleths were generated for Buffalo and Syracuse from the 6 June 1978 images - both day and night. This date was chosen mainly because of the availability of a well-registered temperature difference image on this date. The temperature difference image was generated and provided by NASA in both CCT and hard copy image formats (HCMM Data Users Handbook, 1980); 2°C isopleths of temperature differences were generated from these data and a registered overlay was generated for the U-2 photograph of Buffalo. Figures 3-22 through 3-25 present some of the thermal maps generated for Buffalo and Syracuse. Isopleths containing only one satellite image pixel have been omitted for clarity.

The thermal maps generated from the HCMM satellite imagery provide a wealth of information relative to the urban heat island problem. This information can be analyzed in numerous ways to examine various characteristics of the heat island. Two general characteristics were investigated under this effort. The first of these was the overall macroscale effects of the urban heat island, that is , the overall changes in temperature due to ground cover, in particular between the urban area and the surrounding rural area. The second type of characteristic investigated involved the smaller effects of particular urban features such as urban parks, industrial complexes and residential districts and their effects on adjacent areas. Each of these two areas of investigation is discussed below.

Analysis of the thermal patterns observed within an urban heat island involves recognition of a complex array of variables and limitations. Small changes in temperature recorded on a thermal image can be real, non-real, or a combination of the two extremes. As discussed in Section 2.3, real changes in temperature can result from numerous variables including thermal properties of the ground cover, localized wind patterns, elevation, evaporative cooling, and generation of heat. On the other hand, entirely apparent changes in temperature can result from changes in surface emissivity or integration of various temperatures over one resolution element. Most of the analyses performed under this effort require consideration of all these parameters.

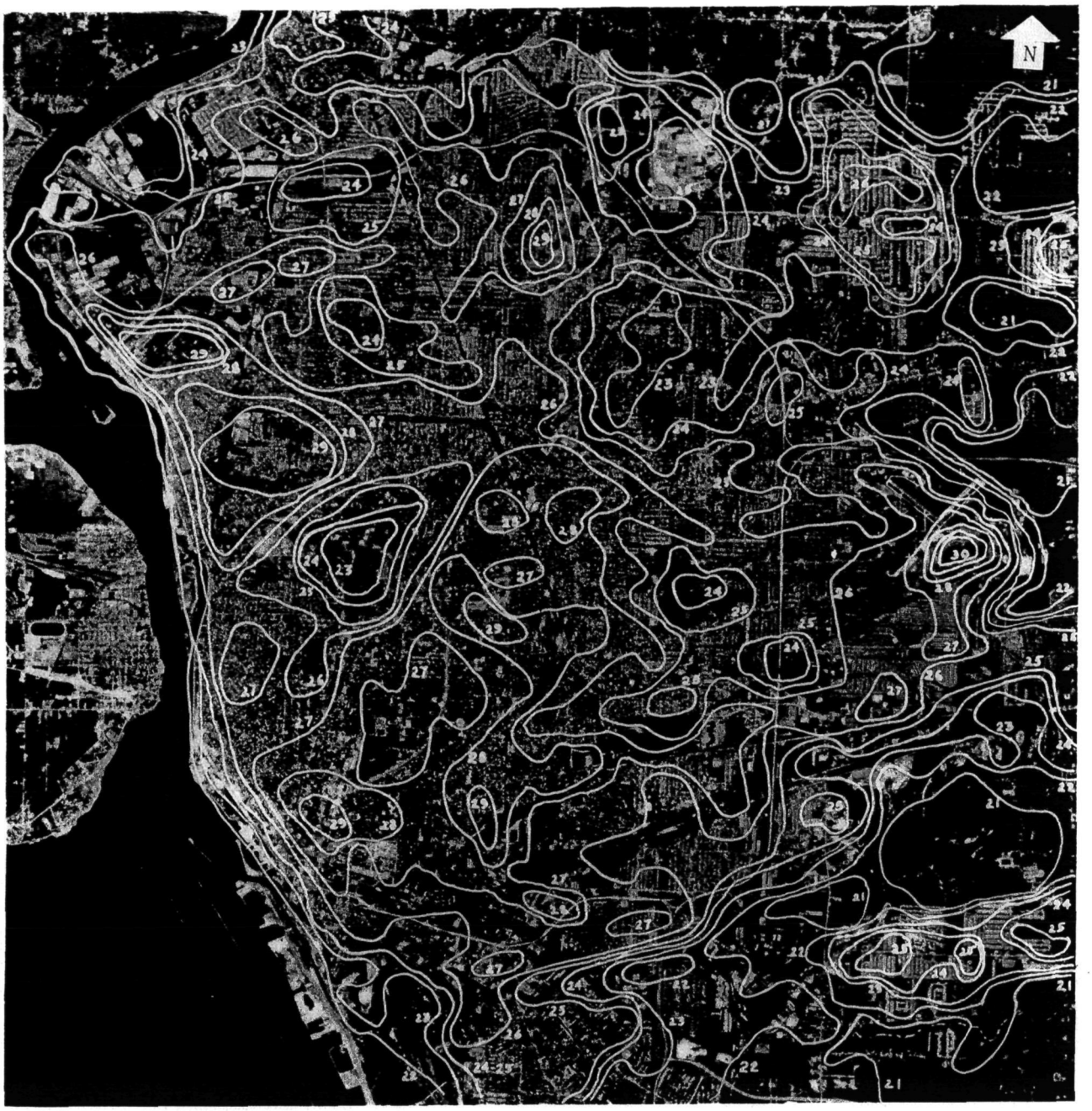

Figure 3-22. Thermal Map Overlay Showing Apparent Radiometric Temperatures For Metropolitan Buffalo, N.Y. - 6 June 1978 - 2 p.m. EDT. Each Isotherm represents a 1°C Change in Temperature as Recorded by the HCMM Satellite. Winds are from the SSW at 12 Knots.

Figure 3-23. Thermal Map Overlay Showing Apparent Radiometric Temperatures For Metropolitan Syracuse, N.Y. - 6 June 1978 - 2 p.m. EDT. Each Isotherm Represents a 1°C Change in Temperature as Recorded by the HCMM Satellite. Winds are from the SSW at 5 Knots.

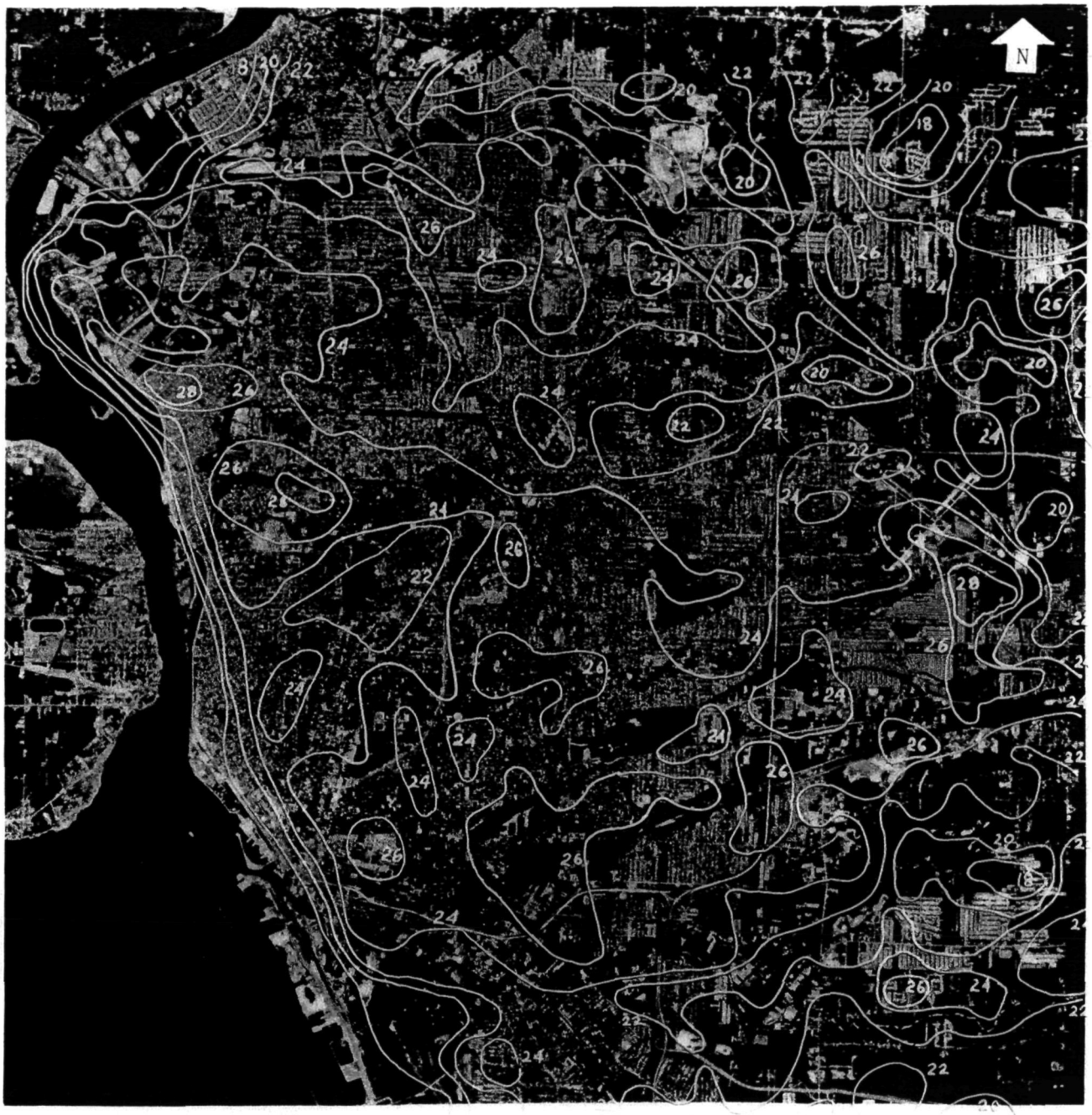

Figure 3-24. Thermal Map Overlay Showing Apparent Change in Temperatures For Metropolitan Buffalo, N.Y. Between 2 a.m. and 2 p.m. - 6 June 1978. Each Isotherm Represents a 2°C Change in the Temperature Difference Between the Night and Day Scenes as Recorded by the HCMM Satellite.

Figure 3-25. Thermal Map Overlay Showing Apparent Radiometric Temperatures For Metropolitan Buffalo, N.Y. - 6 June 1978 - 2 a.m. EDT. Each Isotherm Represents a 1°C Change in Temperature as Recorded by the HCMM Satellite. Winds are from the South at 6 Knots.

It should be noted here that the analyses performed under this experiment were conducted primarily on the 6 June 1978 day/night imagery of Buffalo and Syracuse, New York. As discussed in Section 2.3, a frequent contribution to the formation of a distinct urban heat island is an overcast sky capable of re-radiating escaping heat back into the urban area; of course, overcast conditions preclude clear satellite imagery of an area. The clear 6 June 1978 imagery does, however, indicate some degree of heat island development in the major urban areas; furthermore, registered day/night temperature difference images generated by NASA were also available for analysis for this date. So although this date may not provide the best example of a clear urban heat island formation, it provides a prime set of day, night, and day/night temperature difference images with which to investigate the thermal patterns seen within the urban complex.

The major characteristic of an urban heat island is, by definition, an increase in temperature within the urban area relative to the rural surrounds. This effect is observable directly from HCMM thermal images. Figures 3-26 and 3-27, for example, are thermal images of Buffalo and Syracuse, respectively. The brighter areas in these images correspond to higher temperatures. As can be seen, therefore, the metropolitan areas tend to be brighter than the rural areas surrounding the cities. This difference in temperature is predominantly due to the abundance of vegetation in the rural areas. The vegetation is physiologically capable of maintaining its temperature near that of the ambient air through evaporative processes. With this capability in mind, we would further expect that all rural areas would be roughly at the same temperature, and all non-rural areas composed of varying degrees of man-made materials would tend to be warmer due to the thermal properties of the denser man-made materials. The 24°C isopleth generated from the thermal image presented in Figure 3-25 corresponds remarkably with the interface between the Buffalo metropolitan area and its rural surrounds. This can be seen in Figure 3-28 which presents the entire thermal map generated for this scene. This illustration is basically the same as the map presented as Figure 3-22; in Figure 3-28, however, the 24°C isopleths have been emphasized and annotations referring to examples presented below have been added. (On the high altitude infrared photograph, vegetation will appear red due to its high infrared reflectance).

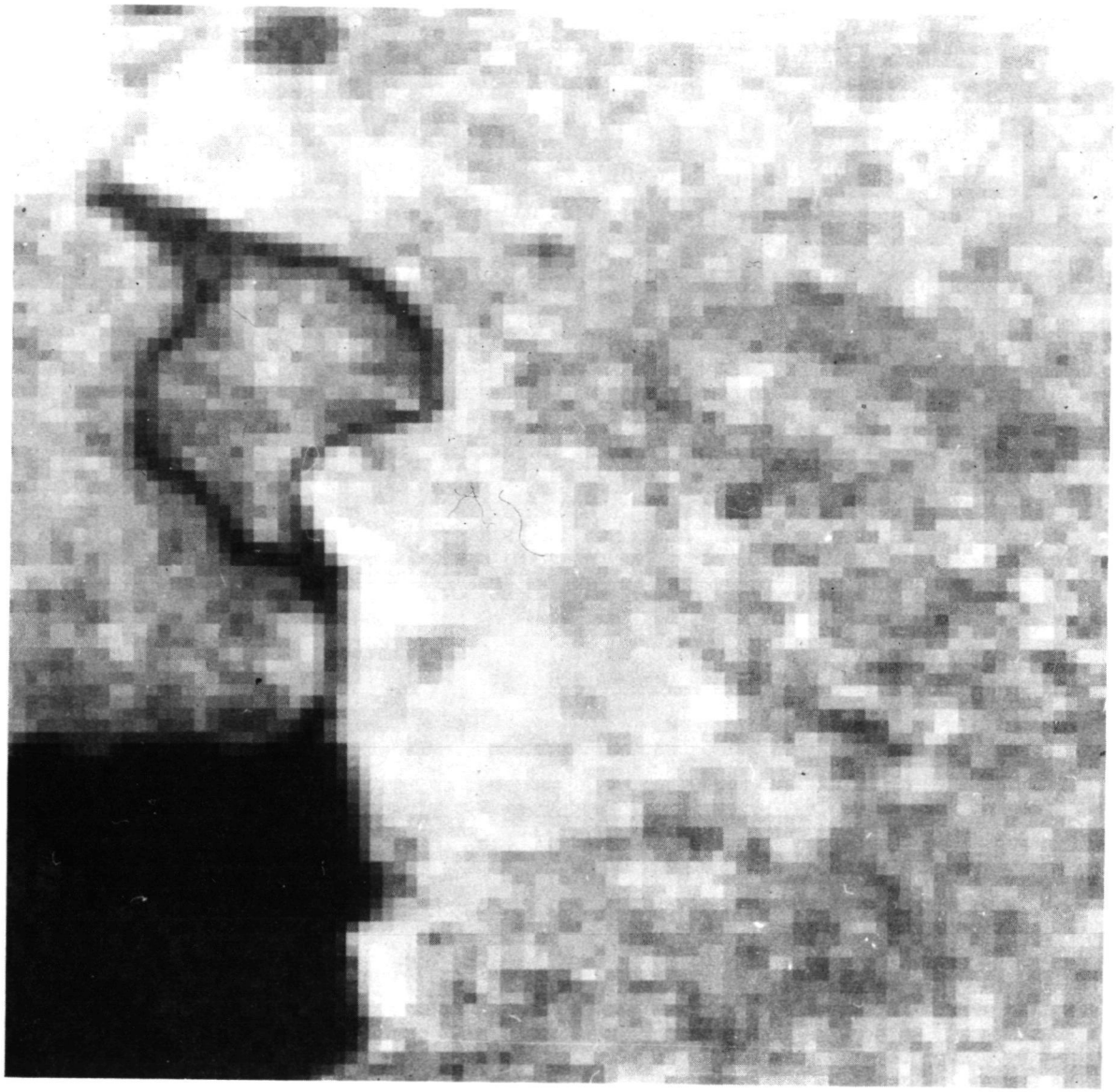

Figure 3-26. Thermal Infrared Image of Metropolitan Buffalo, N.Y. - 6 June 1978 - 2 p.m. as Recorded by the HCMM Satellite. The Warmer Metropolitan Area Appears Lighter on the Thermal Image than the Cooler Rural Surrounds. Lake Erie is in the Lower Left Corner of the Image. The Smaller Cities of Niagara Falls, N.Y. and Niagara Falls, Ontario Can be Seen Along the Niagara River Near the Upper Left of the Image.

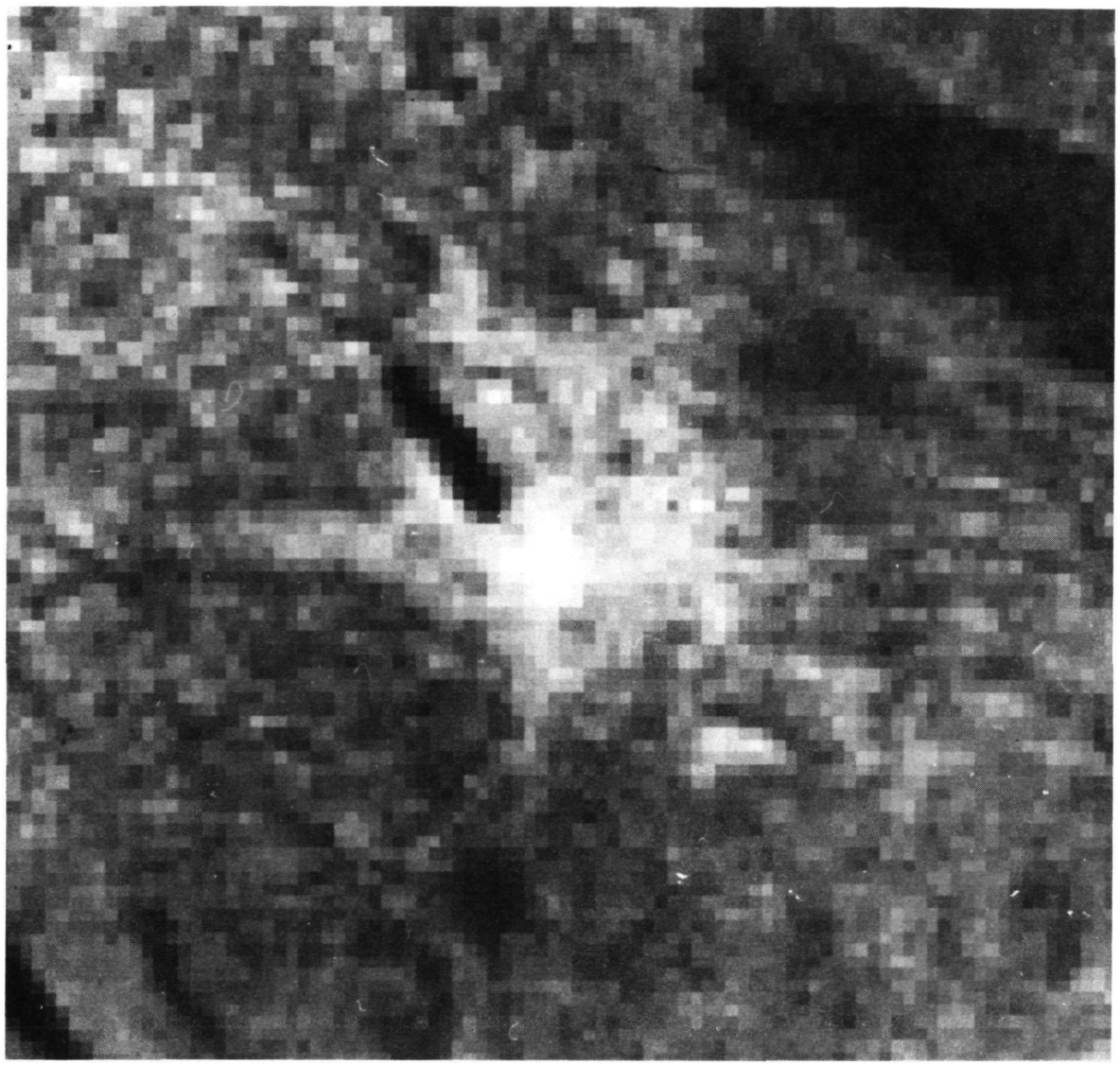

Figure 3-27. Thermal Infrared Image of Metropolitan Syracuse, N.Y. - 6 June 1978 - 2 p.m. as Recorded by the HCMM Satellite. The Warmer Metropolitan Area Appears Lighter on the Thermal Image Than the Cooler Rural Surrounds. Onondaga Lake lies Just to the Upper Left of Syracuse. Oneida Lake is in the Upper Right Corner of the Image.

Figure 3-28. Thermal Map Overlay Showing Apparent Radiometric Temperatures for Metropolitan Buffalo, N.Y. - 6 June 1978 - 2 p.m. EDT. Each Isotherm Represents a 1°C Change in Temperature as Recorded by the HCMM Satellite. The Bold 24°C Isopleth Corresponds Remarkably With the Change in Ground Cover From Urban to Rural. Areas A-J Show a Local Decrease in Temperature with an Increase in Tree Cover. Areas L and M Indicate a Change in Temperature Between Two Similar Residential Areas, One Being Contiguous With the Metropolitan Area and the Other Being More Isolated.

The cooling effects of vegetation can also be seen within urban areas themselves. A high correlation appears between the percent tree cover in an urban area and the corresponding temperature of that area. This is understandable and expected in that any given area is an integration of all the individual factors (e.g., trees, roofs, pavements) in the area, each of which exhibits its own thermal properties. The degree of influence of individual features cannot be examined using the satellite imagery due to insufficient resolution. However, some degree of heat exchange between features is expected at this scale in a way similar to the effects discussed below regarding larger urban features such as residential and industrial complexes and parks.

The correlation between tree cover and temperature mentioned above can be readily seen in Figure 3-28. (The amount of tree cover within the urban and suburban areas can be roughly interpreted by the "redness" of the area on the photograph). Five areas which show an appreciable increase in tree cover relative to surrounding areas are indicated as areas A, B, C, D and E on Figure 3-28. Each of the areas corresponds to a local decrease in temperature. To extend this point one step further, it can also be seen that highly vegetative areas within the metropolitan area (e.g., parks, cemeteries, and open areas) appear to be the coolest spots. Examples of some of these areas are indicated by areas F, G, H, I and J on Figure 3-28.

Investigation of the influence of individual urban features on the development of an urban heat island involves recognition of a complex array of variables and limitations as mentioned above. The contribution of these variables seems to become more important when finer details within the urban thermal pattern are examined. This will be evident in the subjects presented below. Because of the numerous variables involved and the limited depth of this study, the examples presented within this section generally cannot and are not intended to prove that certain conditions or phenomena exist. Rather, the examples are intended to provide a sampling of the numerous subjects of interest contained within the HCMM satellite thermal images of metropolitan areas. A thorough analysis of most of the subject areas would entail comparisons of each area under various wind, sky and temperature conditions.

Ground data collected in Syracuse indicate that significant changes in temperature can exist both between an urban center and its suburbs as well as within the urban center itself. This can be seen by examining the compiled ground temperature data presented in Figure 3-21. The temperature difference between station 1 and station 2 during the day is remarkable given that they are only a few city blocks apart. Likewise, the difference of 3.1°C between station 3 and station 4 during the night indicates a substantial variation in temperature within one city block. The general tendency of the suburban areas to cool more than the urban center at night is also observable through these data. Although ground truth data were not collected in the rural areas surrounding the Syracuse metropolitan area, it is expected that these areas would cool down even more than the suburbs.

HCMM satellite imagery can be used to observe most of the temperature variations in and about a metropolitan area such as Syracuse. The 0.5 kilometer resolution of the imagery does, however, limit examination for some of the finer variations. A discussion of observable variations and patterns follows.

The general tendencies of residential areas contiguous to the metropolitan area (e.g., area M in Figure 3-28) to have higher temperatures than the isolated residential areas (e.g, areas K & L in Figure 3-28) indicates that the urban core and industrial districts do have a general effect of raising the temperatures of adjacent areas. This difference in temperature due to proximity to warmer or cooler areas can be seen by comparing the average temperature of two areas - areas L and M in Figure 3-28 for example. The average temperature of area L is roughly 24°C while the average for area M is 26°C. This difference in temperature is most likely a result of both the cooling effects due to the rural surrounds of area L and heating effects associated with the proximity of area M to hotter areas.

Another characteristic of the thermal patterns found around the urban area is the tendency for isotherms to occur in loose concentric rings, particularly within isolated residential spots such as area L on Figure 3-28. This type of phenomenon, along with the example just cited, support the idea that one area can tend to affect the temperature of adjacent areas. This effect is most likely due to one of two phenomena which are

illustrated in Figure 3-29. First, any wind present will tend to move cool ambient air from vegetated areas into adjacent urban areas helping to cool them down. And similarly, hot ambient air from within urban areas can be removed to rural areas capable of cooling the air through evapotranspiration. The second method by which adjacent areas may tend to affect one another is through interaction by an overcast sky. This condition is more likely to occur given the common conditions associated with heat island formation as discussed in Section 2.3. In this case heat emitted from each point in an urban area will tend to be re-radiated back to the earth, but in an effectively larger area than the source. A point within an urban area which is surrounded by further urbanization will therefore be loaded by the energy emitted by these surrounds and re-radiated back by cloud cover. An urban point near a rural area will however receive a lesser loading due to the decrease in energy emitted by the cool rural area. In effect, this phenomenon would defocus sharp changes in temperature between two areas. As the sky and atmosphere become clearer and as winds decrease, these effects would decrease, resulting in a "sharper" thermal map. This does not mean that temperature differences between rural and urban areas would be more drastic, but rather that the change would occur over a shorter distance at the interface between the two areas. In fact, as discussed earlier, as the sky becomes more overcast and the heat island develops more intensely, the temperature differences between the entire metropolitan area and the rural surrounds will increase. The changes in temperature over smaller areas such as urban parks will however be less drastic as a result of the overcast sky. This is illustrated in Figure 3-30 where a theoretical temperature profile across an urban area is presented for both clear and overcast sky conditions. Wind in both cases is assumed to be negligable.

Five subject areas of interest are presented and discussed below. Due to the large number of variables affecting the temperature of an area and the multitudinous isopleths delineated for each metropolitan area (see Figures 3-22 through 3-25), only a portion of the thermal map in the immediate area being examined was used. In analyzing these individual areas,

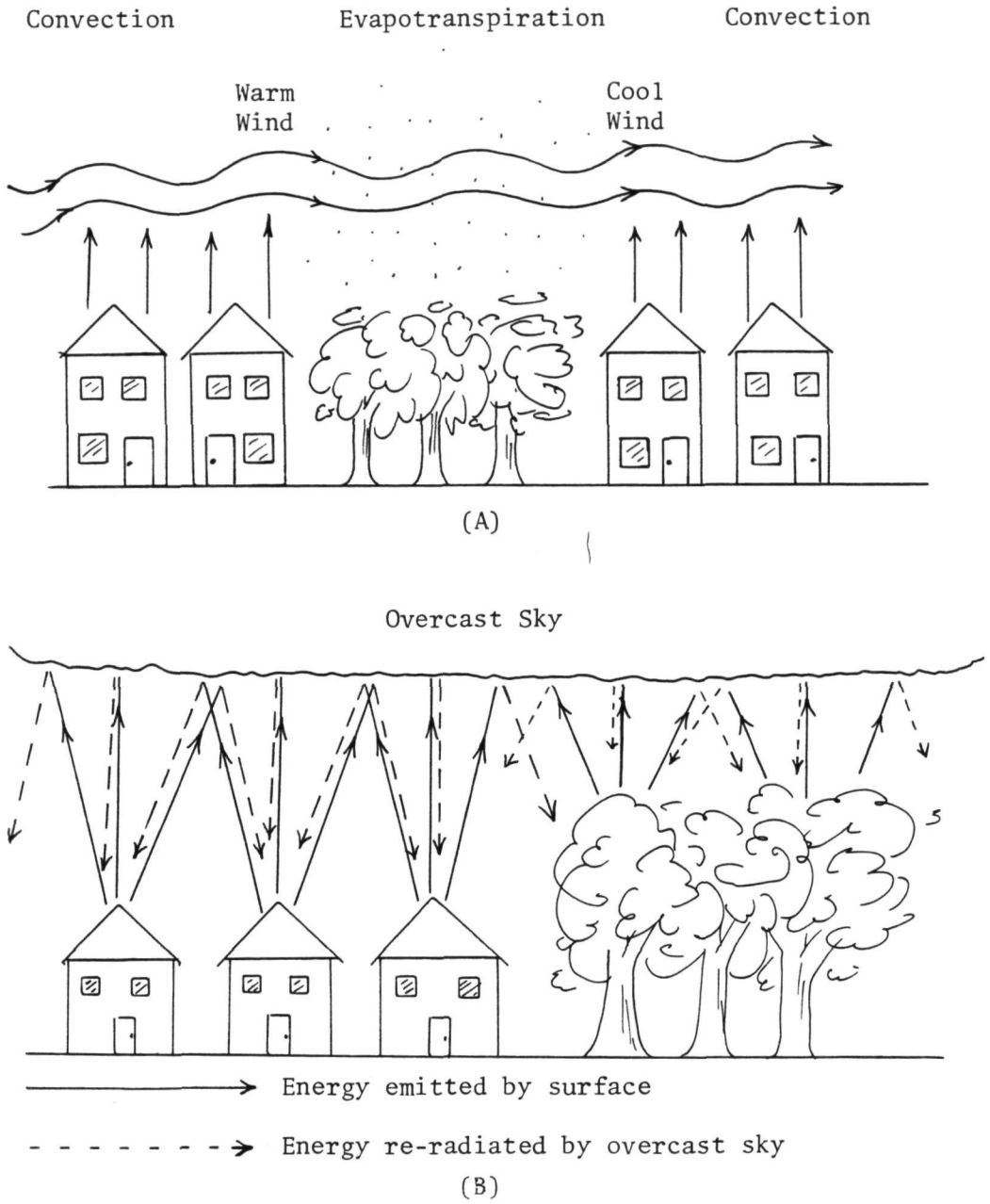

Figure 3-29. Two Methods by Which an Area Can Affect The Temperature of an Adjacent Area. In Illustration A, Moving Air Permits Convective Cooling in Urban Areas; Rural Areas or Green Spots Within the Urban Area Are Capable of Cooling the Air Through Evapotranspiration. In Illustration B, Energy Being Emitted by the Surface is Re-radiated Back to the Surface by an Overcast Sky But in An Effectively Larger Area Than the Source. Thus the Total Radiation Incident Upon Any Surface is a Function of the Energy Emitted by Neighboring Areas.

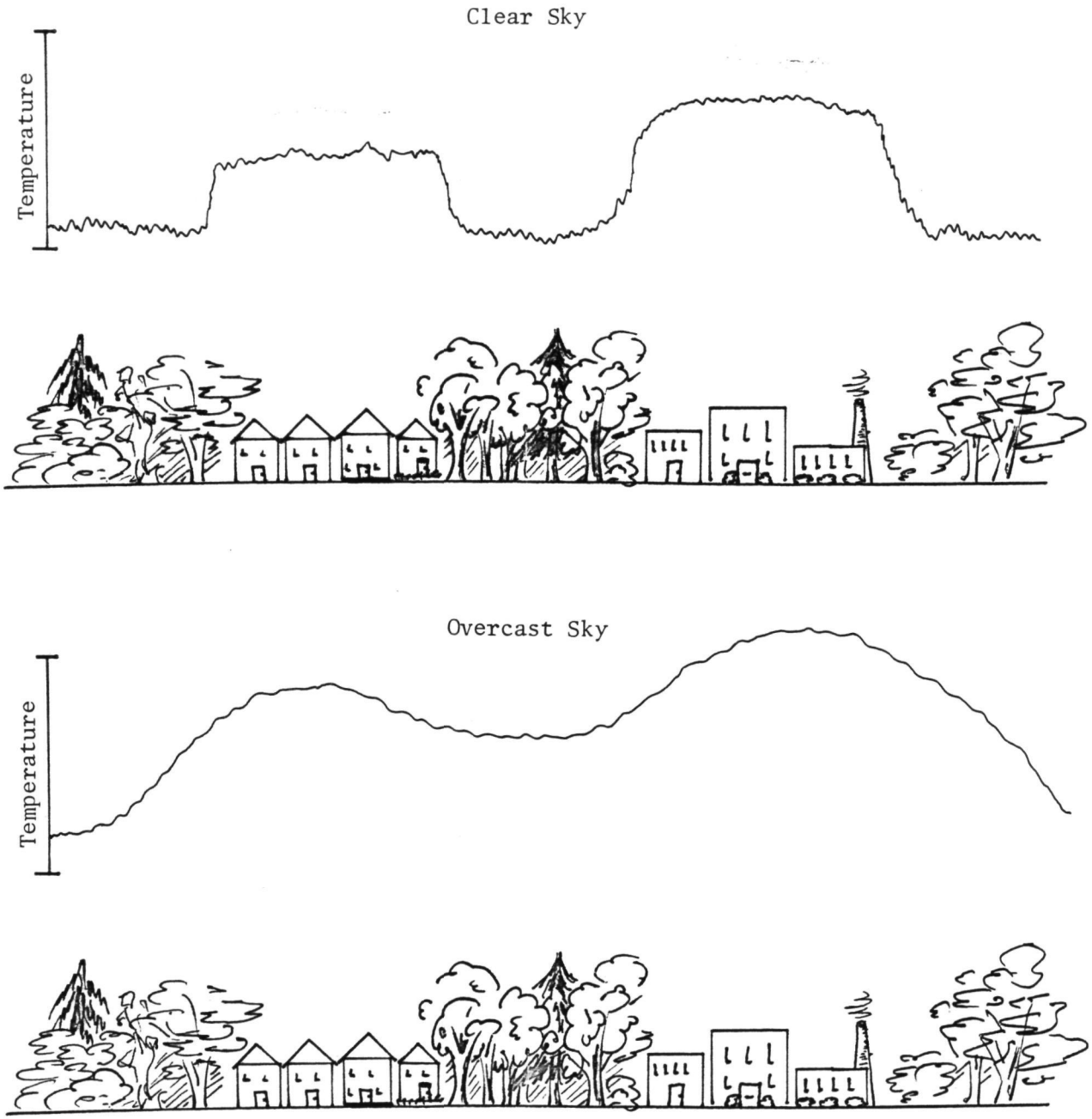

Figure 3-30. Effect of Overcast Sky Conditions on Thermal Gradients Between Areas of Differing Ground Cover. Because of the Overcast Sky's Ability to Absorb and Reradiate Energy Emitted by the Surface, the Overall Temperature at the Surface Remains Higher than Under Clear Sky Conditions; Furthermore, Higher Heat Loss by One Area Tends to Affect the Temperature of Adjacent Areas Through Interaction of the Overcast Sky.

it was determined that concentration on the immediate area was essential; attempts to visually interpret all the factors and interactions over larger areas tended to yield confusion.

The five subject areas are presented in Figure 3-31. These five subjects are all taken from the 6 June 1978 - 2 p.m. image of Buffalo. The wind was from the SSW (240°N) at 12 knots. A discussion of each of the five subjects follows.

SUBJECT I (see Figure 3-31)

Subject I is the lower portion of the contiguous area comprising both Subjects I and II. In this area, the two residential areas A and B are similar with respect to density and tree cover. The two areas differ in temperature by 2°C. Given that the wind is out of the SSW, it is reasonable to expect that this difference in temperature is due to differences in the ground cover type upwind from areas A and B. Area A is influenced by a warm air flow coming from additional residential and commercial districts located at C. Area B, on the other hand, is influenced by a cool air flow coming from the large open fields and railyards located directly upwind from there at D.

SUBJECT II (see Figure 3-31)

Subject II is the area just northeast of Subject I and is similar to that presented in Subject I. In this case, the entire residential area comprising the subject area is reasonably constant relative to density and tree cover. The gradient in temperature across this area normal to the wind direction appears to reflect the changing ground cover found upwind of the area. The large open area and railway yard at G appears to effect a cooler swath into the residential district. In the absence of any potential "cooling" area upwind from F, this portion of the residential district remains warmer than area E.

As discussed earlier, the resolution of the satellite imagery limits analysis of these temperature patterns. In this subject, for example, the 25°C isopleth at E may truly reflect a decreased temperature

Figure 3-31. Thermal Map Overlay Showing Apparent Radiometric Temperatures For Metropolitan Buffalo, N.Y. - 6 June 1978 - 2 p.m. EDT. Each Isotherm Represents a 1°C Change in Temperature as Recorded by the HCMM Satellite. Selected Subject Areas are Shown Which Demonstrate the Effects of Particular Urban Features (e.g., Parks and Commercial/Industrial Districts) on the Temperature of Adjacent Areas.

for that small portion of the residential area or it may result from an integration of both the residential area and part of the open area at G. (This isotherm encompasses two satellite image pixels).

SUBJECT III (see Figure 3-31)

Subject III involves the influence of a large urban park on local temperatures. The large park located at J is centered between a large industrial district, K, and a dense residential/commercial portion of the urban core, L. The large uniform residential area labeled M is apparently affected by both areas J and K which are located upwind from M. The more obvious effect on this large residential area is the increased temperature at the west end adjacent to the industrial district, K. However, an apparent large scale cooling process can also be seen if area M is compared to area N which lies just southeast of M. Area N is not influenced by the large urban park, but instead receives an air flow passing over the dense residential/commercial area, L. Upon initial examination of the two residential areas, M and N, one might expect area N to be cooler because of the increased tree cover within that area. However, apparently because of the additional effect of adjacent urban features, J and L, area M is the cooler of the two areas.

SUBJECT IV (see Figure 3-31)

Subject IV involves the effects of a hot commercial center on the surrounding areas. The "hot spot" in this case is a large complex of commercial buildings dominated by large department stores and malls located at O. The heat being emitted by this area appears to be increasing the temperature of the adjacent residential area to the west. The open areas to the east, P, are capable of cooling some of the heat coming from area O through evaporative processes, but a gradient in temperature can also be seen on this side as the distance from area O increases across the open areas at P. This subject demonstrates well the concept that heat from one area may have an influence on adjacent areas.

SUBJECT V

Subject V is not labelled on Figure 3-31 for the sake of clarity in the illustration. It concerns area R located between Subjects I and II. This is an example of a thermal pattern which does not appear to be so easily explained. Area R is 2°C cooler than the similar residential areas, S and T, located to either side. The only apparent reason for this temperature pattern is the collection of small parks located upwind from and within area R. Other small parks around the metropolitan area do not however seem to have so great an effect. This can be verified by the reader's examination of Figure 3-28.

This subject is presented to illustrate that thermal patterns resulting from less obvious factors are also contained within the HCMM satellite imagery. Proper examination and analysis of these features are necessary if valuable information regarding the development and possible alteration of urban heat islands is to be obtained from the HCMM imagery.

The subjects presented above indicate that considerable information about the thermal properties of urban heat islands is contained within the daytime images provided by the HCMM satellite. Similar subjects of interest can be identified in the night and day/night images as well. Individual subjects are not called out for each image studied under this effort. A sample of some of the other images examined has however already been presented in Figures 3-23 through 3-25. Examination of these illustrations will confirm that numerous additional points of interest are contained in the imagery.

Further investigation and examination of the thermal patterns imaged by the HCMM satellite from day to day under various sky, wind, and temperature conditions could identify the importance of particular urban features such as parks, open fields and tree-lined streets. A better understanding of the influence of these features on the urban heat island could

play an important role in future urban planning relative to decreasing excessive heat within urban areas and thus decreasing the discomfort and health hazards associated with it.

A summary of the conclusions drawn from this experiment is presented in Section 4.3.

Section 4

RESULTS

This section discusses the results of each experiment conducted to assess the utility of HCMM data. In each case the HCMM data provided new and often unique insights into the problem being studied.

4.1 HCMM's Role in Surface Temperature Measurement

The HCMR was calibrated on several passes using the underflight method described in Section 3.1. Table 4-1 contains calibration data for the underflights. These data were analyzed to determine if meteorological or path length variations had a strong influence on the calibration coefficients. Slant path length to the study site never varied by more than 10% from the nominal flying height of the space craft. Presumably because of this small variation, path length effects did not contribute significantly to the variation in calibration coefficients. There did appear to be some correlation between visibility and the intercept term (b of Table 4-1) which is related to the amount of path radiance. The limited amount of data precluded a quantitative analysis; however, the plot shown in Figure 4-1 indicates that the term related to path radiance tends to increase with decreased visibility (particularly under low visibility - high temperature conditions). The observations are in keeping with our expectation since the amount of precipitable water is a significant factor affecting visibility and the dominant factor affecting absorption and reradiation in the 10.5-12.5 μm bandpass observed by HCMM.

The calibration parameters derived from the underflight data were used to predict surface temperatures at points where ground temperatures had been determined from the aerial thermography. Figure 4-2 is a plot of surface temperatures as determined from aircraft data (after Schott 1979) versus temperatures obtained by applying the regression analysis to the satellite data. Data from four underflights are included in Figure 4-2. The residual error in the satellite temperatures was determined to be 1.0°C for 28 points.

Table 4-1. Calibration Data for HCMM Underflights

	Aircraft Altitude (AGL)	τ^*	Satellite Slant Range (Km)	Ground to Satellite** Temp. Coefficients m	b	Air Temp. °C (°F)	Visibility (mi.)
5-22-78 Day							
Rochester	8000'	.73	644	-	-	19 (66)	10
Syracuse	4000'	.773	673	-	-	21 (70)	20
9 Mile	8000'	.69	666	.71	-3.12	-	-
Olcott	4000'	.73	620	.64	-2.66	-	-
6-6-78 Day							
Syracuse	4000'	.708	620	-	-	22 (71)	20
9 Mile	4000'	.653	620	.65	-.572	-	-
6-6-78 Night							
Buffalo	6000'	.71	620	.71	.202	14 (57)	7
Rochester	4000'	.87	622	.66	-1.231	13 (56)	8
Syracuse	4000'	.87	638	.70	-.629	12 (54)	10
8-14-78 Day							
Rochester	6000'	.68	657	.70	13.41	33 (91)	7 (Haze)
Syracuse	6000'	.62	633	-	-	30 (86)	5 (Haze)
11-1-78 Day							
Syracuse	6000'	.712	637	-	-	12 (53)	20

* 8-14 μm transmission to flight altitude

** $T_{satellite} = mT_{ground} + b$ (T in °C)

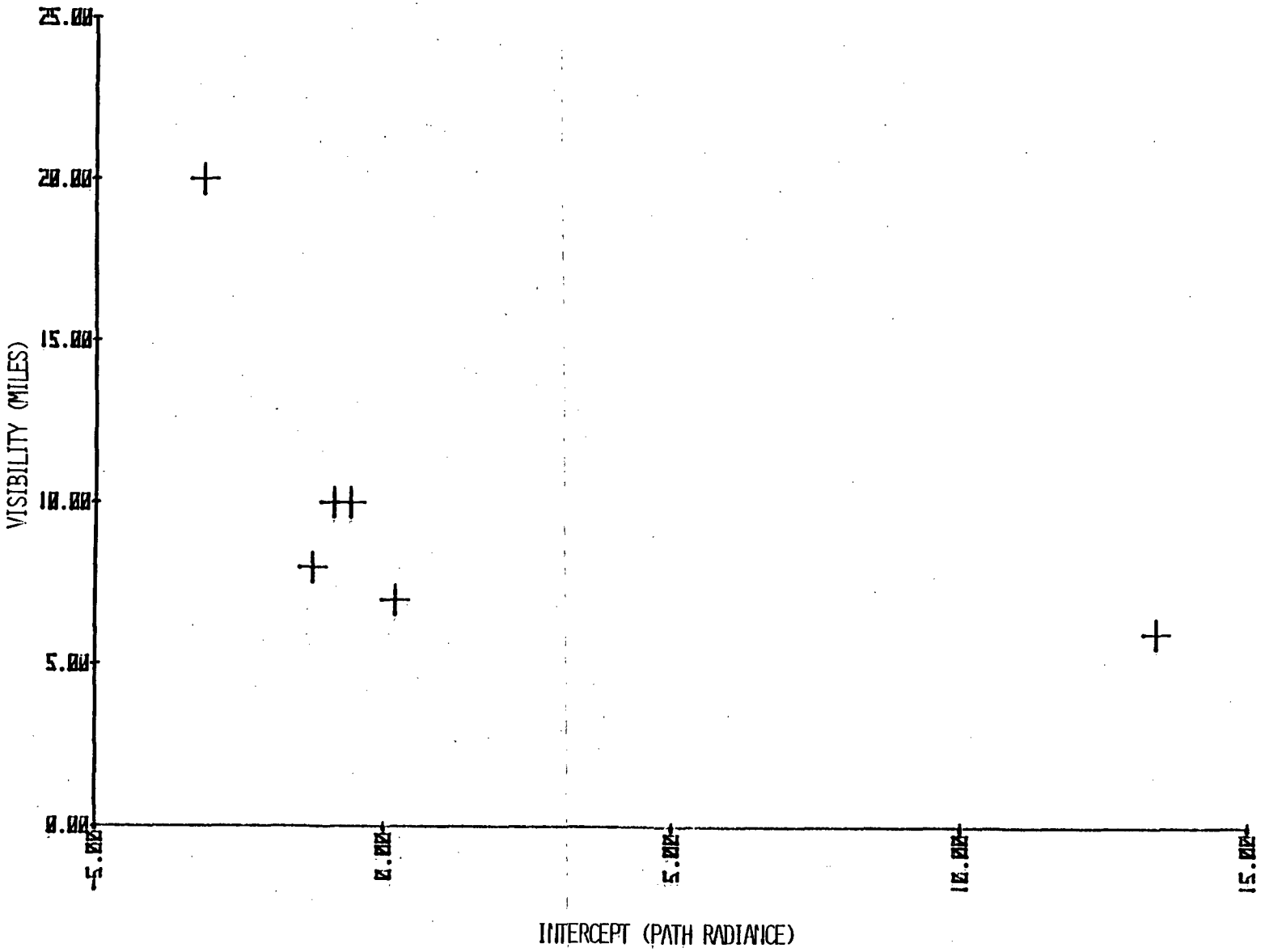

Figure 4-1. Plot of Satellite Calibrated Offset Values vs. Visibility

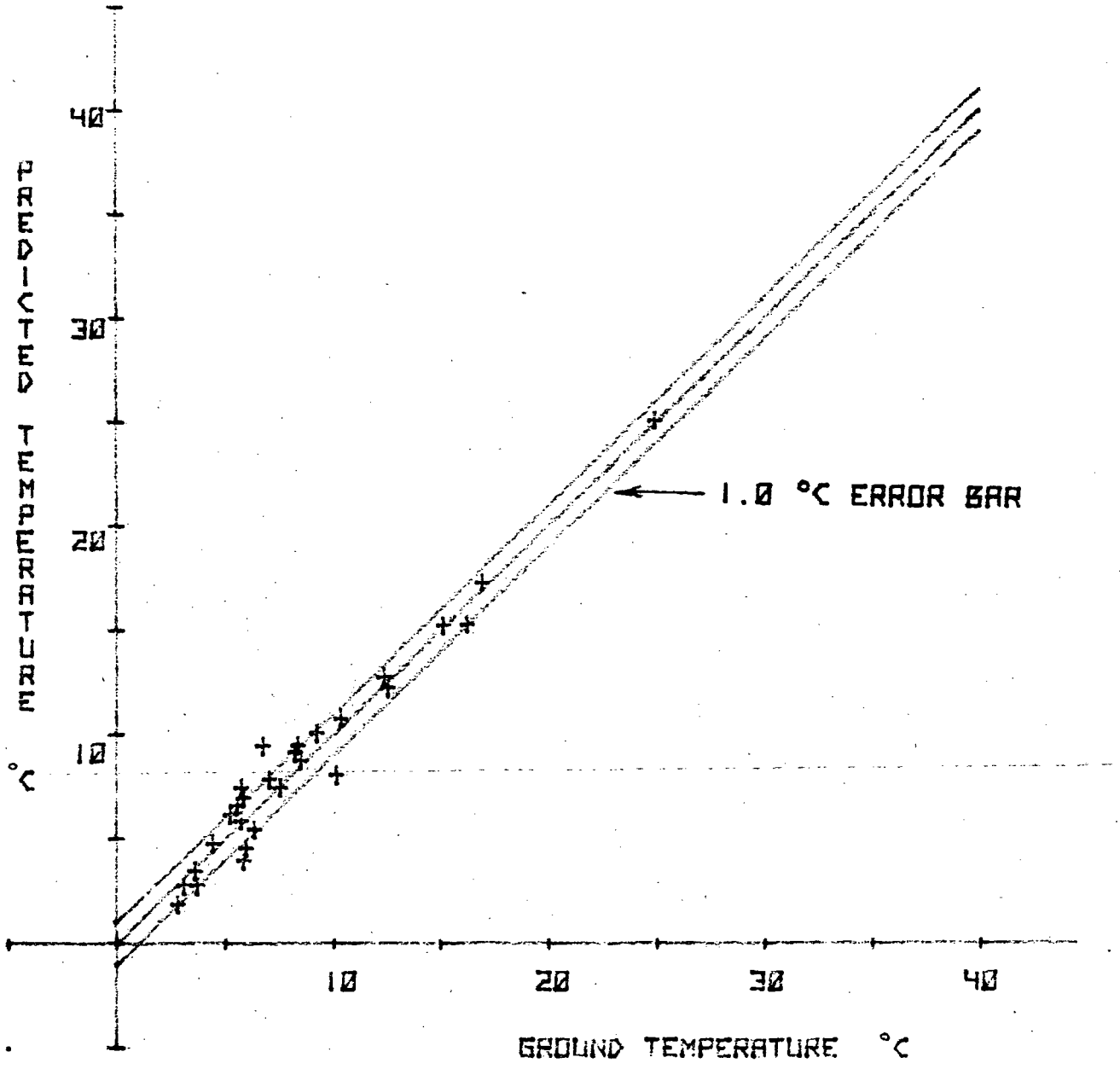

Figure 4-2. Plot of Satellite Data Corrected for Atmospheric Effects vs. Water Surface Temperature. Predicted Temperatures were Obtained by Correcting HCMR Data for Atmospheric Effects Using Coefficients Determined from the Aerial Underflight Calibration Technique. Ground Temperatures were Determined from Aerial Thermography. The Residual Error in the Satellite Temperatures is 1.0°C as Indicated by the Error Bars.

Schott 1979 had previously determined the expected error in the aerial measurement of temperature to be 0.4°C. This yields an overall error in satellite measurement of water temperature of 1.1°C for the underflight calibration approach. In addition to the underflight calibrations the LOWTRAN and RADTRA atmospheric models were run on several days when underflight data were available. The models were run with radiosonde input data from the Buffalo International Airport. An example input data set is shown in Table 4-2 for August 14, 1978 at 7 p.m. EDT. In general, radiosonde data at 7 a.m. and 7 p.m. bracketing the HCMM overpass times were used to determine if a reasonably stable atmosphere appeared to exist. If no significant variance (a change in predicted temperature of less than about 1°C was considered insignificant) existed between the calibration parameters generated by the radiosonde data, occurring just before or after the HCMM overpass, then these data were assumed to be applicable to the HCMR data.

Calibration parameters for several HCMM overpasses are shown in Table 4-3. In general, the LOWTRAN and RADTRA models which draw on the same basic assumptions produce quite comparable results. The empirical data obtained from the extensively tested underflight method exhibits significant variation from the model results. Figure 4-3 is a plot similar to Figure 4-2 showing the water surface temperature as measured from quantitatively calibrated aircraft underflights plotted against water surface temperatures predicted by the various HCMR calibration methods. In general, we see that for the four data sets combined here the empirical data correlate quite well as expected. The data from the LOWTRAN and RADTRA models exhibit considerable error. Indeed when we combine the errors associated with the difference between the satellite predicted values and the ground truth generated from the aircraft, with the error inherent in the ground truth itself, the errors associated with satellite measurement of surface temperature are 9.0°C and 6.9°C for LOWTRAN and RADTRA compared to the 1.1°C value previously computed for the underflight calibration method.

Table 4-2

Radiosonde Input Data For Atmospheric Models

August 14, 1978 - 7 p.m. EDT
Buffalo International Airport

Altitude (km)	Pressure (mb)	Temperature (°C)	Dew Point (°C)
0.218	994.6	30.0	16.1
0.984	912.0	22.9	12.7
1.313	878.0	19.0	12.7
1.591	850.0	16.9	10.9
1.763	833.0	16.7	4.6
1.929	817.0	16.5	2.8
2.452	768.0	12.8	1.4
2.618	753.0	12.6	2.3
2.923	726.0	10.4	3.5
3.050	715.0	9.3	3.2
3.226	700.0	8.4	2.1
3.526	675.0	6.3	0.3
3.809	652.0	4.0	-0.8
3.885	646.0	3.9	-2.1
4.128	627.0	5.1	-11.7
4.299	614.0	3.5	-12.1
4.512	598.0	2.4	-27.6
5.794	509.0	-6.0	-36.0
5.934	500.0	-6.0	-36.0
6.188	484.0	-7.5	-37.5
6.350	474.0	-8.4	-38.4
7.645	400.0	-17.3	-47.3
9.296	319.0	-30.7	-60.7
9.590	306.0	-33.5	-36.0

Table 4-3

Atmospheric Calibration Parameters

Date/Site/Time		Calspan*		RADTRA*		LOWTRAN*	
		m	b	m	b	m	b
6 June 1978							
Buffalo	200 EDT	0.708	0.202				
Buffalo	700 EDT			0.853	1.135		
Buffalo	1900 EDT			0.844	2.287	0.836	1.47
Rochester	200 EDT	0.659	1.231				
Syracuse	200 EDT	0.694	0.629				
Nine Mile	1400 EDT	0.653	0.572				
22 May 1978							
Buffalo	700 EDT			0.885	0.646		
Olcott	1400 EDT	0.64	2.66				
Nine Mile	1400 EDT	0.69	3.12				
14 August 1978							
Buffalo	700 EDT			0.545	7.59		
Buffalo	1900 EDT			0.562	7.83	0.576	4.38
Rochester	1400 EDT	0.684	13.41				

* Where $T_{satellite} = mT_{surface} + b$ (T in °C)

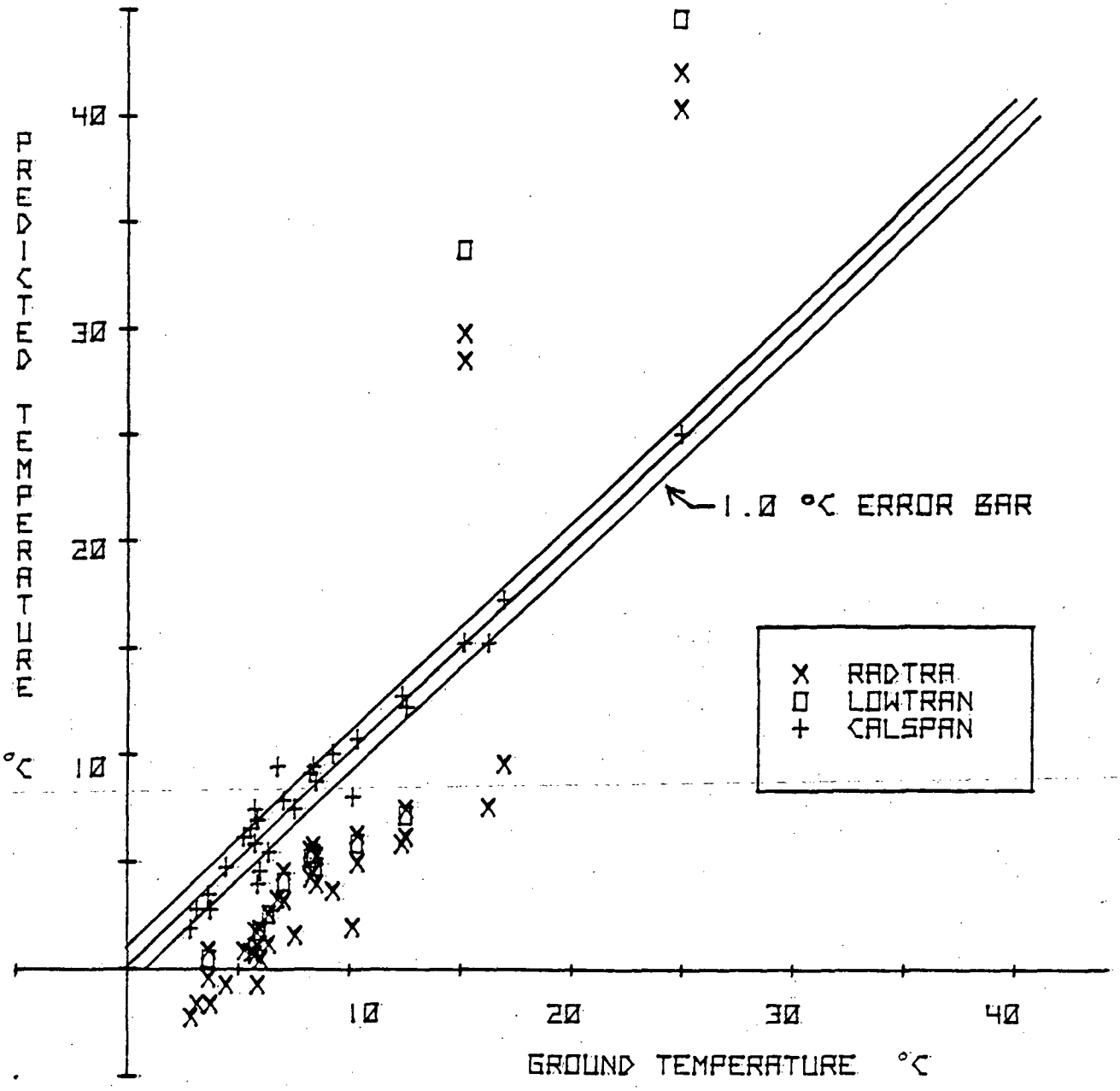

Figure 4-3. Plot of Water Surface Temperature vs. Temperatures Predicted by Various HCMR Calibration Methods. The Residual Error in the Predicted Temperatures Using Calspan's Underflight Calibration Technique is 1.0°C. The Residual Errors Associated With the LOWTRAN and RADTRA Models are 9.0°C and 6.9°C Respectively.

These results indicate that the HCMR can be calibrated for absolute surface temperature measurement using the underflight calibration technique. In addition it appears as though in most cases the atmospheric propagation models are not capable of accurate calibration of satellite sensing systems.

There has been some question about changes in the radiometric calibration of the HCMR after launch. Our data do not support or disprove this possibility. The distribution of the satellite predicted temperatures using the atmospheric propagation models tends to indicate that if the models were extremely precise then both a gain and offset correction to the HCMR calibration has been introduced after launch. We believe that barring any supportive evidence of a change in the sensor calibration it is as likely and perhaps more likely that inadequacies in the atmospheric propagation models are introducing the apparent errors in HCMR calibration.

4.2 HCMM's Role in Observing Regional Water Resources

The general formation and development of the thermal bar can be qualitatively studied by visual analysis of HCMR imagery. In addition, by utilizing the results of the underflight calibration method presented in the previous subsection, it is possible to generate detailed quantitative maps of the surface thermal structure of entire lakes. The actual location and rate of development of the thermal bar can be mapped after the HCMR data have been corrected for atmospheric effects. Figure 4-4 is a map of the surface temperatures of Lake Ontario showing the location of the thermal bar on 6/6/78. Knowing the location of the thermal bar it is possible to map water quality indicators in the vicinity of the bar to determine its effects on water quality. In Figure 4-5 the magnitude of the red to green brightness vector from the Landsat satellite has been mapped for a portion of Lake Ontario. The brightness vector is a measure of the overall turbidity of the water and therefore represents a rough measure of the combined algae and suspended particulates (an indicator of nutrients) in the water. Also shown in Figure 4-5 is the calibrated thermal data from 6/6/78 for comparison to the Landsat data from 6/14/78. The thermal bar's effect on water quality is clear from Figure 4-5. The warm nutrient-rich water is trapped inshore

SURFACE RADIOMETRIC TEMPERATURE (°C)
LAKE ONTARIO
6 JUNE 1978 - 200 EDT

Figure 4-4. Thermal Map of Lake Ontario from Calibrated HCMR Data - 6 June 1978 - 2 a.m. EDT.

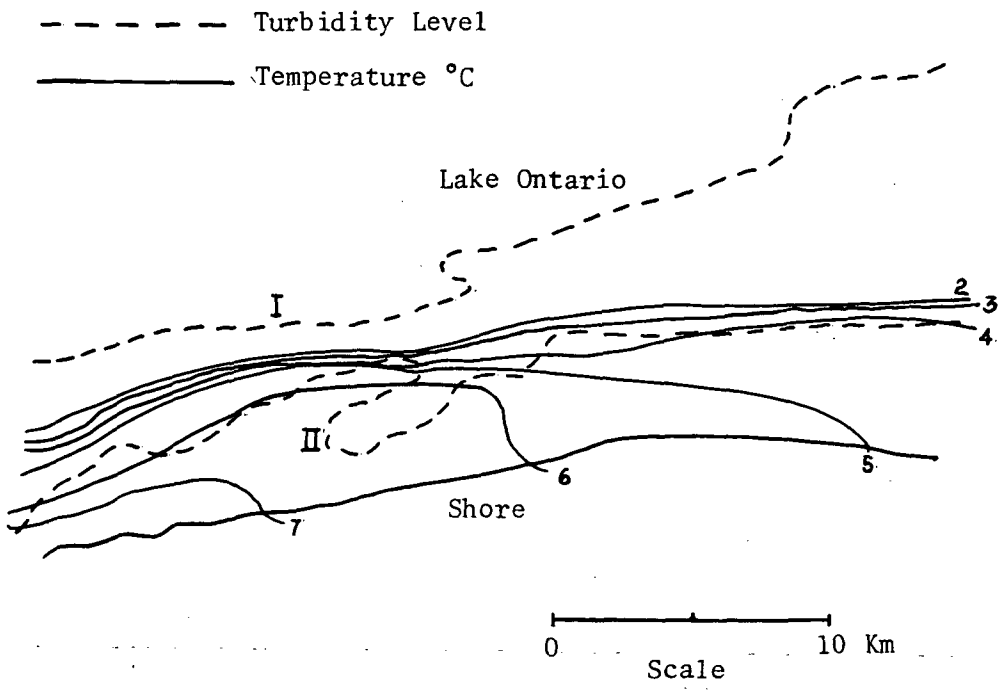

Figure 4-5. Red to Green Brightness Vector from Landsat Image of Lake Ontario - 14 June 1978. The Brightness Vector is a Measure of the Turbidity of the Water; Two Levels of Turbidity are Presented Above. The Additional Thermal Data Illustrate the Relationship Between the Thermal Bar and Water Quality. Warm Water Trapped Inshore of the Thermal Bar Provides an Excellent Medium for Algal Production Evident in the Higher Turbidity Level Near Shore. Note that the thermal data presented is from 6 June 1978 and some outward movements of the bar might be expected by the 14 June date of the Landsat overpass.

of the thermal bar providing an excellent medium for algal production. As we discussed in Section 3.2, aerial underflight data analyzed using the method of Piech and Schott (described in Appendix B) indicated that the major change in water color (turbidity) was associated with increases in algal concentrations. In addition to limiting dilution throughout the lake, thereby increasing nutrient values, pollution concentrations associated with runoff are also increased. In fact in extreme cases the elevated algal concentrations can increase to bloom proportions and become pollution problems themselves.

The effects of the thermal bar on water quality was verified by data taken during the week of 6/5/78 to 6/9/78 corresponding to the HCMM day/night overpass of 6/6/78. The data were obtained from the Canada Center for Inland Waters (CCIW) which had collected it as part of a regularly scheduled cruise of Lake Ontario. Figure 4-6 shows the pattern of the CCIW's permanent sampling stations around the lake. Also shown in Figure 4-6 are CCIW's water surface temperatures, secchi depths and integrated chlorophyll concentrations (where available) for several stations of interest. We have also shown in Figure 4-6 the location of the thermal bar as determined from the calibrated HCMR data of 6/6/78. It is readily apparent from this figure that the CCIW data, taken over a 5 day period including the HCMM overpass date, verify the utility of the calibrated HCMR in locating the thermal bar. These CCIW data also verify the interpretation of the auxiliary Landsat and underflight data relative to water quality. The CCIW data clearly point to a turbidity increase associated with dramatically elevated chlorophyll levels occurring inshore of the thermal bar. Regretably suspended solids and other factors affecting water "color" were not part of CCIW's analysis scheme. Other factors studied such as organic carbon, conductivity, etc. indicate increased levels inshore of the thermal bar. This phenomenon is particularly important because it occurs in the warm near-shore waters in the spring which is when many newborn organisms are in their very susceptible early life stages. These organisms tend (because of breeding habits and availability of food) to spend the early part of their life in the near shore water where they are subjected to elevated pollution loadings resulting from the thermal bars impediment to dilution.

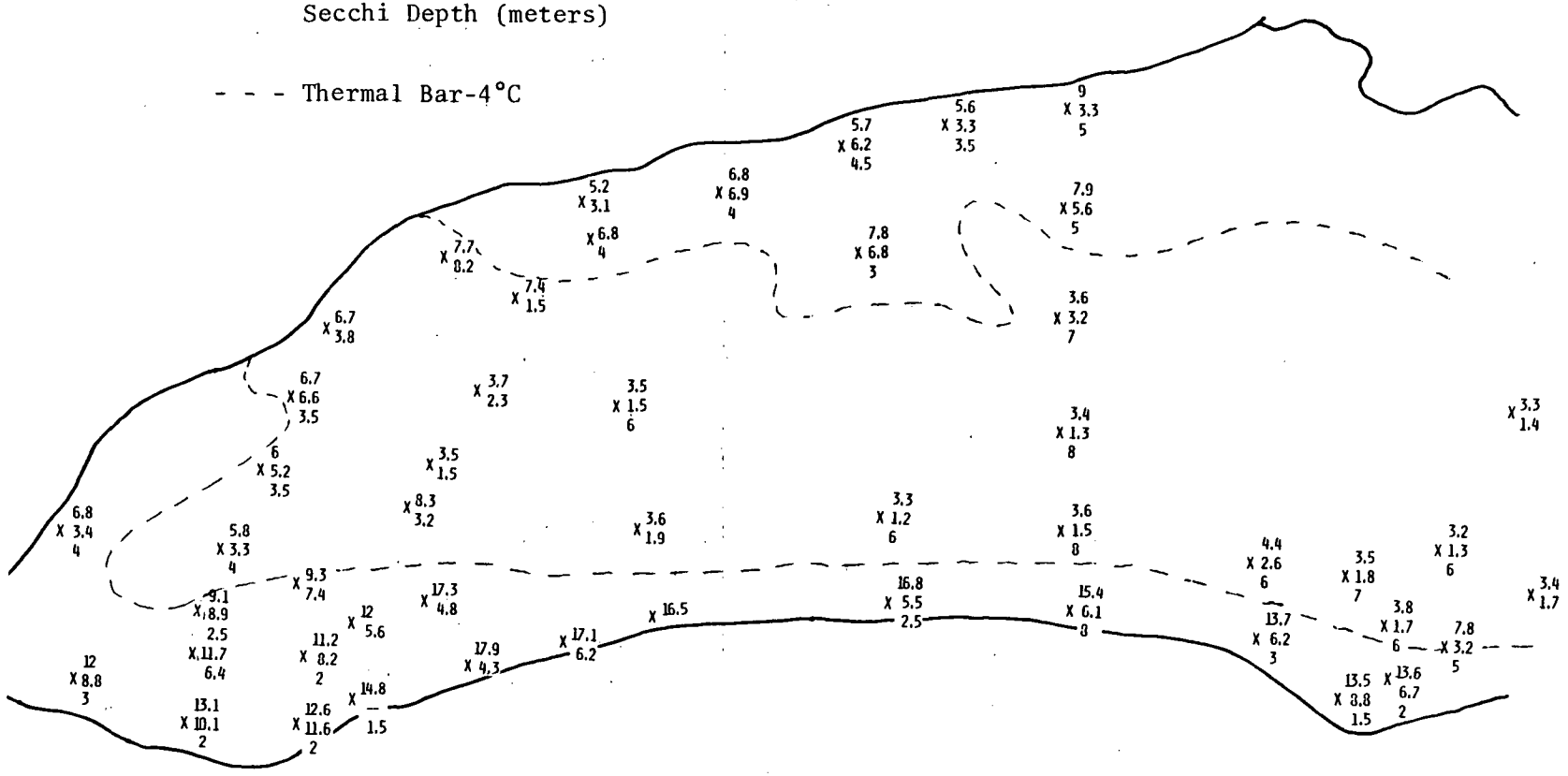

Figure 4-6. Water Quality Measurements for Lake Ontario. The Canadian Center for Inland Waters Collected In Situ Measurements of Temperature, Chlorophyll Concentrations, and Secchi Depth Across Lake Ontario From 5-9 June 1978. The Location of the Thermal Bar as Determined From the Calibrated HCMR Data of 6 June 1978 is Also Shown. This Illustration Clearly Shows the Increased Chlorophyll Concentrations and Turbidity Associated With the Warm Water Inshore of the Thermal Bar.

The HCMR sensor, combined with other spaceborne sensing platforms offers a way to monitor the current location of the thermal bar and its impact on water quality. As seen in Figure 4-7a, HCMR data can be used not only to study whole lake phenomena but also the microstructure of the thermal phenomena. In this figure, we have color coded the thermal data from 6/6/78. The warm water ringing the lake is clearly evident. It is also clear from this figure that localized effects from runoff (e.g., Niagara and Genesee Rivers) can be monitored using HCMR data. By combining the thermal detail available from HCMM with the detail on certain water quality parameters available from the reflected visible energy sensors aboard other spacecraft, a method of monitoring critical conditions could be established. For example, in Figure 4-7a we can see the thermal plume from the Niagara River at the southwest end of the lake. In general, the pollution carried in this water would be diluted by mixing throughout the lake, but the thermal bar essentially forces the river water to hug the shore mixing with other runoff water thereby potentially increasing pollution loads rather than decreasing them. (As an example, industrial discharge levels could be restricted during periods when turbidity indicators were approaching a predetermined critical indicator of excess pollution loading and dilution volumes as indicated by HCMM were expected to be inadequate to reduce concentration levels.)

In addition to monitoring the seasonal development of the thermal bar HCMM's diurnal coverage provides a unique capability for monitoring short term developmental processes. This is dramatically demonstrated in Figure 4-7b. In this figure the nighttime thermal image of a portion of Lake Ontario near Rochester has been subtracted from the daytime image for 6/6/78 and the results color encoded. The deep purple tones in the center of the lake represent regions of essentially no temperature change. The light purple regions inshore of the thermal bar represent slight increase in temperature due to runoff and increased solar absorption near the surface caused by higher turbidity in the inshore waters. The regions color encoded in blue, green and yellow represent increasingly significant changes in temperature. These colors represent the outward advance from shore of the thermal bar. The daytime heating combined with the influx of runoff has

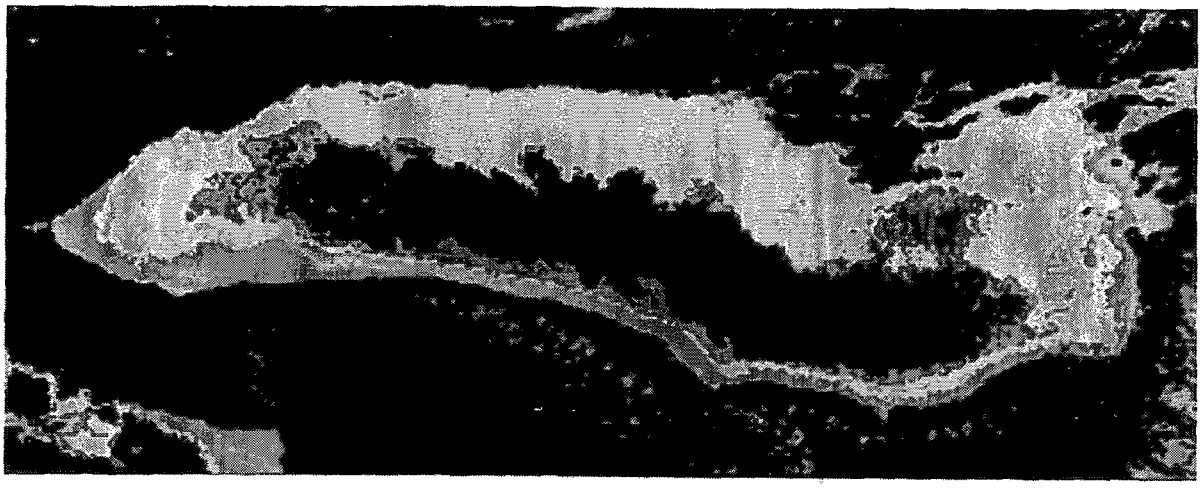

Figure 4.7a. Color Encoded Thermal Map of Lake Ontario - 6 June 1978. From Hot to Cold, the Colors Range From Orange Through the Yellows, Greens, Blues, Pinks and Violets to Dark Blue.

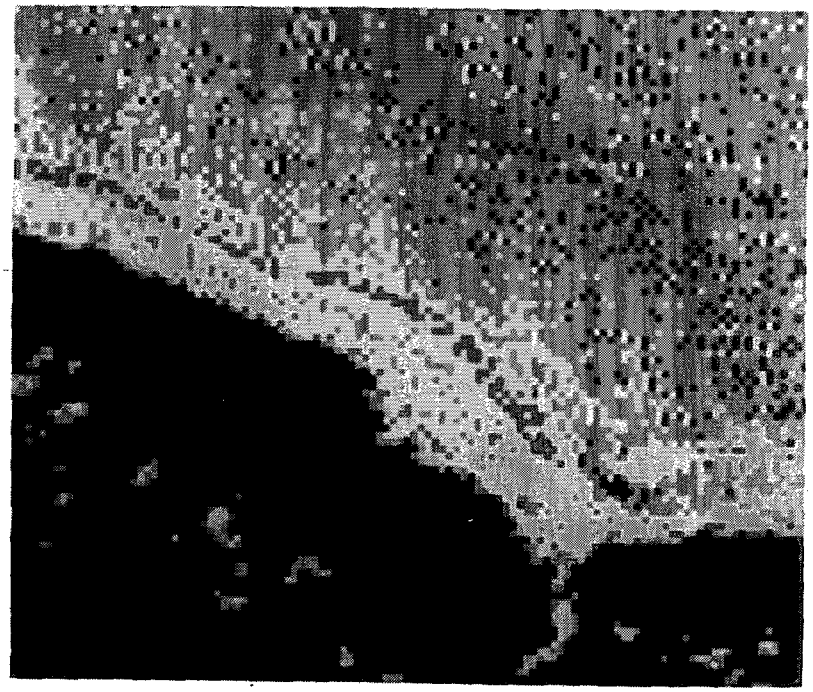

Figure 4.7b. Color Encoded Temperature Difference Image - 6 June 1978 - Illustrating the Changes in Temperature of Lake Ontario Surface Water at the Thermal Bar Over a Twelve Hour Period. The Purple Tones Seen on Both Sides of the Thermal Bar Represent Little Temperature Change. The Regions Color Encoded in Blue, Green and Yellow Represent Increasingly Significant Changes in Temperature Related to the Outward Advance From Shore of the Thermal Bar.

pushed the thermal bar outward so that the temperature difference in this region is now composed of daytime inshore water minus cold central core water from the previous night. The bar has advanced approximately 1 to 1.5 kilometers outward along most of the shore line during this 12 hour period. The bar advanced less in the eastern portion of the image and shows no advance just offshore of the Genesee River discharge. The river discharge presumably had previously introduced a bulge in the bar which would tend to mask advances until the rest of the bar advanced beyond the influence of the plume. We observe a similar phenomena at the mouth of the Niagara River. The increased turbulance and currents at these major discharges also tend to disrupt somewhat the pattern and stable progression of the thermal bar.

The observed advance rate of the bar on this day of 1 to 1.5 km /day seems reasonable since the mean advance rate of the bar from the south shore is about 32 km/45 days or 0.7 km/day. We would expect considerable daily variance in the advance rate with high insolation days (such as the days when HCMM coverage is good) showing higher rates. Analysis of HCMM Night - Day - Night data might also provide answers to questions about diurnal advance and partial withdraw of the thermal bar.

In summary, we found that HCMM data could be successfully used to study both regional and local water resource problems. Daily and seasonal development of the thermal bar as well as the effect of the thermal bar on regional water quality were observed.

4.3 HCMM's Role in Studying the Urban Heat Island

The processing, examination and analysis of HCMM thermal data performed under this effort has indicated that the HCMM imagery can be an invaluable tool for studying characteristics of the urban heat island phenomenon. It can enable efficient study of the individual factors which affect the development of the heat island by providing detailed temperature information across an entire urban area.

The most beneficial property of the HCMM thermal imagery is that it provides a rare opportunity to examine the thermal patterns associated with a real urban complex at a resolution amenable to analysis of small scale effects of individual urban features within a metropolitan area. In the past, studying the urban heat island phenomenon consisted predominantly of developing and analyzing theoretical models (Miller et al 1972, and Myrup 1969) and implementing expensive ground truth or aerial data collection programs (Lenschow and Dutton 1964). The HCMM imagery, however, now provides a relatively inexpensive opportunity to carefully examine some of the thermal properties associated with the urban heat islands as well as to analyze the existent models of this phenomenon.

The HCMM imagery lends itself to analysis of the heat island problem in numerous ways. The frequent reimaging of the same metropolitan areas permits examination of the same urban area under various meteorological conditions. This includes both changes in local weather conditions (e.g. wind speed and direction, temperature, sky conditions) and various degrees of severity in the heat island formation. Imagery over any one urban area is collected within a short period of time thus eliminating the variable of changing meteorological conditions which plague attempts to collect thermal radiation data using other approaches. The integrity of the HCMM imaging system is more than sufficient to describe major changes in temperature within the island. The image resolution permits observation of thermal effects from relatively small features within the urban center.

These properties of HCMM imagery related to its potential application to analyzing the urban heat island problem permit the careful examination of certain aspects of the heat island. In depth analyses of individual metropolitan areas using the thermal information recorded on this imagery can help provide answers to questions concerning the effects of particular urban features on the overall development and dissipation of the heat island. Furthermore, the multiple date coverage of major urban centers can efficiently provide information on the changing role of these individual features under various sky, temperature and wind conditions as well as their changing roll under various degrees of heat island severity. Determination of the influence of particular urban features on the heat island problem can in turn lead to improved city planning to benefit the health and comfort of the people who work and live there.

In summary, then, the heat island experiment conducted under this effort indicates that abundant information relative to the urban heat island phenomenon is currently available in existing HCMM imagery. Through straight forward data processing this information can be employed to further our understanding of and control over the heat island problem.

Section 5

CONCLUSIONS AND RECOMMENDATIONS

The HCMM experiment has been extremely successful in providing new insights into the urban heat island and water resource phenomena. The unique high resolution synoptic perspective of thermal properties that the HCMM experiment has provided has allowed us a look at these phenomena as never before possible.

We have been able to monitor the formation and development of the thermal bar over all of Lake Ontario. By employing the underflight calibration technology HCMR data can be mapped directly to actual surface temperatures. This allows detailed mapping of the thermal structure of the entire lake surface and precise location of the thermal bar. Near shore water quality variations observed by Landsat and documented in situ were demonstrated to be associated with the thermal bar phenomena by analysis of HCMM data. HCMM's unique temperature difference product proved valuable in studying in detail the short term-diurnal development and advance of the thermal bar. High resolution thermal infrared HCMM data, in particular when used with other remotely sensed data, can provide very valuable monitoring and, potentially, forecasting data on large water resources. In general, both HCMM's spatial and thermal resolution were adequate for large water resource studies. More repetitive coverage would greatly increase the utility of the data from future satellites.

A reliable calibration method that did not require underflight data would also be of great benefit in future missions. While inconclusive because of the limited amount of data analyzed, our studies indicate that the standard infrared atmospheric propagation models are inadequate for precise calibration of satellite data. We recommend a more detailed study of this problem to attempt to determine whether the internal calibration on-board the HCMR failed or if, as is more likely, the limitation indeed lies with the atmospheric models. If the failure was on-board HCMM then more intensive application of any available underflight data could be used to define the corrections necessary for future quantitative use of HCMR data.

In the urban heat island experiment, we have seen that the high resolution thermal imagery provided by the HCMM satellite is adequate to monitor detailed surface temperature variations across large areas. The large changes in temperature between urban and rural areas common to the heat island phenomenon can be easily monitored using the satellite imagery. Examination of the correlations between these changes in temperature and the wind, temperature, and sky conditions present during numerous satellite overflights could increase our understanding of the relative importance of individual meteorological factors in the overall development and dissipation of the heat island.

Because of the high resolution of the HCMM thermal imagery, we were also able to examine temperature variations associated with the microclimates found throughout the metropolitan areas being studied. The beneficial effects of city parks, open spaces, and heavily treed residential districts as well as the detrimental effects of over-urbanized commercial areas and industrial heat sources could be readily seen on the thermal imagery. The repeated coverage of the same metropolitan areas under various meteorological conditions provides a means for closely examining the roles of individual urban features in the urban heat island phenomenon.

Never before has so complete a picture of the urban heat island phenomenon been obtained than that which is contained within the imagery provided by the HCMM satellite. The availability of this imagery as well as similar imagery from future satellites could contribute greatly to research efforts involved in studying and understanding the heat island problem, possibly bringing about more timely implementation of improved urban planning techniques to benefit the health of urban inhabitants.

Our experiments relative to the utility of HCMM data for earth resource applications, in particular as a tool for studying and monitoring both our water resources and the urban heat island phenomenon, have indicated that the data can constitute an invaluable tool for both research and resources management. We further feel that the potential of the

HCMM data, even in these particular applications alone, goes far beyond that called out in this report. We suspect that further investigation of these data and their applications would certainly open more doors to further applications and immeasurable benefits.

APPENDIX A

Excerpted from

"TEMPERATURE MEASUREMENT OF
COOLING WATER DISCHARGED FROM POWER PLANTS"

Photogrammetric Engineering and Remote Sensing
Vol. 45, No. 6, June 1979, pp. 753-761

by

John R. Schott
Calspan Corporation
Buffalo, NY 14225

TEMPERATURE MEASUREMENT OF COOLING WATER DISCHARGED FROM POWER PLANTS*

John R. Schott

Calspan Corporation
Buffalo, New York

Introduction and Summary

The growing number and size of power facilities have stimulated the interest of scientists, legislators and the public in the effects such stations have on aquatic environments. The impact of thermal discharges on aquatic ecology and the effects on aquatic organisms that are drawn through cooling systems are of particular concern. To ensure proper protection and management of the environment as well as continued generation of required power, procedures must be developed to accurately assess environmental effects in a timely and cost-effective manner. In monitoring the cooling water discharged into a water body, the temperature value and spatial extent of the thermal plume are the parameters of interest. These thermal plumes can, in some instances, extend more than a mile from the discharge point and include temperature increases in excess of $15^{o}F$.

Airborne thermal infrared imaging systems have been used to study some of these problems.[1-3] These systems generate an image (similar to a photograph) of the heat energy radiated by water surfaces. For example,

---

*The work reported here was sponsored by the New York State Energy Research and Development Authority (NYSERDA) under an agreement dated August 23, 1976 with Calspan Corporation.

the brighter the water appears on the image, the higher the temperature of the water is. The advantage of this approach is that the thermal scanner can image the entire surface area of a discharge plume in minutes. In this manner, all the internal detail as well as the shape and spatial extent can be easily determined. The disadvantage of this approach is that a boat is required to provide data needed to convert brightness levels on the image to temperature values.

In an effort to resolve technical, operational and cost problems associated with the existing approaches, a program was initiated to develop and test wholly airborne calibration of a thermal scanner system so that precise thermal maps could be generated without requiring data from boats. This technique involved development of a model relating the signal at the sensor to the surface temperature and the atmospheric effects contributing to the signal at the sensor.

Procedures were developed for collection and analysis of the thermal imagery such that the terms in this model could be calculated. Data collection procedures included flying the aircraft at different altitudes over the same point in the water and flying parallel flight lines so that data from points in the water could be viewed at different look angles. These procedures add a minimal amount of time to data collection and provide sufficient data so that an analysis of the terms relating water temperature to the signal actually reaching the sensor can be calculated. Once these terms, including atmospheric transmission, sky radiation and reflectance of the water, have been determined, the water surface temperature can be calculated.

In an effort to evaluate this technique, a series of "blindfold" tests was made.[5] In these tests an airplane flew over a boat located at different positions in the water at different times and on different days. The aircraft values were then compared to the boat values, which had been withheld until the aerial determinations were made.[6] Results of this test indicate that on the average, the aerial measurements fell within $0.70^{\circ}F$ of the boat temperatures (standard deviation $\pm 0.59^{\circ}F$ for 63 points). On the basis of these results, this wholly airborne approach, called the "angular calibration technique," is considered operational for airborne measurement of water surface temperatures.

This paper discusses the airborne calibration technique and the experimental test program. For the sake of brevity, the details of the airborne collection system are omitted and the assumption is made that the radiant energy reaching an airborne sensor can be converted to an apparent blackbody temperature equivalent.

Theoretical Approach

Thermal scanners generally detect radiation in the 8-14 μm bandpass. This section will discuss how the radiant energy detected by a sensor at aircraft altitudes (~600 m) is not only a function of temperature but is also functionally dependent on atmospheric and background terms. In addition, the types of measurements required to calculate the values of these additional terms will be defined.

All matter at temperatures above absolute zero radiates electromagnetic energy. The relation between radiant energy, W (emittance), and temperature, T, in ^{o}K is expressed by the Stephen Boltzmann equation

$$W = \sigma T^4, \tag{1}$$

where σ is a proportionality constant.

The general equation for a blackbody radiator is given by the Planck distribution equation,

$$W_\lambda = 2\pi c^2 h^{-5} (e^{hc/kT} - 1)^{-1}, \tag{2}$$

where: W_λ is the radiant emittance per unit wavelength interval,

c is the speed of light,

h is Planck's constant,

k is Boltzmann's constant,

T is temperature, and

λ is wavelength.

This equation, derived from quantum physics, is a function of the quantum radiation states within a blackbody cavity.

The Stephen Boltzmann equation is obtained by integrating the Planck equation over all wavelengths.

The problem in using these equations is finding the dependence of W on temperature over a defined bandpass. The Stephen Boltzmann equation indicates that radiant emittance integrated over all wavelengths varies as T^4, i.e.,

$$\int_0^\infty W_\lambda \, d\lambda = W = \sigma T^4. \qquad (3)$$

To find the functional dependence on temperature in a finite bandpass, it is necessary to use a series expansion solution to the normalized integral of radiant emittance. This yields the fraction of energy less than a given wavelength, D, given by

$$D = \frac{\int_0^\lambda W\lambda \, d\lambda}{\int_0^\infty W\lambda d\lambda} \qquad (4)$$

These D values are tabulated in standard blackbody tables for ranges of T, λ or λT combinations.[4] By finding the difference in D for two wavelengths, a relation can be developed between temperature and radiant emittance in a bandpass expressed as a fraction of the total radiant emittance.

If D is the fraction of the total energy emitted by a blackbody between the wavelength 0 and λ, then D_1-D_2 is the fraction of emitted energy between λ_1 and λ_2. Since σT^4 is the total energy for a given temperature, then $W = (D_1-D_2)\,\sigma T^4$ is the radiant energy emitted for a given bandpass. Values of W and T over the range of interest can be stored in data files on a computer. T can then be calculated from the stored W values.

We can therefore express the radiant energy from a blackbody over the 8-14 μm bandpass ($W_{\Delta\lambda}$) as

$$W_{\Delta\lambda} = W_T = \int_8^{14} 2\pi\, c^2\, h^{-5}\, (e^{hc/kT} - 1)^{-1} \qquad (5)$$

This expression, however, is only true for a blackbody. A blackbody is a perfect radiator and absorber; therefore, all the incident energy is absorbed and reradiated. In practice, the bodies we will be concerned with will be gray bodies, which are not perfect absorbers or radiators in the 8-14 μm bandpass and thus have emissivities less than unity.

Emissivity (ε) is the ratio of energy radiated from a source to energy radiated from a blackbody at the same temperature. Thus, for a gray body,

$$W = \varepsilon\, W_T \qquad (6)$$

To interpret the radiant energy reaching a point at any distance from the source, one must consider atmospheric or path effects; of prime concern is atmospheric transmission over the path lengths of interest. The atmospheric transmission window between 8 and 14 μm is the most useful for earth observation work for a number of reasons. It encompasses the radiant energy peak of 9.5 μm for objects near earth ambient temperature of 300^{o}K. The transmission is quite high over the entire window, and the window is spectrally very broad, permitting integration over a sizable fraction of the total distribution.

Primary attenuation in the lower atmosphere is due to absorption by H_2O vapor, CO_2 and OH. These molecules absorb the radiation and reradiate it as a function of temperature, thereby introducing two noise terms into the system.

These terms can be included in the expression we have defined as follows:

$$W = \tau\varepsilon W_T + W_A \tag{7}$$

where τ is the atmospheric transmission and W_A is the apparent radiant emittance from the air column between the source and sensor, as well as energy scattered into the sensor. It is important to keep in mind that W_A and τ vary as a function of atmospheric conditions on a given day and also within the air column because of layering effects in the atmosphere.

In addition to the radiant energy from the source itself, a certain amount of energy will be reflected from the ground. This energy comes from both the sun and the sky. Solar reflection effects can be avoided by proper orientation of flight lines. Skylight reflection effects can be expressed as $W_s\ \tau R$ and included in equation (7), yielding

$$W = \tau\varepsilon W_T + W_A + W_s\ \tau R \tag{8}$$

where W_s is the radiant energy from the sky incident on the surface observed, and can be associated with an equivalent sky temperature T_s. R is the surface reflectance of the water.

Skylight irradiance comes from scattered solar radiation, radiation emitted from components of the atmosphere (especially the ozone layer and H_2O vapor); and energy from the earth reflected by the atmosphere. All these effects combine to give the sky an apparent radiometric temperature as viewed from the ground. For our purposes, this is the blackbody temperature equivalent T_s associated with the amount of energy incident on the source over the bandpass of interest. T_s can vary considerably with sky conditions from about 300^oK for heavy overcast to well below 250^oK for clear sky conditions.

In evaluating the range of values for the reflectance terms, we recognize that reflection is dependent on look angle. In addition, we have mentioned that W_A and τ are dependent on the length and composition of the atmospheric path between the source and observation point. To recognize this dependence in equation (8), the functional dependence on θ and h will be added to designate angular and height dependence, respectively

where h is the height of sensor above terrain,

θ is look angle measured from the vertical and

$$W(h, \theta) = \tau(h,\theta)\ \varepsilon(\theta)\ W_T + W_A(h,\theta) + \tau(h,\theta)\ W_s\ R(\theta) \quad (9)$$

Limiting our discussion for the moment to vertical viewing, ($\theta = 0$) results in

$$W(h) = \tau(h)\varepsilon\ W_T + \tau(h)\ W_s\ R + W_A(h) \quad (10)$$

Letting $W(0)$ be the energy from the ground as it would be measured vertically at zero altitude, equation (10) reduces to

$$W(h) = \tau(h)\ W(0) + W_A(h) \quad (11)$$

where $$W(0) = \varepsilon W_T + W_s R \quad (12)$$

If $W(h)$ and $W(0)$ are known for a set of observed values, then by least squares analysis of (11), $\tau(h)$ and $W_A(h)$ can be calculated. $W(h)$ and $W(0)$ represent the radiant energy observed by the sensor at flight altitude and ground level, respectively. In practice, the ground level measure is obtained by extrapolating a plot of altitude-versus-temperature to zero altitude using data collected over the same point at a series of altitudes, where radiant energy is converted to apparent blackbody temperature.

If we once again consider the angular viewing effects, equation (11) becomes

$$W(h,\theta) = \tau(h,\theta)\ W(0,\theta) + W_A(h,\theta) \tag{13}$$

where $W(0,\theta) = \varepsilon(\theta)\, W_T + W_S\, R(\theta)$ and (14)

$$\tau(h,\theta) = \tau(h,0)\ \exp\ (1/\cos\ \theta) \quad \text{and} \tag{15}$$

$$W_A\ (h,\theta) = W_A(h,\ 0)/\cos\ \theta. \tag{16}$$

These equations result from the increase in absorption with path length (15) and the increase in atmospheric radiation with path length (16). Since the path length increases as $1/\cos\ \theta$ for slant viewing and the effects on atmospheric emissions should be very nearly linear for small increases in path length through a given medium, equation (16) is derived. Note that this assumption of linearity is only valid for increase due to slant viewing through a known atmosphere and is not necessarily valid for an overall increase in path length.

If observations were made at the same altitude of a given point through two different look angles, one of which may be taken as vertical for convenience, then equations (10), (13) and (14) may be combined to yield

$$W(h, 0) = m\,W(h, \theta) - m\tau(h, \theta)\,W_s\,\bar{R}(\theta) - mW_A(h,\theta) + \tau(h, 0)\,W_s R(0) + W_A(h, 0)] \quad (17)$$

where $$m = \frac{\varepsilon(0)\,\tau(h, 0)}{\varepsilon(\theta)\tau(h,\theta)} \quad (18)$$

Recognizing this as a straight line in the form,

$$W(h, 0) = mW(h, \theta) + I \quad (19)$$

and solving for W_s in terms of m and I yields

$$W_s = \frac{I + mW_A(h,\theta) - W_A(h, 0)}{\tau(h,0)\,R(0) - m\tau(h,\theta)\,R(\theta)} \quad (20)$$

Least squares analysis of equation (19), with input data consisting of apparent temperatures (converted to radiant energy) measured along a line viewed vertically and then at a slant angle, will yield from equation (20) a measure of apparent sky temperature as viewed from the ground.

We have assumed that the apparent temperature of the sky is a constant with respect to angle of observation. In general, this is not the case; rather, the zenith sky appears colder than the sky near the horizon because the atmosphere viewed vertically has fewer radiators. Because of the variability of sky conditions, a functional relationship

between sky temperature and view angle is not readily defined nor are the errors introduced by the assumption of a constant sky easily evaluated. In order to minimize potential errors in measured sky temperature, the analysis discussed above can be conducted for a number of look angle combinations, and a simple relationship between T_s and θ can be developed.

Another solution would involve use of a vertical- viewing, upward-looking radiometer on board the aircraft. Measurement of vertical sky temperature at a number of altitudes and extrapolation to the apparent temperature of the nadir sky as viewed from the ground would eliminate one unknown in equation (17). The equation could then be solved for the sky temperature at look angle θ (i.e., T_s associated with $R(0)$ would be known and T_s associated with $R(\theta)$ would be unknown).

Rewriting equation (9) as

$$W_T = \left[W(h,\theta) - \tau(h,\theta)\, W_S\, R(\theta) - W_A(h,\theta)\right]/\varepsilon(\theta)\, \tau(h,\theta) \qquad (21)$$

we find

$W(h,\theta)$	is a measured value;
$W_A(h,\theta)$	is obtained from equation (16) and least squares analysis of (11);
$\tau(h,\theta)$	is obtained from equation (15) and least squares analysis of (11);
W_s	is obtained from equation (20);
$R(\theta)$ and $\varepsilon(\theta)$	are tabulated values for water.

It should therefore be possible to measure the absolute value of surface waters based on the theories developed thus far. The next section contains procedural approaches for collection of necessary input data to solve for the values in equation (21).

Experimental Design

Our concern at this point is in defining procedures for collecting sufficient input data to permit the use of the theoretical procedures under discussion. Again, we will neglect, for simplicity, signal processing through the sensor and assume that apparent blackbody radiometric temperature can be measured at the sensor location by converting radiant energy to equivalent blackbody temperature.

As shown in equation (11), the input data necessary to calculate the transmission term $\tau(h)$ and the additive target-independent energy from the atmosphere $W_A(h)$ consists of $T_B(h)$ and $T_B(0)$ corresponding to $W(h)$ and $W(0)$. $T_B(h)$ is simply the apparent blackbody temperature measured at altitude h with look angle $\theta = 0$. $T_B(0)$ is the apparent temperature measured at the surface of the water. This value cannot be measured directly but is obtained by a profile technique which involves a simple extrapolation process for data collected at a series of altitudes to a zero altitude case obtained by consecutive flights over the same target.[7] A target consists of an area of uniform temperature either large enough to be directly below the aircraft during the profile or within about 10° from the nadir and distinct enough to be identifiable on the profile images. At angles much larger than 10° the assumption of vertical viewing during the profile no longer holds.

The minimum data input required for equation (11) is $T_B(h)$ and a corresponding $T_B(0)$ for at least two points at differing temperature. Ideally this data consists of a set of approximately five data points covering as wide a temperature range as possible. Figure 1 indicates how $T_B(h)$ and $T_B(0)$ could be obtained for a number of different temperatures.

The input data necessary to calculate W_s, the sky light radiance term, comes from the solution of equation (19) requiring $T_B(h, 0)$ and $T_B(h,\theta)$ as inputs. These values are the apparent temperature observed at the same point through two look angles where one look angle is chosen as zero degrees for convenience. (Note also that equation (11) can be solved directly for W_s, i.e., a one point solution is available). The minimum

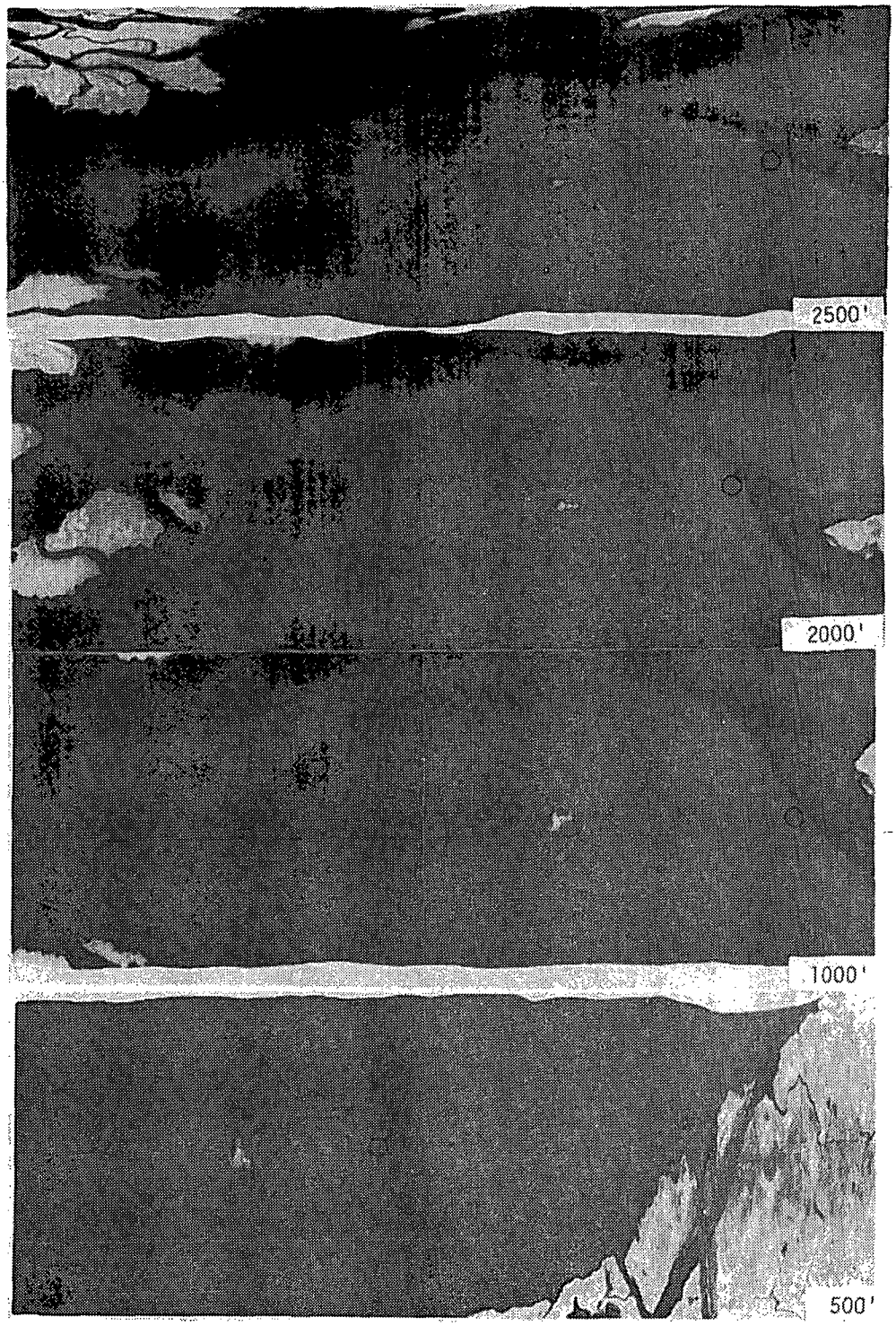

FIGURE 1. THERMAL IMAGES OBTAINED DURING A PROFILE. AREAS OF EQUAL TEMPERATURE ARE INDICATED WHERE RADIOMETER READINGS COULD BE MADE.

data required to solve equation (19) consists of two data sets composed of $T_B(h,0)$ and $T_B(h,\theta)$ for two distinct points. In general, a number of points with a large range in temperature should be used to solve for m and I in equation (19). This data can be collected by flying two parallel flight lines and allowing for some sidelap. This procedure is often used to obtain complete target coverage and would add little or no time to most collection efforts. Figure 2 illustrates how this data could be obtained.

A ground-truth program was used to evaluate these radiometric calibration techniques. This effort involved aerial overflights of a boat anchored at a series of positions in the Hudson River, both within and beyond the thermal plumes of various power plants.

With the boat anchored at a given position, readings were made on the upstream (downstream if flow was upstream in the estuary) side of the boat. Measurements consisted of temperatures recorded from a submerged thermistor (nominally at a depth of 6 in.) and from a Barnes PRT 5 radiometer. During each fly-over, approximately ten readings were recorded and averaged to predict the temperature at a point. To insure unbiased data, all surface measurements were made by independent consultants and surface data were withheld until aerial results had been delivered to NYSERDA. The surface radiometer was calibrated in the field under prevailing atmospheric conditions to ensure that all measurements were absolute surface temperature measurements.

The main survey took place on September 24, 1976 with the boat anchoring at eight positions throughout the day. The aircraft flew over each position four times, permitting 32 data-comparison points for the total survey.

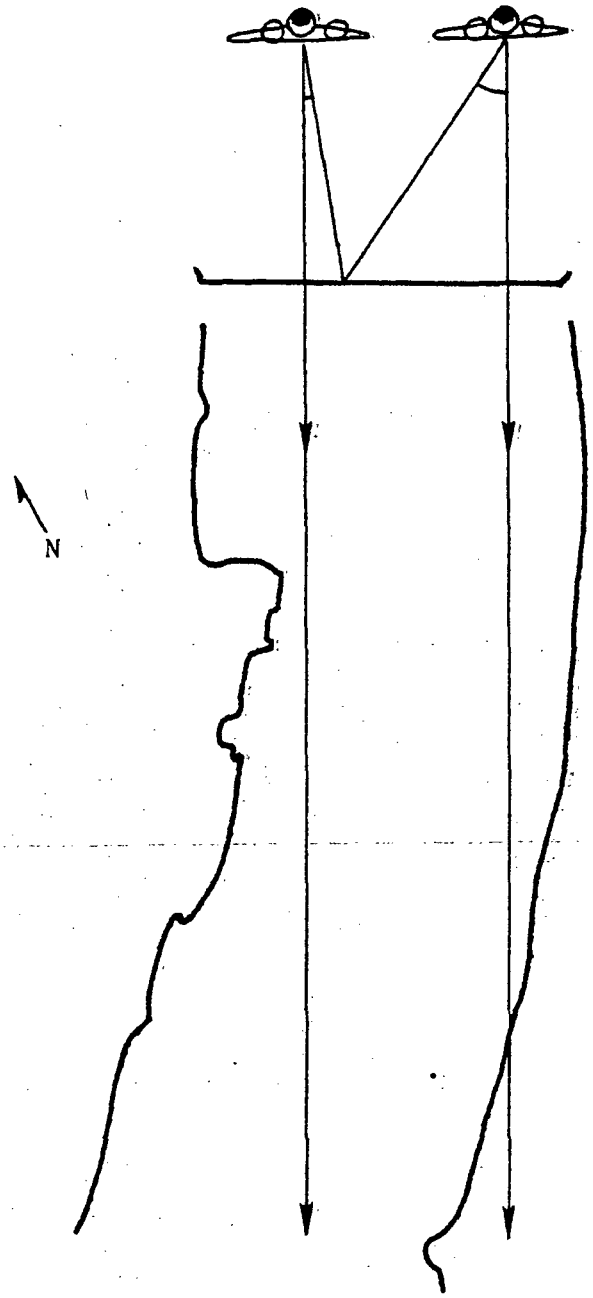

FIGURE 2

EXAMPLE OF PARALLEL FLIGHT LINES OVER A POWER STATION SHOWING THE CHANGE IN LOOK ANGLE FOR A GIVEN GROUND POINT.

Because the boat was covered with aluminum foil, it had a low emissivity and could be located as a "cold" spot on the image. Surface temperatures were predicted using the calibration technique discussed above. Data were also collected at eight positions for five overflights on both July 8 and 9 1976. However, the July 8 data could not be used because of calibration problems with the surface instrument.

Results

Table 1 presents the results of the data correlation for September 24. The mean and standard deviations of the absolute value of the difference between the aerial and surface data are presented. Radiometric surface data was used because it is a more accurate measure of the actual surface temperatures than is the submerged thermistor. Comparison of submerged (6 in.) thermistor data and aerial data showed a mean difference of $0.51^{o}F$ with a standard deviation of $0.46^{o}F$. Also included is a correlation of radiometric temperatures, to which no atmospheric correlations have been applied, with the surface data. Table 2 contains the results of the July 9 survey.

When the July and September data are combined, a mean error of $0.70^{o}F$ is obtained with a standard deviation of $0.59^{o}F$ (Angular Technique). This compares with a mean error of $3.23^{o}F$ with a standard deviation of $1.25^{o}F$ if only internal system calibration is used. Figure 3 illustrates the precision of the calibration technique and the limitations of using only internal scanner calibration. The figure shows the surface radiometer data

Table 1

Comparison of Surface and Aerial Data

for 24 September 1976 (^{o}F)

	Surface Radiometer and Uncorrected Airborne Scanner	Surface Radiometer and Angular Technique
Mean of the absolute value of the temperature difference between boat and aircraft	4.19	.55
Standard deviation of ΔT	1.22	.57

Table 2

Comparison of Surface and Aerial Data

for July 9, 1976 (^{o}F)

	Surface Radiometer and Uncorrected Airborne Scanner	Surface Radiometer and Angular Technique
Mean of the absolute value of the temperature difference between boat and aircraft	2.66	.80
Standard deviation of ΔT	1.27	.57

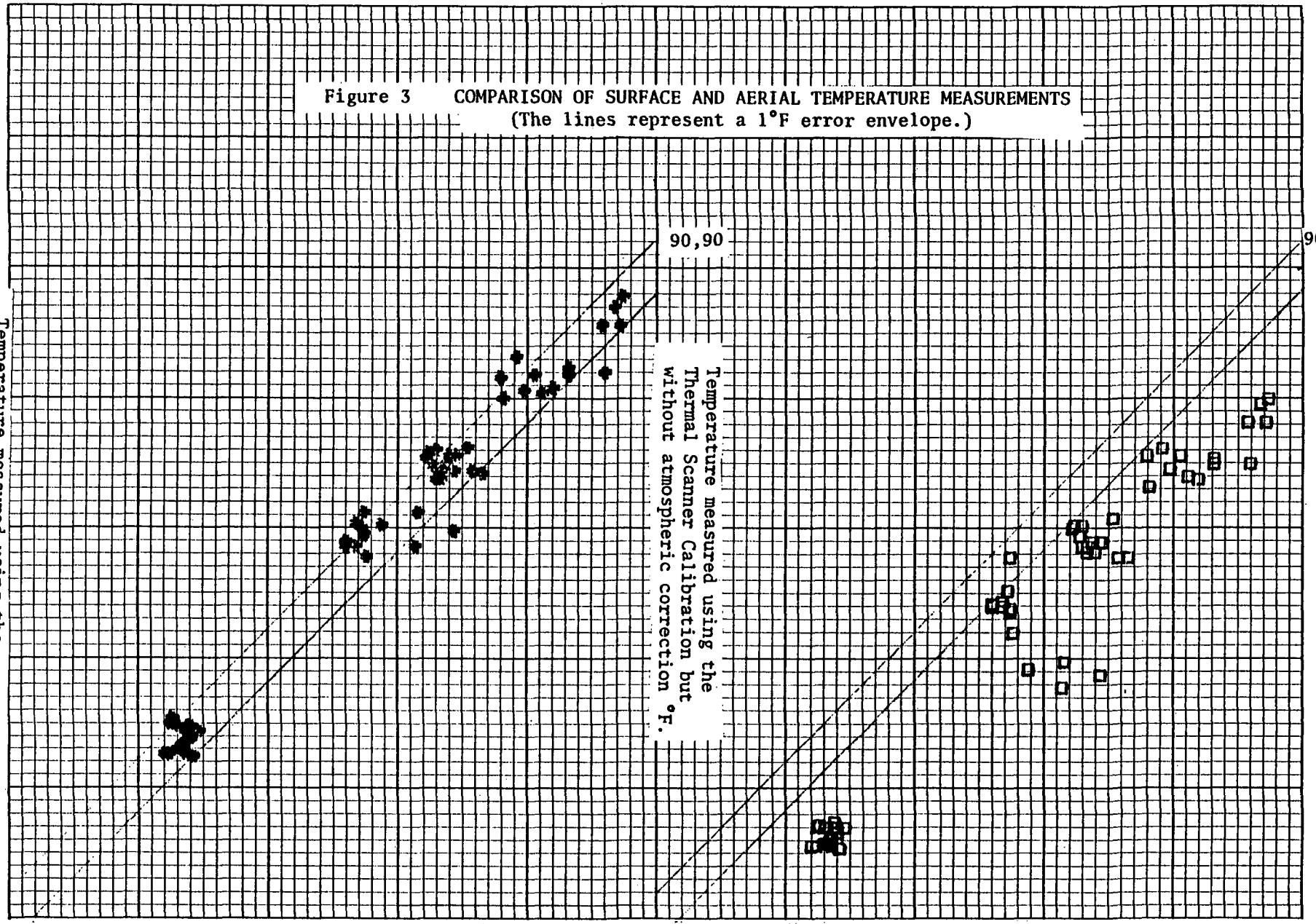

Figure 3 COMPARISON OF SURFACE AND AERIAL TEMPERATURE MEASUREMENTS
(The lines represent a 1°F error envelope.)

plotted against the calibrated (#) and uncalibrated (0) scanner data. The data, which has been corrected for atmospheric and background effects, shows a very close fit within the $1^{o}F$ error bars. The data using only the internal scanner calibration shows sizable errors and is generally less than the actual temperature. Note that this is generally the case but that a temperature higher than the true surface temperature can be detected by airborne systems under certain atmospheric and background conditions.

One shortcoming to the angular technique is a requirement for extra data to permit calibration and some additional data processing. Neither the time nor the cost is appreciable; however, the data must be properly collected. Some improvements in accuracy could be expected if data collection were modified to facilitate analysis using the angular technique. Major improvements cannot be expected because temperatures predicted from the air approach the accuracies obtainable by surface measurements.

Conclusions and Recommendations

The data correlation results presented in the previous section indicate that a major advance in airborne radiometric measurement of water surface temperatures has been achieved. Measurement accuracies essentially as good as surface measurements are demonstrated.

The data collection procedures involve only minor variations in standard collection practices requiring approximately fifteen additional minutes of flight time. Data processing can all be done on a desk-top computer.

The net result of these conclusions is that a fully airborne approach to measure water surface temperatures, with accuracies comparable to those obtained from surface measurements, is an operational reality. In addition, these results were obtained through use of an outside consultant for acquisition of ground-truth data, thus precluding any bias.

We recommend that future efforts in this area be directed at techniques to generate thermal maps with appropriate corrections at angles away from vertical. The corrections developed using the angular calibration techniques are quite accurate and should be applied in map generation. Current mapping techniques do not apply a correction for variations in apparent temperature at non-vertical look angles; development of these corrective procedures in the map-generation process would allow the full accuracies developed in the angular calibration technique to be carried through a final map product. In addition, data collected specifically for analysis using this technique should eliminate the need for iterative solutions and should further improve calibration accuracies. While major improvements in water temperature measurements could not be expected because the current results already so closely approach surface measurements, improvements applicable to such problems as a quantitative measurement of heat loss from buildings could be expected. In fact a major advantage of this technique is that it includes consideration of sufficient variables to allow surface temperature measurement of any uniform flat surface whose emissitivity is known.

REFERENCES
(Appendix A)

1. Bartolucci-Castedo, L.A., et al, "Computer Aided Processing of Remotely Sensed Data for Temperature Mapping of Surface Water from Aircraft Altitudes," LARS Publication, Purdue University, Indiana, 1973.

2. Haynes, R.B. and Whipple, J., "Problems in Applying Infrared Reconnaissance Technology to Water Temperature Surveillance," Technical Memorandum No. RADC/IR/TM-71-2, 1971.

3. Scapace, F.L., Madding, R.P., and Green III, T., "Scanning Thermal Plumes," Ninth International Symposium on Remote Sensing of Environment, April 1974.

4. Pivovonsky, M., and Nagel, M.R., "Tables of Black Body Radiation Functions," The MacMillan Company, New York 1961.

5. Schott, J. R., "Thermal Remote Sensing Calibration Techniques," Calspan Report NA-6019-M-1, NTIS #TB-269-471, 1977.

6. "Report of Infrared Water Temperature Measurements Made September 24, 1976 of the Hudson River," Wormser Scientific Co. Report, Stamford, Connecticut.

7. Schott, J. R. and R. H. Tourin, "A Completely Airborne Calibration of Aerial Infrared Water Temperature Measurements," Proceedings ERIM Tenth International Symposium on Remote Sensing of Environment.

APPENDIX B

Excerpted from

"THE BLUE-TO-GREEN REFLECTANCE
RATIO AND LAKE WATER QUALITY"

Photogrammetric Engineering and Remote Sensing
Vol. 44, No. 10, October 1978, pp. 1303-1310

by

Kenneth R. Piech
John R. Schott
Calspan Corporation
Buffalo, NY 14225
Kenton M. Stewart
State University of New York
Buffalo, NY 14260

INTRODUCTION

One alternative to the enormous effort required for extensive sampling of water resources is the use of satellite and aircraft imagery. Such imagery can not substitute completely for in-situ measurements of physical, chemical, and biological variables; however, the data can provide substantial assistance in a synoptic evaluation of the water quality of lakes.

The objective of this study was to evaluate satellite and aircraft measurements of lake reflectances, particularly the relative values of blue and green reflectances, as indices of water quality. Recent papers and extensive reviews (Graham, 1966; Fruh et al., 1966; Stewart and Rochlich, 1967; Piech and Walker, 1971; Likens, 1972; Bukata et al., 1974; Strong, 1974; Thomson et al., 1974; Wrigley and Horne, 1974; and Boland, 1976) have indicated that optical properties of lakes and related chlorophyll values are important in water quality and trophic assessments. Our investigation, involving remote sensing and field work, extends the relationship between trophic parameters and optical properties by comparing selected water quality indices and reflectance ratios for lakes of varying trophic character. The investigation has also developed a promising methodology for differentiating changes in chlorophyll, lignin, and humic acid concentrations.

The two lakes given the most attention during this study were Lake Ontario, the easternmost Great Lake, and Conesus Lake, the westernmost Finger Lake in New York State. Aircraft imagery were obtained for Lake Ontario in 1972 and 1973, and for Conesus Lake in 1973. Satellite imagery was also collected over Lake Ontario in 1973. In-situ measurements of physical, chemical, and biological variables were obtained on both lakes. The Lake Ontario data were gathered in 1972 during the International Field Year on the Great Lakes (IFYGL), while the in-situ data

for Conesus Lake were obtained in 1973.

The primary technique for data analysis involved densitometry of color imagery and subsequent analyses to remove atmospheric and film processing effects from the photographic data. Accurate measurements of the ratios of broad band reflectances could then be obtained. The reflectance data were compared with in-situ measurements of Secchi disk, irradiance, and chlorophyll in an attempt to derive relationships between changes in the optical and changes in the trophic variables.

METHODS

A. Lake Data

The Secchi disk measurements were made with all white disks (30 cm dia) on Lake Ontario and black and white disks (20 cm dia) on Conesus Lake. Irradiance measurements at depth in Lake Ontario were made with a Hydro Products Relative Irradiance meter equipped with a green filter (Wratten #58).

Water samples for chlorophyll(a) were collected at numerous stations in Lake Ontario by personnel of the Canada Centre for Inland Waters aboard vessels Porte Dauphine, Limnos, and Martin Karlsen. Chlorophyll values were determined by the spectrophotometric method of Strickland and Parsons (1968). Sample values from one and five meters were averaged and then a lake-wide average was determined.

Water samples for chlorophyll(a) from Conesus Lake were collected by boat from selected sites with an "integrated" open tube sampler (according to Lund, 1949), and analyzed by the spectrophotometric method of Lorenzen (1967). Chlorophyll(a) values from both lakes were corrected for pheo-pigments.

B. Aerial Data

The aerial data base consisted of color imagery from aircraft (Piper Aztec and B-26) and satellite (Skylab) overflights. The aircraft imagery utilized Ektachrome MS2448 color film from Hasselblad 500EL cameras with 80 mm focal length lenses. The Skylab imagery utilized S0242 film from the Skylab S190 camera package.

The three color film layers (red-, green-, and blue-sensitive) provided information on the color of the lakes in each photograph. A densitometer measurement of each film layer could thus provide a measurement of the brightness of the lake in the three color bands. Atmospheric and film processing effects, however, modify the color of the lake. Therefore, before the color information could be related to trophic indices, the atmospheric and film processing effects had to be removed from the density information in each film band.

A method to measure these effects and relate exposure values to reflectance values has been described previously (Piech and Schott, 1974; Piech and Walker, 1974; Piech et al., 1975). The method uses densitometry of shadows within the image to establish the additive exposure caused by the atmosphere and the transmission loss through the atmosphere. Shadows cast by buildings near the shorelines of the lakes were used to calibrate the color imagery and thus relate film exposure to lake reflectance. Detailed analyses of the accuracy of the shadow calibration process have shown that reflectance ratios can be measured to an accuracy of $\pm$10% of the ratio value (Piech et al., 1975). Such an accuracy appears sufficient to measure changes in chlorophyll concentration.

C. Laboratory Data

The lake sampling and aerial data were supplemented by a laboratory investigation of reflectance changes caused by varying amounts of chlorophyll, lignin, and humic acid.

The major difficulties associated with such a laboratory experiment are reproducing the geometry and illumination conditions of a large lake satisfactorily. The geometry of the problem is that of an infinite half space (An infinite half space approximates a large deep lake, i.e., a medium with x and y extent from $-\infty$ to $+\infty$, and z extent from 0 to $-\infty$). Constructing an approximation to the half space while retaining the ability to vary the parameters of the medium is difficult. Similarly, it is difficult to create satifactory illumination over the half space approximation.

The above difficulties were resolved by the apparatus of Fig. 1. A square tube, 0.07 meters on the side and 0.5 meters long, was lined with aluminum foil so that specular reflections from the foil would approximate a slab with infinite extent in directions perpendicular to the long axis of the tube. The tube was immersed in a vat of water, approximately 0.5 m^3 in volume, whose composition could be readily changed. A collimated tungsten source illuminated the tube at one end. The light reflected back from the tube was, in turn, collected by a fibre optics probe with a cosine collector head. The other end of the fibre optics bundle was integrated into the photomultiplier tube and electronics of the microdensitometer of the photointerpretation console described by Piech et al. (1975). Measurements were made in red, green, and blue spectral bands using Wrattan 90 series filters.

The reflectance and transmission of the medium in the slab, r and t, were measured by monitoring the reflected signal from a set of known

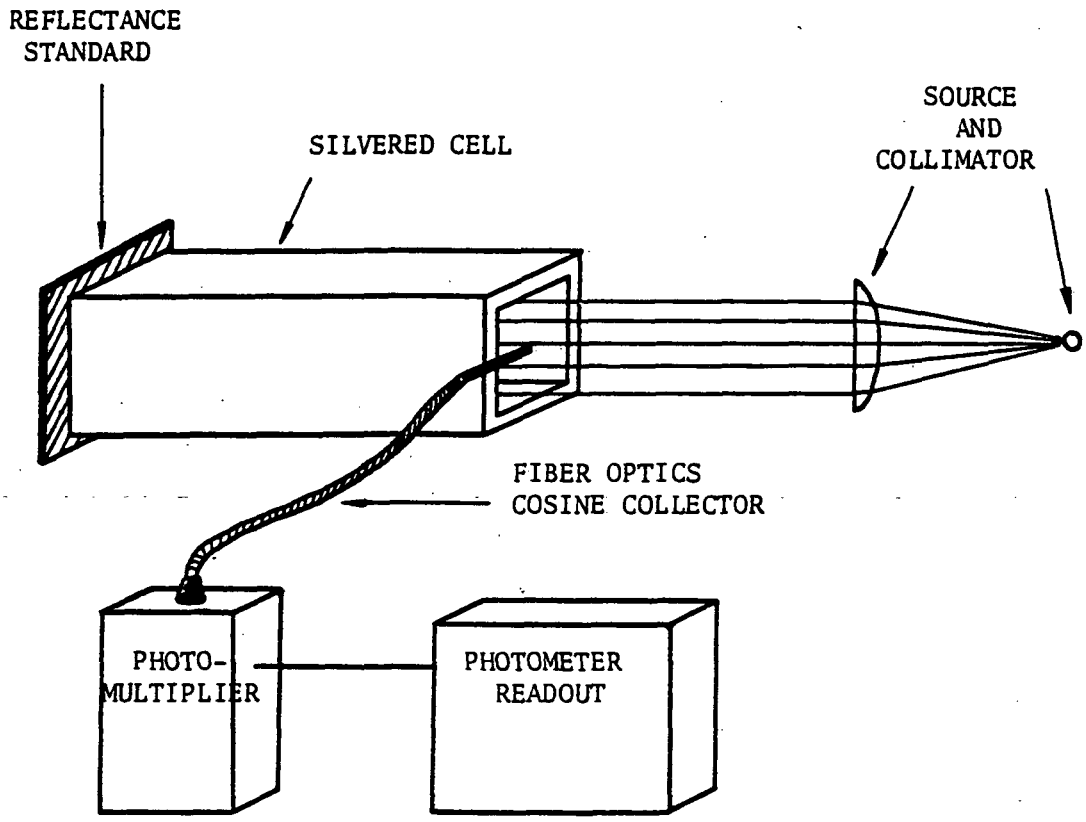

FIGURE 1

Schematic of Laboratory Apparatus for Reflectance Measurement.

reflectance standards at the end of the slab. The reflectance of these standards ranged from 2 to 30 percent. The reflected signal, S, to first order consists of the signal reflected by the medium alone, s(r), and that signal transmitted through the medium and reflected by the end reflector, i.e.,

$$S = at^2R + s(r) + c = mR + b$$

where R is the reflectance of the end reflector, and a and c are instrument constants. The correlation coefficient, r^2, for the linear fit between S and R was always in excess of 0.99 for all the test media. A set of six reflectance standards was used to establish the fit to Eq. (1).

The apparatus was calibrated using distilled water as a standard. Letting the subscript o denote distilled water,

$$S_o = at_o^2R + s(r_o) + c = m_oR + b_o$$

The values adopted for distilled water transmission in the red, green, and blue spectral bands were 75.0, 93.3, and 98.1% per meter, respectively, or t_o = 86.6%, 96.6%, and 99.0%.

Comparison of the slopes of the test and standard media then yields t through

$$t = t_o\sqrt{\frac{m}{m_o}} \quad . \tag{3}$$

The difference between the intercepts of the test and standard media curves yields r through

$$b-b_o = s(r) - s(r_o) \approx s(r), \text{ and} \tag{4}$$

$$r = \frac{s(r)t_o^2}{m_o} \quad . \tag{5}$$

The reflectance for infinite depth was obtained from the diffuse reflectance, r, and transmission, t, of the tube or slab by consecutive computation of the reflectance, r_2, and transmission, t_2, of slabs with double thickness. The necessary equations are

$$r_2 = r + \frac{t^2 r_2}{1-r^2} \quad , \tag{6}$$

$$t_2 = \frac{t^2}{1-r^2} \quad . \tag{7}$$

The doubling was continued until no change in the reflectance was obtained.

The properties of the medium were varied by additions of chlorophyll, lignin, and humic acid. The chlorophyll was added in the form of water-soluble chlorophyll; the lignin was in the form of bleached hardwood paper pulp. Since the chlorophyll was on a soap substrate, the weight of water-soluble chlorophyll necessary to simulate a given concentration of in-vivo chlorophyll was determined by matching spectral responses on the standard spectrometer method for measuring chlorophyll concentration. The chlorophyll concentrations were varied from 0 to 7 µg/l while lignin concentration ranged from 0 to 70 mg/l and humic acid from 0.5 to 1.8 mg/l.

A major difficulty with the experiment proved to be the soap substrate of the water-soluble chlorphyll. The original intent was to modify the chlorophyll concentration while keeping the scattering turbidity constant so that a model could be developed for chlorophyll concentration at varying degrees of background turbidity. Unfortunately, the soap substrate modified the background turbidity by contributing a spectrally uniform scattering as chlorophyll concentration was changed. The net effect of this background turbidity was to dampen changes in the reflectance ratios.

Reflectance change with addition of both chlorophyll and lignin was linear. As the amount of chlorophyll was increased, the increased scattering by the substrate effectively cancelled the increasing absorption of the chlorophyll in the blue. The blue reflectance thus remained a uniform 4% from 0 to 7 μg/l. The green reflectance varied from 2.7 to 7.2% over this concentration range, while the red reflectance changed from 1.1 to 2.9%. The corresponding variation in the blue to green reflectance ratio was from 1.5 to 0.6, with the variation being approximately linear. Reflectance of the medium with lignin variation was 4% to 11% in the blue, 2.7% to 8.5% in green, and 1.1% to 5.7% in red.

The data obtained by individual variation of the three components were supplemented by joint variation of the components. As a result, it was possible to develop a set of discriminators for determining whether a turbidity change is caused by a variation in lignin, chlorophyll, or humic acid.

RESULTS

A. Ratios

The study of Lake Ontario during 1972 established the feasibility of monitoring selected water quality indices using aircraft imagery at scales as small as 1:50,000. The study demonstrated that indices such as depth of photic zone (1% relative irradiance in green spectral region), Secchi disk transparency, total attenuation coefficient, and chlorophyll concentration could be related to the ratio of blue lake reflectance to green lake reflectance as measured from the color film imagery. Figure 2 illustrates these relationships using lake-wide averages, i.e., averages over all lake stations occupied. Although station by station comparisons are more complex,

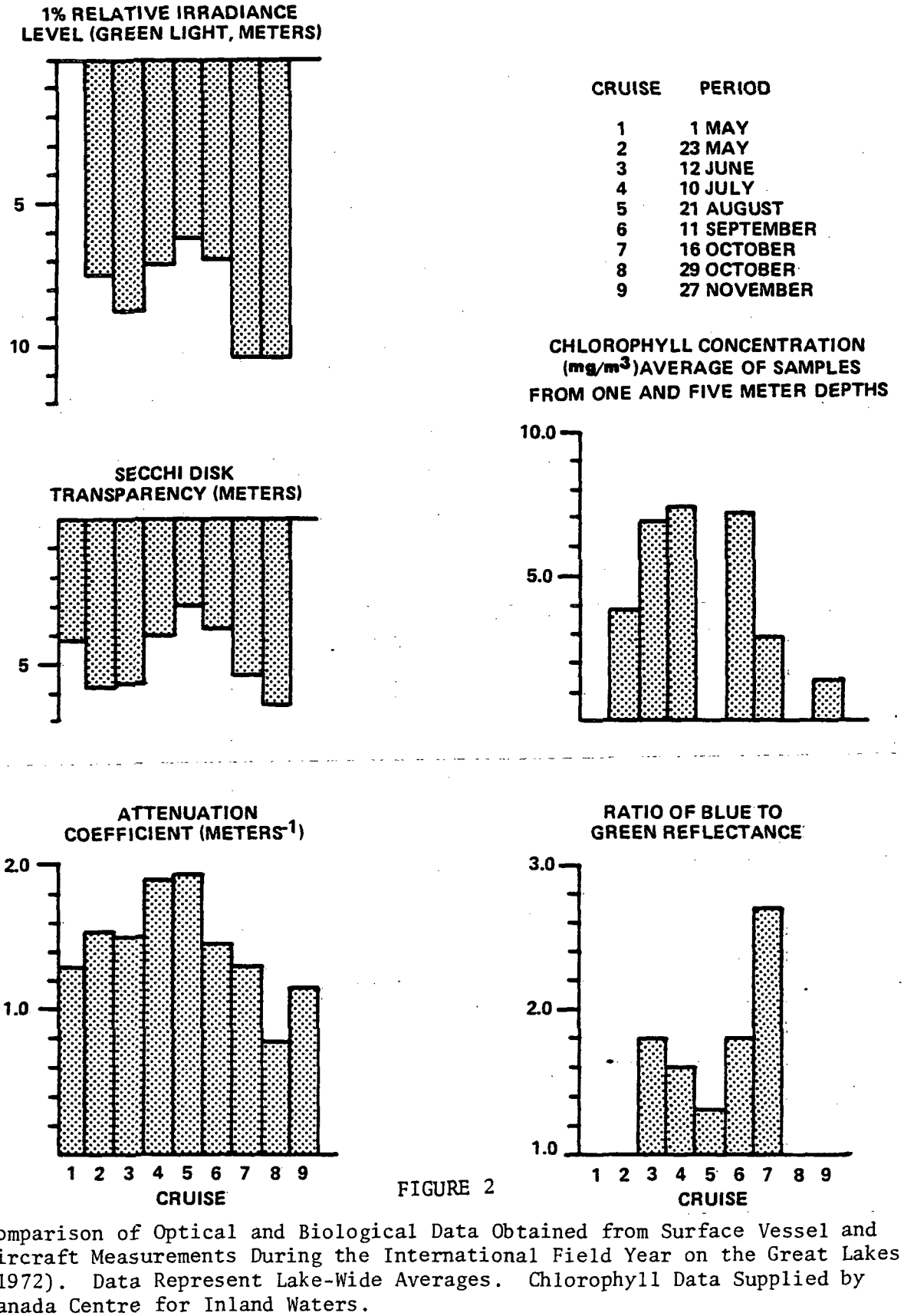

FIGURE 2

Comparison of Optical and Biological Data Obtained from Surface Vessel and Aircraft Measurements During the International Field Year on the Great Lakes (1972). Data Represent Lake-Wide Averages. Chlorophyll Data Supplied by Canada Centre for Inland Waters.

the data of Fig. 2 generally indicate a surprising seasonal relationship between the various parameters. The ratio of blue to green reflectance is inversely proportional to chlorophyll concentration and coefficient of total attenuation and directly proportional to photic zone depth and Secchi disk transparency.

A key aid in water quality evaluation of lakes from optical data would be the use of satellite imagery. A test was therefore conducted to determine if lake reflectances could be measured to sufficient accuracy for such assessments from Skylab imagery.

Figure 3 is a Skylab S190A image (from an altitude of ~435 km) of Lake Ontario in which the Skylab satellite track and two aircraft tracks are indicated. The simultaneous aircraft underflights were at an altitude of 3 km on two north-south tracks separated by approximately 50 km.

The S190A image of Lake Ontario was processed to remove atmospheric effects to yield a color encoded display of the blue to green reflectance ratio and the data from this display were compared to the aircraft data at a scale of 1:40,000. About 15 photographs were obtained on each aircraft track, with each photograph covering an area of about 6.6 km^2.

The resolution of the Skylab imagery was only 15 to 30 meters, insufficient for the shadow calibration mentioned earlier. The Skylab imagery was calibrated using reflectances of objects measured on previous flights, e.g., coal piles and aircraft runways (Piech, et al., 1975). The aircraft imagery was calibrated using shadow analyses at the ends of the aircraft tracks.

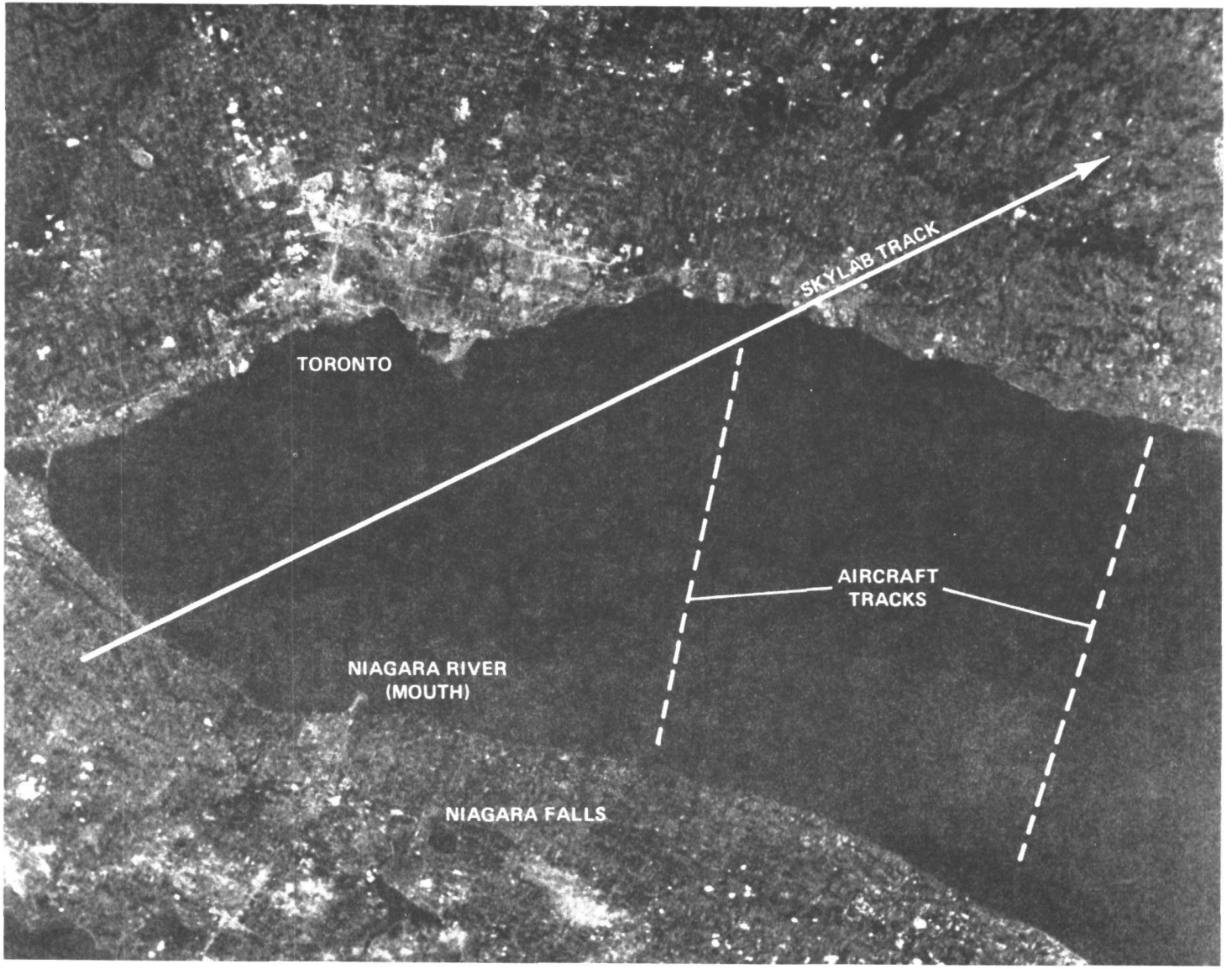

Figure 3. Black and White Copy of a Skylab S190A Color Image of the Western Half of Lake Ontario, 9 Sept. 1973. Two Frames of Imagery Covered the Lake on this Skylab pass. The Large Urban Complex on the North Shore is Toronto. The Discharge on the South Shore Just West of the Niagara River is the Welland Canal. The Niagara Falls and the White Water of the Lower Niagara River can be Observed Just to the South of the Two Power Station Reservoirs Which Straddle the Niagara River. The Altitude From Which This Image was Taken was Approximately 435 km. Resolution on the Original Transparency is Superior to This Copy.

Figure 4 compares the satellite and aircraft data obtained on the two tracks. The aircraft points include error bars corresponding to $\pm$ 12% of the blue to green reflectance ratio and $\pm$ 1.6 km in aircraft position. The statistical correlation between reflectance ratios of the satellite and aircraft is excellent (correlation coefficient = 0.87 in Olcott to Gold Point flight and 0.98 in the Troutberg to Chub Point flight, highly significant in both cases). This indicates that either S190 imagery or aircraft imagery may be utilized for defining the optical properties of the lake using relationships similar to those obtained on the IFYGL program.

The relationship between the optical and trophic parameters is dependent on the physical properties of the lake being studied. For example, Fig. 5 contains the relationship between blue to green reflectance ratio and chlorophyll concentration for Conesus Lake, as obtained on the Skylab effort. Again, a strong dependency is evidenced with a marked blue-green minimum occurring at maximum chlorophyll concentration, although the specific relationship of chlorophyll concentration and ratio level differs from the Ontario values. The variation occurs because Conesus and Ontario are quite different in physical character. For example, Conesus is darker than Ontario, having a green reflectance of about 2% compared to a reflectance of 3% for Lake Ontario. The darker the lake, the greater the effect chlorophyll absorption can be expected to have on the blue-green ratio. The actual situation is, of course, more complicated than this simple model.

A major area of further research therefore involves generalizing the relationships between aerial and surface data. By way of example, Conesus and Canadice Lakes (the latter of which is a shorter but deeper Finger Lake near Conesus Lake) had approximately the same range of chlorophyll and Secchi disk values at the time these measurements were made. The

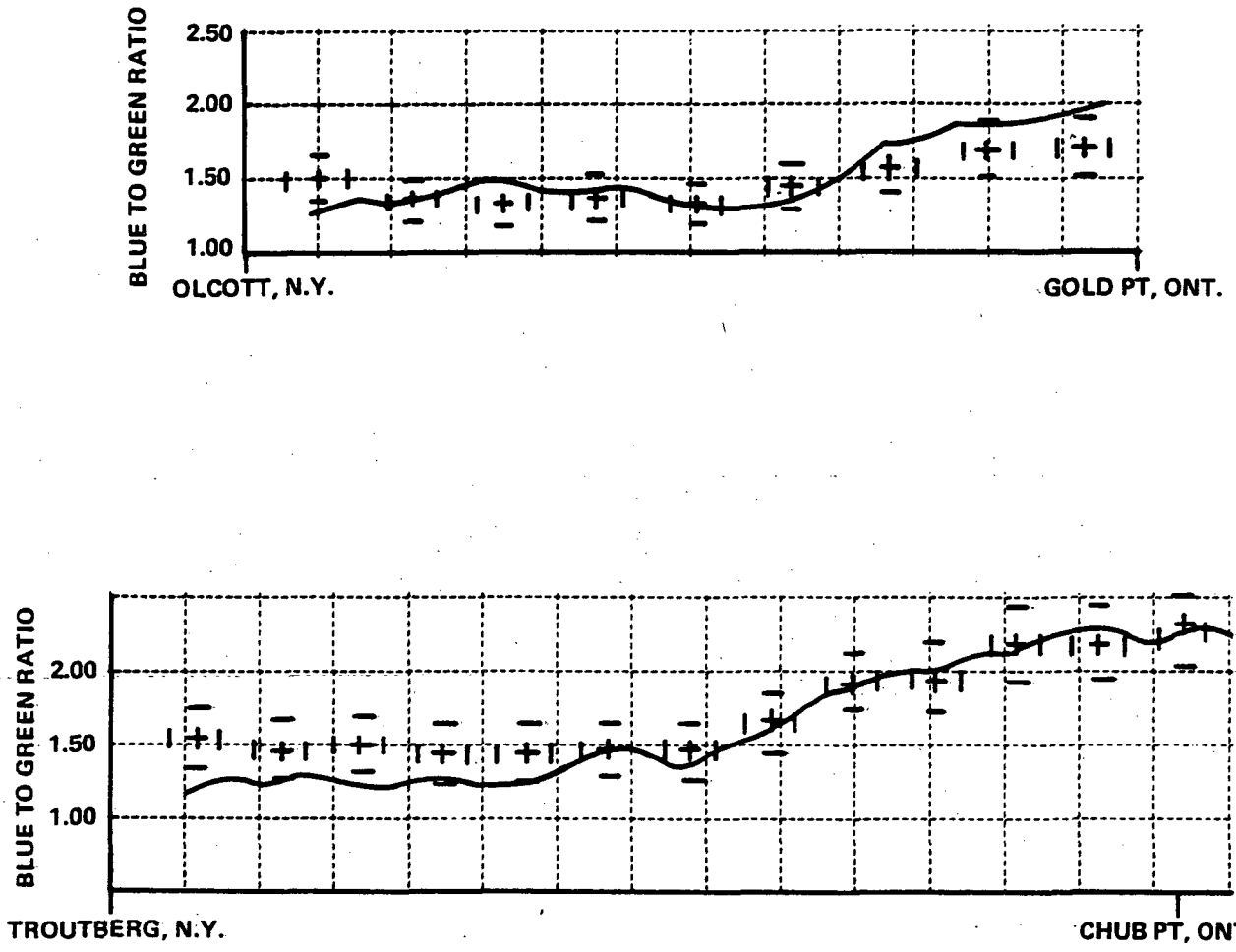

Figure 4

Comparison of S190 Measurements of Blue to Green Reflectance Ratio Along the Aircraft Tracks (Solid Line) With the Aircraft Measurements (Crosses and Error Bars). Each Division on the Horizontal Axis Represents 4.8 km. Correlation Coefficient Between Blue to Green Ratio Measurements by S190A Satellite and Small Aircraft is 0.87 for the Upper Plot and 0.98 for the Lower Plot - Statistically Highly Significant in Both Cases.

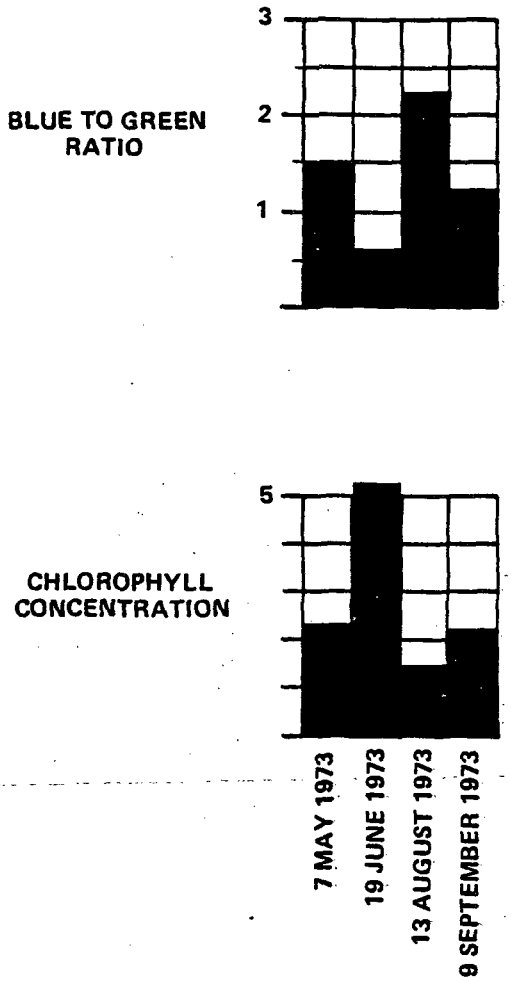

FIGURE 5

Comparison of Blue to Green Reflectance Ratio With Surface Chlorophyll Concentration in mg/l for Conesus Lake in New York.

Canadice blue to green ratio values which correspond to the Conesus values of Fig. 6 are: 7 May, 1.5; 19 June, 0.3; 13 August, no data; and 9 September, 1.4. The close correspondence between the blue-green ratios of Conesus and Canadice, even though specific chlorophyll data for Canadice are not available on these dates, is encouraging. This correspondence, coupled with the correlation of the aerial and surface data for both Conesus Lake and Lake Ontario, leads us to believe that general relationships valid for lakes of a given trophic classification can be developed, and that such understanding will serve to significantly broaden the scope of application of sophisticated satellite photography.

B. Lignin and Humic Acid

The laboratory measurements of reflectance versus chlorophyll, lignin, and humic acid concentration attempted to broaden this understanding. The laboratory data also provided a method for relating color or turbidity changes to changes in concentrations of chlorophyll, lignin or humic acid.

The discriminators for the dominant turbidity change are listed in Table 1. In essence, the data indicate that changes in any of the three components can be discriminated by the blue to green reflectance ratio and reflectances of the green and red bands. The blue to green ratio is inversely proportional to chlorophyll concentration, does not vary with humic acid, and is directly proportional to the amount of lignin. The green and red reflectances are directly proportional to both chlorophyll and lignin, while the green reflectance is inversely proportional to humic acid and red reflectance is unchanged by humic acid. Measurements of the blue to green reflectance ratio and green and red band reflectances thus appear sufficient to specify variations in chlorophyll, lignin, and humic acid concentration. Use of Table 1 in studying the Skylab image of Fig. 3 indicates that major

Table 1

DISCRIMINATORS FOR CHANGES IN
CHLOROPHYLL, LIGNIN AND HUMIC ACID*

Variable	Change	Discrimination Equation
chlorophyll	increase	if $\frac{B}{G} < \frac{B1}{G1}$ and $G \geq G1$ and $\frac{B}{R} < \frac{B1}{R1}$
chlorophyll	decrease	if $\frac{B}{G} > \frac{B1}{G1}$ and $G < G1$ and $\frac{B}{R} > \frac{B1}{R1}$
lignin	increase	if $R \geq R1$ and $G \geq G1$ and $\frac{B}{G} \geq \frac{B1}{G1}$ and $\frac{G}{R} < \frac{G1}{R1}$
lignin	decrease	if $R \leq R1$ and $G \leq G1$ and $\frac{B}{G} \leq \frac{B1}{G1}$ and $\frac{G}{R} > \frac{G1}{R1}$
humic acid	increase	if $\frac{B}{R} < \frac{B1}{R1}$ and $G < G1$ and $\frac{B}{G} < \frac{B1}{G1}$
humic acid	decrease	if $\frac{B}{R} > \frac{B1}{R1}$ and $G > G1$ and $\frac{B}{G} > \frac{B1}{G1}$

*R1, G1, and B1 are the red, green and blue reflectances respectively at some arbitrary reference level and R, G, and B are the reflectances at the sample points.

turbidity changes may be caused by changes in chlorophyll concentration. However, it is also apparent from investigations of Dobson et al., (1974) and Bukata et al., (1974) that some variations in turbidity may also be related to particulate matter and suspended sediment.

Application of the discrimination rules of Table 1 would facilitate investigations such as studies of the effects of power plant discharges on neighboring water quality, evaluation of the impact of chlorination of power plant discharges on algal concentration, and a study of the effects of sewage treatment outfalls on stream or river conditions.

These discrimination rules have been applied to aerial imagery of power plant discharges into the Hudson River (Schott and Gaucher, 1977). Comparison of the aerial predictions based on Table 1 were verified by surface data collected simultaneously with the aerial overflights. The validity of the general behavior between chlorophyll concentration and the blue to green reflectance ratio observed on Lake Ontario and Conesus Lake for the very turbid waters of the Hudson River is quite encouraging.

SIGNIFICANCE

Our results indicate that relative chlorophyll concentrations can be monitored using blue to green reflectance ratios. Because the chlorophyll/reflectance relationship may vary between lakes of different trophic character and even within a lake, a general relationship between chlorophyll and reflectance data cannot have uniform application to all lakes. The in-situ sampling requirements are, however, significantly reduced by aerial monitoring while at the same time a more complete description of lake behavior is obtained.

ACKNOWLEDGEMENTS

We acknowledge the enthusiastic cooperation and assistance of L. B. York of the Principal Investigators Management Office at the Johnson Space Center. Major support was provided by National Science Foundation Grants GA-37768 and GA-32207, and by National Aeronautics and Space Administration Contract No. NAS9-13336. The Canada Centre of Inland Waters supplied the chlorophyll data for Lake Ontario.

REFERENCES
(APPENDIX B)

Boland, D. H. P. 1976. Trophic classification of lakes using Landsat-1 (ERTS-1) multispectral scanner data. Tech. Report EPA-600/3-76-037. 245 p.

Bukata, R. P., G. P. Harris, and J. E. Bruton. 1974. The detection of suspended solids and chlorophyll(a) utilizing digital multispectral ERTS-1 data. Proc. 2nd Canad. Sympos. Remote Sensing. 551-564.

Dobson, H. F. H., M. Gilbertson, and P. G. Sly. 1974. A summary and comparison of nutrients and related water quality in Lakes Erie, Ontario, Huron, and Superior. J. Fish. Res. Bd. Can. 31: 731-738.

Fruh, E. G., K. M. Stewart, G. F. Lee, and G. A. Rohlich. 1966. Measurements of eutrophication trends. J. Wat. Pollut. Control Fed. 38: 1237-1258.

Graham, J. 1966. Secchi disk observations and extinction coefficients in the central and eastern North Pacific Ocean. Limnol. Oceanogr. 11: 184-190.

Likens, G. E. (ed). 1972. Nutrients and eutrophication: The limiting nutrient controversy. Special Symposia Vol. I, Limnol. Oceanogr. 328 p.

Lorenzen, C. J. 1967. Determination of chlorophyll and pheo-pigments: Spectrophotometric equations. Limnol. Oceanogr. 12: 343-346.

Lund, J. W. G. 1949. Studies on Asterionella. I. The origin and nature of cells producing seasonal maxima. J. Ecol. 37: 389-419.

Pearcy, W. G., and D. F. Keene. 1974. Remote sensing of water color and sea surface temperature off the Oregon coast. Limnol. Oceanogr. 19: 573-583.

Piech, K. R., and J. R. Schott. 1974. Atmospheric corrections for satellite water quality studies. Proc. of the SPIE, 51:84-89.

Piech, K. R., and J. E. Walker. 1971. Aerial color analyses of water quality. J. Surv. Mapp. Div. Am. Soc. civ. Engrs 97(SU2): 185-197.

Piech, K. R., and J. E. Walker. 1974. Interpretation of soils. Photog. Eng., 40:87-94.

Piech, K. R., J. R. Schott, and K. M. Stewart. 1975. S190 Interpretation techniques development and application to New York State water resources. NTIS E76010081. 44 p.

Schott, J. R., and D. W. Gaucher. 1977. Aquatic and terrestrial surveys in the vicinity of power plants using remote sensing. Calspan Corporation Report NA-6019-M-2. 57 pp, NTIS PB-273463.

Schott, J. R., K. R. Piech, and J. E. Walker. 1977. Toward aquatic surveys of effects of cooling water discharges using remote sensing. Proceedings ANS Topical Symposium (Las Vegas).

Stewart, K. M., and G. A. Rohlich. 1967. Eutrophication - A review. Calif. St. Wat. Qual. Control Bd. Publ. No. 34. 188 p.

Strickland, J. D. H., and T. R. Parsons. 1968. A Practical Handbook of Seawater Analysis. Fish. Res. Bd. Can. Bull. 167. 309 p.

Strong, A. E. 1974. Remote sensing of algal blooms by aircraft and satellite in Lake Erie and Utah Lake. Remote Sens. Environ. 3:99-107.

Thomson, K. P. B., J. Jerome, and W. R. McNeil. 1974. Optical properties of the Great Lakes (IFYGL). Proc. 17th Conf. Great Lakes Res. 811-822.

Wrigley, R. C., and A. J. Horne. 1974. Remote sensing and lake eutrophication. Nature 250:213-214.

REFERENCES

1. _____ "Heat Capacity Mapping Mission Users Guide", NASA, Goddard Space Flight Center, (Second Revision) 1980.

2. Braham, R.R. Jr., "Overview of Urban Climate" Proceeding of Conf. on Metropolitan Physical Environment, USDA Forest Service TR NE-25, 1977.

3. Clarke, John F., "Some Effects of the Urban Structure on Heat Mortality," Environmental Research, Vol. 5, 1972.

4. Elliott, G.H., and Elliott, J.A. 1970. Laboratory Studies on the Thermal Bar. Proc. 13th Conf. Great Lakes Res. 413-418.

5. Elliott, G.H., and Elliott, J.A. 1971. A Mathematical Study of the Thermal Bar. Proc. 14th Conf. Great Lakes Res. 545-554.

6. Huang, J.C.K. 1972. The Thermal Bar. Geophys. Fluid Dynamics. 3: 1-25.

7. Hubbard, Davis W., and Spain, J.D. 1973. The Structure of the Early Spring Thermal Bar in Lake Superior. Proc. 16th Conf. Great Lakes Res. 735-742.

8. Martin, Frank P. and Powell, Grace L., "The Urban Heat Island in Akron, Ohio," Proceedings of the Conference on Metropolitan Physical Environment, USDA Forest Service Technical Report NE-25, 1977.

9. Menon, A.S., Dutka, B.J., and Jurkovic, A.A. 1971. Preliminary Bacteriological Investigation of the Lake Ontario Thermal Bar. Proc. 14th Conf. Great Lakes Res. 59-68.

10. Mitchell, J. Murray, "The Temperature of Cities," Weatherwise December 1961.

11. Piech, K.R., Schott, J.R. and Stewart K.M., "The Blue to Green Reflectance Ratio and Lake Water Quality" Photogrammetric Engineering and Remote Sensing, Vol. 44, No. 10, Oct. 1978, pp. 1303-1310.

12. Rangaswamy, S., Subbarayudu, J. (1978) "Radtra Computer Program" Developed under Contract NAS5-24272.

13. Rodgers, G.K., "The Thermal Bar in the Laurentian Great Lakes" Proceedings of the 8th Conf. Great Lakes Research pp. 358-363, 1965.

REFERENCES (cont.)

14. Rodgers, G.K.,1966. Publications Great Lakes Res. Div. Univ. Mich., 15: 372.

15. Rodgers, G.K., 1968. Heat Advection Within Lake Ontario in Spring and Surface Water Transparency Associated with the Thermal Bar. Proc. 11th Conf. Great Lakes Res. 480-486.

16. Rodgers, G.K. and Sato, G.K., 1970. Factors Affecting the Progress of the Thermal Bar of Spring in Lake Ontario. Proc. 13th Conf. Great Lakes Res. 942-950.

17. Rodgers, G.K. 1971. Field Investigation of the Thermal Bar in Lake Ontario: Precision Temperature Measurements. Proc. 14th Conf. Great Lakes Res. 618-624.

18. Sato, G.K. 1969. The Time of Disappearance of the Thermal Bar in Lake Ontario. Master's Thesis, Dept. of Civil Engineering, Univ. Toronto, Toronto.

19. Scarpace, F.L., Madding, R.P., and Green III, T., "Scanning Thermal Plumes," Ninth International Symposium on Remote Sensing of Environment, April 1974.

20. Schott, J.R., "Temperature Measurement of Cooling Water Discharged from Power Plants" Photogrammetric Engineering and Remote Sensing Vol. 45, No. 6, June 1979, pp. 753-761.

21. Schott, J.R., "Remote Sensing of Thermal Loadings on Aquatic Systems" Proceedings 14th Congress of the Intl. Society of Photogrammetry, Hamburg, Germany, July 1980.

22. Selby, J.E.A., Kneizys, F.X., Chetwynd, J.H., Jr., and McClatchey, R.A. (1978), Atmospheric Transmittance/Radiance: Computer Code LOWTRAN 4, AFGL-TR-78-0053.

23. Stoermer, E.F. 1968. Nearshore Phytoplankton Populations in the Grand Haven, Michigan Vicinity During Thermal Bar Conditions. Proc. 11th Conf. Great Lakes Res. 137-150.

24. Terjung, Werner H. "Urban Energy Balance Climatology: A Preliminary Investigation of the City-Man System in Downtown Los Angeles," Geographical Review, January 1970.

25. Wetzel, R.G. 1975. Limnology. W.B. Saunders Book Company, Philadephia, 743 pp.